A MODAL FINITE ELEMENT METHOD FOR THE NAVIER-STOKES EQUATIONS

by

ZLATKO SAVOR
B.Sc. (Eng.), University of Zagreb, 1969

A THESIS SUBMITTED IN PARTIAL FULFILLMENT OF
THE REQUIREMENTS FOR THE DEGREE OF
MASTER OF SCIENCE

in

THE FACULTY OF GRADUATE STUDIES
Department of Civil Engineering

We accept this thesis as conforming
to the required standard

THE UNIVERSITY OF BRITISH COLUMBIA
September 1977

In presenting this thesis in partial fulfilment of the requirements for an advanced degree at the University of British Columbia, I agree that the Library shall make it freely available for reference and study. I further agree that permission for extensive copying of this thesis for scholarly purposes may be granted by the Head of my Department or by his representatives. It is understood that copying or publication of this thesis for financial gain shall not be allowed without my written permission.

Department of Civil Engineering

The University of British Columbia
2075 Wesbrook Place
Vancouver, Canada
V6T 1W5

Date September 30, 1977

ABSTRACT

A modal finite element method is presented for the steady state and transient analyses of the plane flow of incompressible Newtonian fluid. The governing restricted functional is discretized with a high precision triangular stream function finite element. Eigenvalue analysis is carried out on the resulting discretized problem, under the assumption that the nonlinear convective term is equal to zero. After truncating at various levels of approximation to obtain a reduced number of modes, the transformation to the new vector space, spanned by these modes is performed. Advantage is taken of the symmetric and the antisymmetric properties of the modes in order to simplify the calculations. The Lagrange multipliers technique is employed to incorporate the nonhomogeneous boundary conditions. The steady state analysis is carried out by utilizing the Newton-Raphson iterative procedure. The algorithm for transient analysis is based upon backward finite differences in time. Numerical results are presented for the fully developed plane Poiseuille flow, the flow in a square cavity, and the flow over a circular cylinder problems. These results for the steady state are compared with the results obtained by direct finite element approach on the same grids and the results obtained by finite differences technique. It is concluded that the number of modes, which are to be retained in the analysis in order to achieve reasonable results, increases with the refinement of the finite element grid. Furthermore, the choice of modes to be used depends on the problem. Finally it is established, that this new modal method

yields good results in the range of moderate Reynolds numbers with about 50% or less of the modes of the problem. This, in turn, means that the time integrations can be performed on a greatly reduced number of equations and hence potential savings in computer time are significant.

TABLE OF CONTENTS

CHAPTER

LIST OF TABLES

LIST OF FIGURES

NOTATION

The specific use and meaning of symbols are defined in the text where they are introduced. Indicial notation based upon the summation convention is adopted throughout the text. Alternatively, the more common matrix notation is also used when it results in equations written more concisely, and for final expressions. Vector quantities are indicated by a lower bar, matrices by two lower bars, and triply subscripted arrays by three lower bars. When the arrays have to be written out in full, vectors are denoted by { } brackets, matrices by [ ] brackets, and transposed vectors by < > brackets. A comma followed by an index, appearing as a subscript, designates a partial derivative with respect to a spatial derivative in the direction of that index.

The Greek symbol ε implies 'belongs to' unless specified otherwise.

ACKNOWLEDGEMENTS

The author wishes to express his gratitude to his adviser, Dr. M.D. Olson, for his invaluable advice and guidance during the research and preparation of this thesis. He also expresses thanks to Dr. S.Y. Tuann for his valuable suggestions during the research work.

The financial support of the Research Council of SRH, Yugoslavia, and the Department of Civil Engineering at UBC is gratefully acknowledged.

Finally, many thanks to my wife Iva for all her help and encouragement.

CHAPTER 1

Introduction

The numerical analysis of the plane flow of incompressible Newtonian fluid constitutes an important area in computational mechanics and engineering practice. Traditionally, the most popular and thoroughly studied methods for treating problems of this type have been the various techniques based on finite difference discretization. The great progress in application of finite element procedures has been made only in the last few years. [1].

The purpose of this thesis is to establish whether it is feasible to reduce the number of discrete variables appearing in finite element approach by performing the transformation to modal coordinates. This is especially important in applications to transient problems where the cost of integrating the discrete equations in time soon becomes prohibitively expensive.

Stream function alone approach is used for finite element modelling. The restricted functional governing the problem is discretized with a high precision finite element of C^1 class. Eigenvalue analysis is carried out on the resulting discretized problem under the assumption that the nonlinear convective term is equal to zero. After truncating at various levels of approximation to obtain a reduced number of modes, transformation to the new basis defined by these modes is performed. It is shown that it is computationally more efficient to employ transformation in conjunction with Lagrange multipliers technique than transformation by condensation, even though the system size is expanded and the system matrix is nonpositive-definite. Steady state analysis is carried out by utilizing the Newton-Raphson iterative procedure. Algorithms for transient analysis are based upon backward finite differences in time and differ only in how the nonlinear

term is treated. The pressure distribution is obtained by solving the Poisson equation after all modal stream function variables in the finite element coordinates have been found.

Numerical results are presented and discussed for the fully developed Poiseuille flow, the flow in the square cavity and the flow over a circular cylinder problems. The results for the steady state are compared with the results obtained by direct finite element approach on the same grids and the results obtained by finite difference procedures.

CHAPTER 2

Basic Theory

In this chapter the partial differential equation governing the problems of plane flow of incompressible Newtonian fluid and the restricted variational principle derived from it are presented to recapitulate the theoretical basis on which modal approach shall later be built.

2.1 Partial Differential Equation

The descriptive set governing the plane flow of incompressible Newtonian fluid consists of: (a) the spatial equation of motion, derived from the dynamics of flow considerations using the principle of conservation of linear momentum, and called Navier-Stokes equation:

$$\frac{\partial u_i}{\partial t} + u_j u_{i,j} = -p_{,i} + \frac{1}{R_e}(u_{i,j} + u_{j,i})_{,j} \qquad \underline{x}\in\Omega,\ t>0 \qquad (1)$$

(b) the continuity equation derived from the kinematics of fluid flow via the conservation of mass:

$$\nabla \cdot \underline{u} = u_{i,i} = 0 \qquad \underline{x}\in\Omega,\ t>0. \qquad (2)$$

The appropriate boundary and initial conditions also have to be prescribed. The equations are written in an Eulerian frame of reference fixed in space. The normalizing system used in above equations is based on the convective time scale L/U, where L is a characteristic length and U is a characteristic velocity of the problem. Pressure is normalized with respect to the reference pressure ρU^2. Re is the dimensionless Reynolds number defined as $Re = \frac{UL}{\nu}$. The other parameters of the problem are the density of the fluid ρ, which is assumed constant and independent of temperature, the

absolute viscosity of the fluid μ, and the kinematic viscosity defined as $\nu = \frac{\mu}{\rho}$. $u_i (i = 1,2)$ are the components of velocity in x and y directions respectively, and Ω is the domain under consideration with the boundary Γ.

Viscous stresses for an isotropic Newtonian fluid are defined as:

$$\tau_{ij} = \mu(u_{i,j} + u_{j,i}) \tag{3}$$

By introducing the stream function concept the continuity equation becomes exactly satisfied and the pressure is completely eliminated, leaving the stream function as the only dependent variable. The stream function is defined as:

$$\psi_y = u \qquad \psi_x = -v. \tag{4}$$

Then by cross-differentiating Eq. (1) for each of the two directions x and y to eliminate the pressure and by expressing the velocities in terms of the stream function via Eq. (4), the following single-variable fourth order partial differential equation is obtained:

$$\frac{\partial(\nabla^2\psi)}{\partial t} = -\frac{\partial}{\partial x}\left(\frac{\partial\psi}{\partial y}\nabla^2\psi\right) + \frac{\partial}{\partial y}\left(\frac{\partial\psi}{\partial y}\nabla^2\psi\right) + \frac{1}{Re}\nabla^4\psi. \tag{5}$$

As

2.2 Restricted Variational Principle

As proven by Finlayson [2], no exact variational principle exists for this equation due to the non-selfadjoint convective terms. Therefore Olson [3] resorted to restricted variational principle. Yamada et al. [4] point out that the paper [3] was "itself a breakthrough in the application of the finite element method to field of fluid dynamics". The derivation of the principle is repeated here, extended for the time dependent term, as this principle yields the

functional, which in its discretized form serves as the basis for the modal approach.

If Eq. (5) is multiplied by $\delta\psi$ and integrated over the domain Ω the following varied integral is obtained:

$$\delta I_2 = \iint_{\Omega} [\frac{1}{Re} \nabla^4\psi + \psi_x \nabla^2(\psi_y) - \psi_y \nabla^2(\psi_x) - \frac{\partial}{\partial t} (\nabla^2\psi)] \delta\psi d\Omega. \tag{6}$$

Integrating Eq. (6) by parts twice for the viscous term and once for the convective and the time dependent terms and employing the Green-Gauss theorem yields the following variational statement:

$$\begin{aligned} \delta_{\psi} I_1 = \iint_{\Omega} [&\frac{1}{Re} \nabla^2\psi\nabla^2\delta\psi + (\psi_y^\circ \nabla^2\psi^\circ)\ \delta\psi_x - (\psi_x^\circ \nabla^2\psi^\circ)\ \delta\psi_y \\ &+ \nabla\psi_t^\circ \nabla\delta\psi]\ d\Omega + \oint_{\Gamma} [\frac{1}{Re} \frac{\partial(\nabla^2\psi)}{\partial n} - \nabla^2\psi^\circ \underline{n} x \nabla\psi^\circ \\ &- \frac{\partial}{\partial t} (\frac{\partial(\nabla\psi^\circ)}{\partial n})]\ \delta\psi d\Gamma - \frac{1}{Re} \oint_{\Gamma} \nabla^2\psi \delta\psi_n d\Gamma \end{aligned} \tag{7}$$

where the notation $\delta_{\psi} I_1$ refers to variation in ψ only, while ψ° is kept fixed. After the variation ψ is set equal to ψ° and the governing differential equation (5) recovered as Euler equation.

If the variational operation δ is pulled in front of the integral expression, and the boundary integrals neglected for now, the following functional is obtained:

$$\begin{aligned} I_1(\psi,\psi^\circ) = \iint_{\Omega} [&\frac{1}{2Re} (\nabla^2\psi^2) + (\psi_y^\circ \nabla^2\psi^\circ)\ \psi_x \\ &- (\psi_x^\circ \nabla^2\psi^\circ)\ \psi_y + \nabla\psi_t^\circ \nabla\psi] d\Omega. \end{aligned} \tag{8}$$

This functional yields the boundary conditions:

$$\text{either } \delta\psi = 0 \quad \text{or} \quad -\frac{1}{Re}\nabla^2\psi_n + \nabla^2\psi\psi_s + \frac{\partial(\psi_n)}{\partial t} = 0 \tag{9}$$

$$\text{and either } \delta\psi_n = 0 \quad \text{or} \quad \zeta = \nabla^2\psi = 0 \tag{10}$$

where n is the direction of the outward normal on the boundary, and s is the direction tangential to the boundary, and ζ represents the vorticity. The left hand side conditions are the logical 'rigid' boundary conditionss corresponding to specified stream function and its normal derivative. The 'natural' boundary conditions on the right hand side are not the ones that we would like to have, namely those of constant pressure and zero shear stress.

These boundary conditions can be easily implemented though, by simply adding the appropriate boundary integrals to the functional Eq. (8). As we use triangular finite elements to be covered in more detail later, the boundary integrals are added in such a way, that the natural boundary conditions can be approximated only on one edge of the triangle. This effectively means that only if a particular finite element is to be used as boundary element with two of its vertices lying on the part of the boundary, where any one or both 'natural' boundary conditions are prescribed, these boundary integrals are added.

In order to simplify the equations we switch now to local coordinates ξ,η as shown in Fig. (1), and obtain the modified governing functional as:

$$I^e(\psi,\psi^\circ) = \iint_{\Omega^e} [\frac{1}{2Re}(\nabla^2\psi) - (\psi^\circ_\xi\nabla^2\psi^\circ)\,\psi_\eta + (\psi^\circ_\eta\nabla^2\psi^\circ)\,\psi_\xi \tag{11}$$

$$+ \nabla\psi^\circ_t\nabla\psi]\, d_\xi d_\eta + \int_{-b}^{a} [\frac{2}{Re}\psi^\circ_{\xi\xi}\psi_\eta - (\psi^\circ_\xi\psi^\circ_{\xi\xi} + \psi^\circ_\eta\psi^\circ_{\xi\eta})\psi]_{\eta=0}\, d\xi.$$

The functional yields the 'rigid' boundary conditions:

$$\delta\psi = 0 \quad \text{and} \quad \delta\psi_\eta = 0 \tag{12}$$

and the 'natural' boundary conditions:

$$p_\xi = \psi_{\eta t} - \frac{1}{Re}(\psi_{\xi\xi\eta} + \psi_{\eta\eta\eta}) + \psi_\eta\psi_{\xi\eta} - \psi_\xi\psi_{\eta\eta} = 0 \tag{13}$$

$$\text{and } \tau = \frac{1}{Re}(\psi_{\eta\eta} - \psi_{\xi\xi}) = 0.$$

Both 'rigid' boundary conditions can be exactly satisfied for a straight boundary, since stream function is uniquely determined by ψ, ψ_ξ and $\psi_{\xi\xi}$ at the two vertices lying on the boundary, and its normal derivative, a cubic, is uniquely determined by ψ_η and $\psi_{\eta\xi}$ at these vertices. For curved boundaries, however, special provisions are necessary, and the desired boundary conditions are realized exactly only at discrete nodes. These provisions in the element area integrations are included in this work, but they will not be reported, as they are well documented in Tuann and Olson [5,6].

CHAPTER 3

Finite Element Formulation

By performing the aforementioned integration by parts the order of the function space is lowered. This relaxation of the continuity requirements on the stream function is referred to as a 'weak' formulation of the problem. It permits us to seek the solution in the Sobolev space W_2, which contains all functions, whose second derivatives are square integrable, i.e. finite. In other words using classical finite element vocabulary we need a finite element of C^1 class. Such an element satisfies the 'compatibility' conditions, as it provides interelement continuity of ψ and its normal derivative and the governing functional contains derivatives of at most second order.

In this chapter the derivation of the functional for an element of C^1 class is presented. The procedure of finding the extremum of the global functional resulting in the discretized equations of motion is indicated.

3.1 Functional on Element Level

Here the triangular element derived by Cowper et al. [7] is adopted. This element has since been recognized as one of the most accurate finite elements available for plate bending problems, Gallagher [8]. It should be noted, though, that this element requires a substantial formulative effort. Olson was the first to modify it for application to the steady state two-dimensional viscous flow problems. Only the relevant steps in the element derivation are included and for more details it is referred to Olson [1,3].

The element and its nodal variables are shown in Fig. (2). The

field variable is interpolated within the element by a truncated quintic polynomial:

$$\psi = \sum_{i=1}^{20} a_i \xi^{m_i} \eta^{n_i} \tag{14}$$

such that tangential velocity component along the edge 1-2 is a cubic in ξ. Eighteen relations expressing nodal variables $\underline{\psi}_1$ in terms of polynomial coefficients $\underline{A}$ can be established by differentiating ψ with respect to the ξ,η coordinates and by substituting the local coordinates of the vertices. Two additional relations are obtained by constraining the tangential velocity to vary as a cubic along the remaining two edges, 2-3 and 3-1. This is written in matrix form as:

$$<\underline{\psi}_1,0,0^T> = \underline{\underline{T}}\ \underline{A} \tag{15}$$

Inverting the above equation the vector of polynomial coefficient $\underline{A}$ can be expressed in terms of the vector of nodal variables $\underline{\psi}_1$ as:

$$\underline{A} = \underline{\underline{T}}^{-1}<\underline{\psi}_1,0,0>^T = \underline{\underline{T}}_2\underline{\psi}_1 \tag{16}$$

where $\underline{\underline{T}}_2$ is 20 x 18 matrix consisting of the first 18 columns of $\underline{\underline{T}}^{-1}$.

The introduction of the transformation from local coordinates ξ,η to global coordinates x,y in the form:

$$\underline{\psi}_1 = \underline{\underline{R}}\ \underline{\psi} \tag{17}$$

where $\underline{\psi}$ is the vector of nodal variables in the global coordinate system into Eq. (16) yields the following relation between $\underline{\psi}$ and A:

$$\underline{A} = \underline{\underline{T}}_2\underline{\underline{R}}\underline{\psi} = \underline{\underline{S}}\ \underline{\psi}. \tag{18}$$

The element matrices are then obtained by substituting Eq. (14) into the governing functional Eq. (11) and carrying out the integrations. It should be noted, that the terms in the functional are first arranged in such a way, that the resulting arrays are symmetric in their first two indices. The functional on the element level can then be written in discretized form as:

$$I^e(\underline{\psi},\underline{\psi}^\circ) = \frac{1}{Re} K^e_{kj}\psi_k\psi_j + Q^e_{ijk}\psi^\circ_i\psi^\circ_j\psi_k + M^e_{kj}\psi_k\dot{\psi}^\circ_j \tag{19}$$

where

$$K^e_{kj} = S_{rk}S_{sj}k_{rs} \tag{20}$$

is the element linear dissipative matrix

$$Q^e_{ijk} = S_{rk}S_{sj}S_{ti}q_{rst} \tag{21}$$

is the element nonlinear convective matrix and

$$M^e_{kj} = S_{rk}S_{sj}\ell_{rs} \tag{22}$$

is the element consistent mass matrix, and $\dot{\psi}$ represents a time derivative. In the above equations i,j,k take values from 1 to 18, and r,s,t from 1 to 20, respectively. The other arrays appearing in these equations are defined as:

$$\begin{aligned} k_{rs} = {} & m_r m_s (m_r - 1)(n_r - 1)(m_s - 1)(n_s - 1) \times F(m_r + m_s - 4, n_r + n_s) \\ & + n_r n_s (n_r - 1)(n_s - 1) \times F(m_r + m_s, n_r + n_s - 4) \\ & + [m_r n_s (m_r - 1)(n_s - 1) + m_s n_r (m_s - 1)(n_r - 1)] \\ & \times F(m_r + m_s - 2, n_r + n_s - 2) + [m_r n_s (m_r - 1) \\ & + m_s n_r (m_s - 1)] \times G(m_r + m_s - 2, n_r + n_s - 1) \end{aligned} \tag{23}$$

$$q_{rst} = \frac{1}{2}(n_r m_t - m_r n_t)\, m_s (m_s - 1) + (n_s m_t - m_s n_t)\, m_r (m_r - 1)$$

$$\times F(m_r + m_s + m_t - 3,\ n_r + n_s + n_t) + \frac{1}{2}(n_r m_t - m_r n_t)\, n_s (n_s - 1)$$

$$+ (n_s m_t - m_s n_t)\, n_r (n_r - 1) \times F(m_r + m_s + m_t - 1,\ n_r + n_s + n_t - 3)$$

$$- \frac{1}{2} m_r m_s (m_r + m_s + m_t - 2) \times G(m_r + m_s + m_t - 3,\ n_r + n_s + n_t)$$

$$- \frac{1}{2} n_r n_s (m_r + m_s) \times G(m_r + m_s + m_t - 1,\ n_r + n_s + n_t - 2) \qquad (24)$$

$$\ell_{rs} = m_r m_s \times F(m_r + m_s - 2,\ n_r + n_s) + n_r n_s \times F(m_r + m_s,\ n_r + n_s$$

$$- 2) \qquad (25)$$

where F and G represent the exact integral formulas obtained by carrying out the integrations of the general term $\xi^m \eta^n$ over the area of the triangle and along the $\eta = 0$ edge, respectively.

$$F(m,n) = c^{m+1}[(a)^{m+1} - (-b)^{m+1}]\frac{m!n!}{(m + n + 2)!} \qquad (26)$$

$$G(m,n) = \frac{1}{m+1}[(a)^{m+1} - (-b)^{m+1}] \quad \text{if } n = 0$$

$$G(m,n) = 0 \quad \text{if } n \neq 0. \qquad (27)$$

3.2 Global Functional

The global governing functional for the entire problem in discretized form is obtained by following the usual finite element assemblage process. That is, the element matrices are appropriately summed into the global matrices, taking into account the symmetry and bandedness properties. The homogeneous boundary conditions are introduced during the process as well, by simply striking out rows and columns of the global

arrays corresponding to the variables on the boundary with specified zero value. The problem obtained in that manner, that is, the problem of the order equal to the number of the nonzero nodal variables will be referred to as the 'net' problem. It should be noted, that so far, the nonhomogeneous boundary conditions have not been taken into account.

The aforementioned functional can be written as:

$$I(\underline{\psi},\underline{\psi}^\circ) = \frac{1}{Re} K_{kj}\psi_j\psi_k + Q_{ijk}\psi_i^\circ\psi_j^\circ\psi_k + M_{kj}\dot{\psi}_j^\circ\psi_k \qquad (28)$$

$$i,j,k = 1, \ldots, r$$

where r is the''net' problem size, and $\underline{\psi}$ and $\underline{\psi}^\circ$ represent the global vectors of nonzero nodal variables. The global dissipative matrix K_{kj} and the global consistent mass matrix M_{kj} are each stored columnwise in an one-dimensional array of size lb. x r. The nonlinear convective matrix Q_{ijk} is also stored in full, because it was found to be numerically more efficient, than to recalculate it element by element. The matrix cannot be accommodated in the core, because of its size, so it is stored slice by slice columnwise in the order of the index k on the high speed disk. Each one-dimensional slice is of size lb x (2 lb - 1), or lb x r, depending on whether the 'net' size of the problem is bigger or smaller than the bandwidth 2 lb - 1. The half-bandwidth of the problem is defined as lb.

The procedure of seeking the extremum of the global functional Eq. (28) with respect to $\underline{\psi}$, while keeping $\underline{\psi}^\circ$ fixed, yields:

$$\delta_\psi I = (\frac{1}{Re} K_{kj}\psi_j + Q_{ijk}\psi_i^\circ\psi_j^\circ + M_{kj}\dot{\psi}_j^\circ)\ \delta\psi_k = 0 \qquad (29)$$

where the indices, appearing as subscripts, i, j, and k take on, successively, values from 1 to r, as before.

The restricted variational principle now permits to replace

$\underline{\psi}^{\circ}$ by $\underline{\psi}$ and as $\delta\psi_k$ is arbitrary, the set of first order nonlinear differential equations in discrete form for the r global variables ψ is obtained:

$$\frac{1}{Re} K_{kj}\psi_j + Q_{ijk}\psi_i\psi_j + M_{kj}\dot{\psi}_j = 0 \tag{30}$$

where the indices take on successively the same values, as in the previous two equations.

The functional Eq. (28), or alternatively the system of differential equations Eq. (30), will serve as the basis for employing modal approach.

CHAPTER 4

Modal Approach

The idea to employ modal approach originates in the field of structural dynamics where this approach has been applied successfully for years to linear and mildly nonlinear problems and recently extended to cover strongly nonlinear problems.

In the category of linear structural dynamics problems the advantages of modal approach are quite obvious. Not only do the equations of motion uncouple, under the assumption that damping matrix can be represented as a linear combination of stiffness and mass matrices, but also, due to the fact that most of the frequency content of the loading is contained in the lowest modes for many types of practical loadings, only a fraction of the total number of uncoupled equations in generalized coordinates need be considered in order to obtain a reasonable approximation to the actual response of the system [9].

We define mildly nonlinear systems as those systems for which nonlinear deformation mechanisms do not cause major changes in the deflection patterns. For these systems the equations of motion are no longer uncoupled due to off-diagonal terms appearing in the generalized stiffness matrix. The response may still be evaluated, though, by direct integration of a limited set of equations of motion in generalized coordinates.

In the category of strongly nonlinear problems modal analysis has been tried, to my knowledge, only by Nickel [10]. He casts the dynamic equations in the incremental form. After finding the initial modes and frequencies he proceeds to compute the subsequent modal spectrum for nonlinear states, employing an extremely fast and efficient eigenproblem solver that involves matrix multiplications only and uses the most recently computed

spectrum as initial estimate. So he obtains the equations of motion in the uncoupled form even when strong nonlinearities are present. The advantage of his procedure gets more pronounced as the bandwidth of the problem in the original finite element coordinates increases. It should be noted though, that again the assumption is made, that the lowest natural frequencies and associated modes dominate the incremental motion. This assumption, which is essentially equivalent to the previous statement, that the frequency content of the loading is contained the lowest modes, is empirically verified for great many structural dynamics problems, notably those of earthquake excitation.

Had the same been true for the problems of fluid dynamics, we would have tried to perform the modal decomposition for nonlinear states as well, employing only the lowest modes. Unfortunately, prior to this work nothing was known about the application of modal analysis to fluids. So the first fundamental question that we have attempted to answer was how many modes were to be included in order to obtain a reasonable solution. That is why we intentionally restricted the class of the problems that we have been trying to solve to mildly nonlinear problems, that is, to the range of low to moderate Reynolds numbers. Thus we needed to perform the linear eigenvalue analysis only, but for all the modes. The eigenvalue analysis for the subsequent nonlinear states, based upon the tangent matrix obtained as a linear combination of the linear viscous matrix and the nonlinear convective matrix, evaluated with stream function values at a previous time step, for all the modes, would have been prohibitively expensive, of course. The second fundamental question that we have tried to answer was, what was the maximum Reynolds number governing the nonlinear behaviour, for which the linear modes could still predict the accurate enough solution.

In this chapter two procedures for employing modal analysis, transformation by condensation and transformation in conjunction with Lagrange multipliers technique will be presented. Both procedures shall in turn be applied, the first one to Eq. (30), the second one to the functional Eq. (28). It will be assumed, as already stated previously, that the homogeneous boundary conditions have been taken account of, but not the non-homogeneous ones. As a matter of fact, as must be obvious from Eq. (30), which is homogeneous, the only 'loading' comes precisely from these non-homogeneous boundary conditions, that is, from the prescribed nonzero variables on the boundary.

4.1 Transformation by Condensation

In the following derivation the indices appearing as subscripts i, j, and k take on successively values from 1 to s, where s is the total number of unconstrained variables equal to the size of the problem, which will be referred to as the 'net net' problem, the indices m and n values from 1 to p, where p is the number of constrained variables on the kinematic and mixed boundaries, and the indices α,β, and γ values from 1 to w, where w is the number of the eigenvectors used. Throughout the derivation it will be assumed that the number of the eigenvectors used w is equal to the size of the 'net net' problem, so that the equations of motions in the generalized coordinates are the exact equivalent of the same equations in finite element coordinates. Later in actual applications we shall obviously attempt to reduce the number of eigenvectors used.

The equations of motion will be written for the unconstrained variables only as follows:

$$M_{kj}\dot{\psi}_j + \frac{1}{Re} K_{kj}\psi_j + Q_{ijk}\psi_i\psi_j + M_{km}\psi_m + \frac{1}{Re} K_{km}\psi_m$$

$$+ Q_{njk}\psi_n\psi_j + Q_{imk}\psi_i\psi_m + Q_{nmk}\psi_n\psi_m = 0 \tag{31}$$

As there are p prescribed variables ψ_m and ψ_n the multiplications involving these variables may be performed. Taking advantage of the symmetry of the array Q in the first two subscripts i and j, we can write:

$$Q_{njk}\psi_n\psi_j + Q_{imk}\psi_i\psi_m = Q_{njk}\psi_n\psi_j + Q_{njk}\psi_n\psi_j = C_{jk}\psi_j. \tag{32}$$

By transposing all the known terms to the right hand side, the following set of equations is obtained:

$$M_{kj}\dot{\psi}_j + \frac{1}{Re} K_{kj}\psi_j + C_{jk}\psi_j + Q_{ijk}\psi_i\psi_j = F_k \tag{33}$$

where F_k can be viewed as the 'loading' term defined by:

$$F_k = -M_{km}\psi_m - \frac{1}{Re} K_{km}\psi_m - Q_{nmk}\psi_n\psi_m. \tag{34}$$

We now propose to transform Eq. (33) using the following transformation on the finite element stream function vector:

$$\psi_j (t) = E_{j\alpha} y_\alpha (t) \tag{35}$$

where $E_{j\alpha}$ is a square matrix and y_α (t) is a time dependent vector of the order s.

The matrix E is established by solving for:

$$M_{kj}\dot{\psi}_j + K_{kj}\psi_j = 0. \tag{36}$$

The solution can be postulated to be of the form:

$$\psi_j = \phi_j e^{-\lambda t} \tag{37}$$

where t is the time variable and λ is a constant defined to represent the time decay of the vector ϕ.

By substituting Eq. (37) into Eq. (36) the generalized eigenvalue problem is obtained, from which the eigenvectors $\underline{\phi}$ and the associated eigenvalues λ are to be determined:

$$\left(\frac{1}{Re} K_{kj} - M_{kj}\right) \phi_j = 0. \tag{38}$$

It is evident now that E is to be defined as a matrix whose columns are just the eigenvectors $\underline{\phi}$:

$$\underline{\underline{E}} = <\underline{\phi}_1, \underline{\phi}_2, \underline{\phi}_3, \ldots, \underline{\phi}_s>. \tag{39}$$

By introducing Eq. (35) into Eq. (33), we obtain:

$$M_{kj}E_{j\alpha}\dot{y}_\alpha + \frac{1}{Re} K_{kj}E_{j\alpha}y_\alpha + C_{jk}E_{j\alpha}y_\alpha + Q_{ijk}E_{i\beta}E_{j\alpha}y_\alpha y_\beta = F_k. \tag{40}$$

By multiplying the above equation by E_{kj} the equations of motion in the eigenvector basis are obtained in the form:

$$\begin{aligned} &M_{kj}E_{j\alpha}E_{k\gamma}\dot{y}_\alpha + \frac{1}{Re} K_{kj}E_{j\alpha}E_{k\gamma}y_\alpha + C_{jk}E_{j\alpha}E_{k\gamma}y_\alpha \\ &+ Q_{ijk}E_{i\beta}E_{j\alpha}E_{k\gamma}y_\alpha y_\beta = F_k E_{k\gamma}. \end{aligned} \tag{41}$$

The above equation can be simplified taking into account the orthonormal properties of the eigenvectors with respect to the mass matrix M_{kj}. These properties can be expressed as follows:

$$
\begin{aligned}
M_{kj}E_{k\gamma}E_{j\alpha} &= 1 && \text{if } \gamma = \alpha \\
M_{kj}E_{k\gamma}E_{j\alpha} &= 0 && \text{if } \gamma \neq \alpha \\
K_{kj}E_{k\gamma}E_{j\alpha} &= \lambda_{\gamma} && \text{if } \gamma = \alpha\gamma \\
K_{kj}E_{k\gamma}E_{j\alpha} &= 0 && \text{if } \gamma \neq \alpha.
\end{aligned} \tag{42}
$$

The equation of motion for the o-th generalized coordinate y_o can then be written as:

$$
\dot{y}_o + \frac{1}{Re}\lambda_o y_o + C_{jk}E_{j\lambda}E_{j\gamma}y_\alpha + Q_{ijk}E_{i\beta}E_{j\alpha}E_{ko}y_\alpha y_\beta = F_k E_{ko} \tag{43}
$$

or in the matrix form for the whole system:

$$
\underline{\underline{I}}\dot{\underline{y}} + \frac{1}{Re}\underline{\underline{\lambda}}\underline{y} + \underline{\underline{\bar{C}}}\underline{y} + \underline{\underline{\bar{Q}}}\underline{y}\underline{y} = \underline{\bar{F}} \tag{44}
$$

where $\underline{\underline{I}}$ is the identity matrix, $\dot{\underline{y}}$ is the vector of first order time derivatives of generalized coordinates, $\underline{\underline{\lambda}}$ is the diagonal matrix of eigenvalues, $\underline{y}$ is the vector of generalized coordinates, $\underline{\underline{\bar{C}}} = \underline{\underline{E}}^T\underline{\underline{C}}\underline{\underline{E}}$ is the square matrix, $\underline{\bar{Q}} = \underline{\underline{E}}^T\underline{\underline{Q}}\underline{\underline{E}}\underline{\underline{E}}$ is the condensed nonlinear convective matrix, and $\underline{\bar{F}} = \underline{\underline{E}}^T\underline{F}$ is the load vector.

It should be noted that the procedure laid out above is completely analogous to the treatment of an arbitrary support excitation in structural dynamics. This transformation by condensation procedure seems quite appealing. It uses the classical eigenvectors which satisfy the homogeneous boundary conditions only. Unfortunately we have to deal with the nonlinear convective matrix, as well. Although it is numerically quite easy to code an integer vector to keep track of the prescribed values of the stream function on the boundary, even the process of forming the nonlinear matrix in the finite element coordinates is an extremely complicated one, and breaking

this matrix into four different arrays, as indicated in Eq. (31), to carry out the multiplications of Eqs. (32) and (34), seemed quite hopeless. It is because of these numerical difficulties that the procedure had to be abandoned and we concentrated instead on the transformation in conjunction with Lagrange multipliers technique.

4.2 Transformation in Conjunction with Lagrange Multipliers Technique

In this derivation the indices i, j, and k take on successively values from 1 to r, where r is the size of the 'net' problem, the index m values from 1 to p, where p is the number of constrained variables on the kinematic and mixed boundaries, and the indices α,β, and γ values from 1 to w, where w is the number of eigenvectors used to approximate the solution. Throughout the derivation w will be taken equal to the size of the 'net' problem r in order to obtain the exact equivalent of the formulation of the problem in the finite element coordinates.

The p linear constraints imposed upon the stream function can be expressed in the form:

$$G_{mk}\psi_k - T_m = 0 \tag{45}$$

where G_{mk} is the rectangular matrix of constraints of size p x r with all the entries equal to zero except for the diagonal entries corresponding to the prescribed values of the stream function on the boundary, ψ_k is the vector of stream function variables of size r, and T_m is the vector of these prescribed values of the stream function on the boundary of size p.

Then Eq. (45), multiplied by the vector of Lagrange multipliers h of size p, is added to the global functional Eq. (28) and the augmented functional obtained in the form:

$$I(\underline{\psi},\underline{\psi}^{\circ},\underline{h}) = \frac{1}{Re} K_{kj}\psi_j\psi_k + Q_{ijk}\psi_i^{\circ}\psi_j^{\circ}\psi_k + M_{kj}\dot{\psi}_j^{\circ}\psi_k$$

$$+ G_{mk}\psi_k h_m - T_m h_m = 0. \tag{46}$$

The variation of the augmented functional defined by the above equation, first with respect to $\underline{\psi}$ while keeping $\underline{\psi}^{\circ}$ and $\underline{h}$ fixed and then with respect to $\underline{h}$ while keeping $\underline{\psi}$ and $\underline{\psi}^{\circ}$ fixed, yields:

$$\frac{\partial I}{\partial \psi_k} = M_{kj}\dot{\psi}_j + \frac{1}{Re} K_{kj}\psi_j + Q_{ijk}\psi_i\psi_j + G_{mk}h_m = 0$$

$$\frac{\partial I}{\partial h_m} = G_{mj}\psi_j - T_m = 0 \tag{47}$$

where in the first subset of the above set of equations $\underline{\psi}^{\circ}$ has been replaced by $\underline{\psi}$ as permitted by the restricted variational principle, and in the second subset the dummy subscript k has been replaced by j.

By employing the coordinate transformation indicated in Eq. (35), with the matrix $\underline{\underline{E}}$ established via Eqs. (36) to (39), and by introducing this transformation into Eq. (47) we obtain:

$$M_{kj}E_{j\alpha}\dot{y}_{\alpha} + \frac{1}{Re} K_{kj}E_{j\alpha}y_{\alpha} + Q_{ijk}E_{i\beta}E_{j\alpha}y_{\alpha}y_{\beta} + G_{mk}h_m = 0$$

$$G_{mj}E_{j\alpha}y_{\alpha} - T_m = 0. \tag{48}$$

By multiplying the first subset of the above set of equations by $E_{k\gamma}$ and by taking advantage of the orthonormality properties of the eigenvectors with respect to the mass matrix M_{kj} as expressed in Eq. (42) the following system of equations is obtained:

$$\dot{y}_{\gamma} + \frac{1}{Re} \lambda_{\gamma}y_{\gamma} + Q_{ijk}E_{i\beta}E_{j\alpha}E_{k\gamma}y_{\alpha}y_{\beta} + G_{mk}E_{k\gamma}h_m = 0$$

$$G_{mj}E_{j\alpha}y_{\alpha} - T_m = 0 \tag{49}$$

or in the matrix form:

$$\begin{aligned} \underline{\underline{I}}\dot{\underline{y}} + \underline{\underline{\lambda}}\underline{y} + \underline{\underline{\bar{Q}}}\underline{y}\underline{y} + \underline{\underline{\bar{E}}}^{T}\underline{h} &= 0 \\ \underline{\underline{\bar{E}}}\underline{y} - \underline{T} &= 0 \end{aligned} \tag{50}$$

where $\underline{\underline{I}}$ is the identity matrix, $\underline{\underline{\lambda}}$ is the diagonal matrix of eigenvalues, $\underline{\underline{\bar{Q}}} = \underline{\underline{E}}^{T}\underline{\underline{Q}}\underline{\underline{E}}\underline{\underline{E}}$ is the transformed nonlinear convective matrix, $\underline{\underline{E}}$ is the matrix of eigenvectors, and $\underline{\underline{\bar{E}}}^{T} = \underline{\underline{E}}\underline{G}$ is the matrix consisting of the entries in eigenvectors at the constrained degrees of freedom. The matrices $\underline{\underline{I}}$ and $\underline{\underline{\lambda}}$ are each of size w x w, the matrix $\underline{\underline{\bar{Q}}}$ is of size w x w x w, and the matrix $\underline{\underline{\bar{E}}}$ is of size p x w.

4.3 Final Remarks

It should be emphasized again, that while in the first method, the transformation by condensation, the general eigenvalue analysis is run after the nonhomogeneous boundary conditions have been taken account of, in the second method employing Lagrange multipliers technique the generalized eigenvalue analysis is run prior to taking account of the given values of stream function on the boundary. Also, the first method contracts the size of the system of equations to be solved to s = r - p, while the second method expands the size to q = r + p, where r is the 'net' problem size, and p is the number of constraints. This does not effect our choice of the second method to a great extent, however, because in the fluid problems the number of constraints is relatively small compared to the size r and it can be further reduced by our numerical procedure through the use of 'master slave' option.

If the number of eigenvectors is equal to the number of finite

element degrees of freedom, mathematically the same space is spanned by the eigenvectors as by the nodal point finite element stream function variables and consequently the same solution must be obtained by both analyses. But, employing all the eigenvectors of the linear eigenvalue problem, would actually be a step backward, because although the global consistent mass matrix and the linear global dissipative matrix become uncoupled, the equations in generalized coordinates are still coupled through the global nonlinear convective matrix, which becomes full, whereas it was banded in finite element coordinates. So, the modal approach can only be more efficient, if a reasonable approximation of the solution of finite element equations of motion Eq. (30) can be obtained by using a significantly reduced number of eigenvectors. We note, that so far we have only been concerned with the exact and approximate solutions of these discrete equations. Whether a good approximation to the solution of the actual continuum problem will be obtained, depends on the finite elements employed, the finite element meshes, and the boundary conditions.

CHAPTER 5

Solution of Nonlinear Equations in Time Dependent and Steady State Analyses

It is appropriate to note here, that in the classical computational fluid dynamics, based on finite differences, the studies of even steady state problems are mostly based on the time dependent equations, because, firstly, this time dependent approach does not postulate the existence of a steady state solution, secondly, the procedure is more flexible in the sense, that the transient solution can be achieved, if so desired, and thirdly and most important, the unsteady equations in finite differences are easier to handle and more stable than their steady counterparts. The steady state solution is obtained, if it exists, as the asymptotic limit of the time integration.

In the finite element discretization of fluid dynamics problems, the contrary seems to be true, that is, it is computationally more efficient to seek the steady state solution only, if the transient solutions are of no interest. As we are also confident, that the steady state solutions for the problems, that we intend to solve, do exist, and indeed, excellent results have been obtained employing the same boundary conditions, the same 18 d.o.f. triangular finite elements, and the same finite element meshes by Olson [3], and Tuann and Olson [5,6], we shall implement the time dependent, but also the steady state approach. The time dependent approach will be used only for the numerical study of the flow around a circular cylinder, where the transient solutions are desired, as oscillatory behaviour is to be expected at the critical value of the Reynolds number.

As we propose to solve the governing set of nonlinear equations in generalized coordinates Eq. (50) simultaneously, rather than to attempt

a partitioned solution, we shall first cast Eq. (50) in the form of one nonlinear time dependent matrix equation as follows:

$$\begin{bmatrix} \underline{\underline{I}} & \underline{\underline{0}} \\ \underline{\underline{0}} & \underline{\underline{0}} \end{bmatrix} \begin{Bmatrix} \dot{\underline{y}} \\ \dot{\underline{h}} \end{Bmatrix} + \begin{bmatrix} \frac{1}{Re}\underline{\underline{\lambda}} & \underline{\underline{\bar{E}}}^T \\ \underline{\underline{E}} & \underline{\underline{0}} \end{bmatrix} \begin{Bmatrix} \underline{y} \\ \underline{h} \end{Bmatrix} + \begin{Bmatrix} \underline{\underline{\bar{Q}}}\ \underline{y}\ \underline{y} \\ -\underline{T} \end{Bmatrix} = \underline{0}. \quad (51)$$

Then the time dependent approach shall be applied directly to the above equation, while the steady state approach shall be applied to the steady equivalent of the same equation obtained by simply setting the time dependent term equal to zero.

5.1 Time Dependent Approach

We shall assume linear time dependence of the vector of generalized coordinates $\underline{y}$ over the time interval t, which can be written as:

$$\underline{y}\ (\tau) = \underline{y}_t + \frac{\tau - t}{\Delta t}\ (\underline{y}_{t+\Delta t} - \underline{y}_t). \quad (52)$$

Differentiating the above equation with respect to τ, we obtain:

$$\dot{\underline{y}}\ (\tau) = \frac{1}{\Delta t}\ (\underline{y}_{t+\Delta t} - \underline{y}_t) \quad (53)$$

or evaluating at time $\tau = t + \Delta t$

$$\dot{\underline{y}}\ (t + \Delta t) = \frac{1}{\Delta t}\ (\underline{y}_{t+\Delta t} - \underline{y}_t). \quad (54)$$

We note, that the above equation represents a backward finite difference scheme, which is unconditionally stable for linear problems. This very useful feature cannot be ascertained for nonlinear problems, however, and consequently the critical time step for those problems must be determined by numerical experiments.

If we introduce Eq. (54) into Eq. (51), evaluate at time t+Δt, and add the appropriate terms, we obtain the following set of now algebraic nonlinear equations:

$$\begin{bmatrix} \frac{1}{\Delta t}\underline{\underline{I}} + \frac{1}{Re}\underline{\underline{\lambda}} & \underline{\underline{E}}^T \\ \underline{\underline{E}} & \underline{\underline{0}} \end{bmatrix} \begin{Bmatrix} \underline{y}_{t+\Delta t} \\ \underline{h}_{t+\Delta t} \end{Bmatrix} + \begin{Bmatrix} \underline{\underline{\bar{Q}}}\underline{y}_{t+\Delta t}\underline{y}_{t+\Delta t} \\ \underline{0} \end{Bmatrix}_t = \begin{Bmatrix} \frac{1}{\Delta t}\underline{y}_t \\ \underline{T}_{t+\Delta t} \end{Bmatrix} . \quad (55)$$

Three time integration algorithms shall in turn be applied to the above equation. These algorithms differ only in how the nonlinear term is treated. All of them are quite crude, but relatively cheap, and we consider them sufficient for this work.

In the first algorithm we simply evaluate the nonlinear term for the previous time step and move it to the right hand side to obtain:

$$\begin{bmatrix} \frac{1}{\Delta t}\underline{\underline{I}} + \frac{1}{Re}\underline{\underline{\lambda}} & \underline{\underline{E}}^T \\ \underline{\underline{E}} & \underline{\underline{0}} \end{bmatrix} \begin{Bmatrix} \underline{y}_{t+\Delta t} \\ \underline{h}_{t+\Delta t} \end{Bmatrix} = \begin{Bmatrix} \frac{1}{\Delta t}\underline{y}_t - \underline{\underline{\bar{Q}}}\underline{y}_t\underline{y}_t \\ \underline{T}_{t+\Delta t} \end{Bmatrix} . \quad (56)$$

The system matrix of the above set of linear equations is square, real, symmetric, and nonsingular, but it has an associated quadratic form which is indefinite, so that Cholesky decomposition cannot be used. As this matrix remains constant it needs be inverted only once and for the consecutive steps only the backsubstitution has to be performed.

In the second procedure the nonlinear term is evaluated as $\underline{\underline{Q}}\,\bar{\underline{y}}_t\bar{\underline{y}}_{t+\Delta t}$, so that the following system of linear equations for the generalized coordinates $\bar{\underline{y}}$ and $\underline{h}$ is obtained:

$$\begin{bmatrix} \frac{1}{\Delta t}\underline{\underline{I}} + \frac{1}{Re}\underline{\underline{\lambda}} + \underline{\underline{\bar{Q}}}\underline{y}_t & \underline{\underline{\bar{E}}}^T \\ \underline{\underline{\bar{E}}} & \underline{\underline{0}} \end{bmatrix} \begin{Bmatrix} \underline{y}_{t+\Delta t} \\ \underline{h}_{t+\Delta t} \end{Bmatrix} = \begin{Bmatrix} \frac{1}{\Delta t}\underline{\underline{I}}\underline{y}_t \\ \underline{T}_{t+\Delta t} \end{Bmatrix} \tag{57}$$

It should be noted, that the nonlinear term is treated in the above algorithm in the same way as an Picard iteration or the method of successive substitution. Here the iterations shall not be performed, because the cost would be quite high, and consequently the dynamic equilibrium is again not exactly satisfied. The algorithm can be very easily modified, though, to incorporate the iterative procedure. The system matrix, which has now become unsymmetric, has to be updated at each time step, but that allows the use of much larger time step than in the first algorithm. As a matter of fact, our experience has been that this second algorithm is numerically more efficient.

In the third algorithm, following a proposal by Stricklin et. al. [11], the nonlinear term is treated by transposing it to the right hand side as additional 'pseudoload' vector, similarly as in the first algorithm. But then the whole right hand side including the nonlinear term is expanded into a first order Taylor series about the previous time step. Denoting the right hand side vector as $\underline{F}$, defined as:

$$\underline{F}_t = \begin{Bmatrix} \frac{1}{\Delta t}\underline{y}_{t-1} - \underline{\underline{\bar{Q}}}_t\underline{y}_t \\ \underline{T}_t \end{Bmatrix} \tag{58}$$

we can write:

$$\underline{F}_{t+\bar{t}} = \underline{F}_t + \Delta t \frac{\partial}{\partial t}\underline{F}_t. \tag{59}$$

By using a first order backward difference expression to approximate the time derivative in the above equation, it becomes:

$$\underline{F}_{t+1} = 2\underline{F}_t - \underline{F}_{t-1}. \tag{60}$$

We note, that the use of Eq. (59) corresponds to a linear extrapolation of the 'loads' at the two previous time steps. By introducing Eq. (60) into Eq. (55), it can be written as:

$$\begin{bmatrix} \frac{1}{\Delta t}\underline{\underline{I}} + \frac{1}{Re}\underline{\underline{\lambda}} & \underline{\underline{E}}^T \\ \underline{\underline{E}} & \underline{\underline{0}} \end{bmatrix} \begin{Bmatrix} \underline{y}_{t+\Delta t} \\ \underline{h}_{t+\Delta t} \end{Bmatrix} = \underline{F}_{t+\Delta t}. \tag{61}$$

The above procedure cannot be started directly, so we start it by solving for the first two time steps with the first algorithm.

In all three algorithms a test is included on whether the steady state has been achieved.

In the first algorithm all the entries in the two consecutive solution vectors are successively scanned, and if none of the absolute differences in the two entries corresponding to the same coordinate exceeds a preassigned value, we assume that the steady state has been achieved.

In the second algorithm the steady state has been obtained if the test on the two consecutive determinants of the system matrix of Eq. (57)

$$\frac{|D^{t+\Delta t} - D^t|}{D^t} < \varepsilon \tag{62}$$

is satisfied, where ε is a preassigned small value.

In the third procedure the entries in the two consecutive 'load' vectors are compared and the maximum absolute difference in the two entries

corresponding to the same coordinate is found. Then if this maximum difference is smaller than a prescribed small value, we assume that the steady state solution has been achieved.

5.2 Steady State Approach

We propose to solve the steady equivalent of Eq. (51) by Newton-Raphson method, which seeks to exactly satisfy the equations of equilibrium by iterating until a specified level of accuracy is attained. We denote an approximate vector of generalized coordinates as $\underline{y}$ and an approximate vector of Lagrange multipliers by $\underline{h}$. Then the vector of residuals $\underline{F}(\underline{y},\underline{h})$ may be written as:

$$\underline{F}(\underline{y},\underline{h}) = \begin{bmatrix} \frac{1}{Re}\underline{\underline{\lambda}} & \underline{\underline{E}}^T \\ \underline{\underline{E}} & \underline{\underline{0}} \end{bmatrix} \begin{Bmatrix} \underline{y} \\ \underline{h} \end{Bmatrix} + \begin{Bmatrix} \underline{\underline{Q}}\underline{y}\underline{y} \\ -\underline{T} \end{Bmatrix} . \tag{63}$$

A Taylor series expansion of the vector of residuals around the position $(\underline{y},\underline{h})$ yields the following expression for the vector of residuals at an adjacent state $(\underline{y} + \Delta\underline{y},\ \underline{h} + \Delta\underline{h})$

$$\underline{F}(\underline{y} + \Delta\underline{y},\ \underline{h} + \Delta\underline{h}) = \underline{F}(\underline{y},\underline{h}) + \frac{\partial \underline{F}}{\partial \underline{y}}\Delta\underline{y} + \frac{\partial \underline{F}}{\partial \underline{h}}\Delta\underline{h} + O[(\Delta\underline{y},\Delta\underline{h})^2]. \tag{64}$$

In the above equation the vector notation is used for simplicity. Partial derivatives may be written more rigorously as:

$$\frac{\partial \underline{F}}{\partial \underline{y}}\Delta\underline{y} = \frac{F_i}{y_j}\Delta y_j \quad \text{and} \quad \frac{\partial \underline{F}}{\partial \underline{h}}\Delta\underline{h} = \frac{F_i}{h_k}\Delta h_k \tag{65}$$

where the index i takes on successively values from 1 to w+p, the index j values from 1 to w, and the index k values from 1 to p, where w is the number of eigenvectors used, and p is the number of constraints in the problem.

The conventional Newton-Raphson procedure retains only the terms up to the first order partial derivatives in the Taylor expansion Eq. (64). We assume, in addition, that the vector of residuals corresponding to the state ($\underline{y} + \Delta\underline{y}$, $\underline{h} + \Delta\underline{h}$) is zero. These assumptions allow to rewrite Eq. (64) as:

$$\underline{F}(\underline{y},\underline{h}) + \frac{\partial \underline{F}}{\partial \underline{y}}\Delta\underline{y} + \frac{\partial \underline{F}}{\partial \underline{h}}\Delta\underline{h} = \underline{0}. \tag{66}$$

The partial derivatives appearing in the above equation may be obtained by differentiating the steady equivalent of Eq. (51), as follows:

$$\frac{\partial \underline{F}}{\partial \underline{y}}\Delta\underline{y} + \frac{\partial \underline{F}}{\partial \underline{h}}\Delta\underline{h} = \begin{bmatrix} \frac{1}{Re}\underline{\underline{\lambda}} + 2\underline{\underline{\bar{Q}}}\underline{y} & \underline{\underline{\bar{E}}}^T \\ \underline{\underline{\bar{E}}} & \underline{\underline{0}} \end{bmatrix} \begin{Bmatrix} \Delta\underline{y} \\ \Delta\underline{h} \end{Bmatrix}. \tag{67}$$

By introducing Eqs. (63) and (67) into Eq. (66) we obtain the following system of linear equations:

$$\begin{bmatrix} \frac{1}{Re}\underline{\underline{\lambda}} + 2\underline{\underline{\bar{Q}}}\underline{y} & \underline{\underline{\bar{E}}}^T \\ \underline{\underline{\bar{E}}} & \underline{\underline{0}} \end{bmatrix} \begin{Bmatrix} \Delta\underline{y} \\ \Delta\underline{h} \end{Bmatrix}_{n+1} = - \begin{bmatrix} \frac{1}{Re}\underline{\underline{\lambda}} & \underline{\underline{\bar{E}}}^T \\ \underline{\underline{\bar{E}}} & \underline{\underline{0}} \end{bmatrix} \begin{Bmatrix} \underline{y} \\ \underline{h} \end{Bmatrix}_n - \begin{Bmatrix} \underline{\underline{\bar{Q}}}\underline{y}\underline{y} \\ \underline{T} - \underline{\underline{\bar{E}}}^T\underline{y} \end{Bmatrix}_n \tag{68}$$

where n is the iteration number.

The above equation is solved to determine the (n+1) increments in generalized coordinates and Lagrange multipliers. These increments are then used to determine an improved vector of generalized coordinates

$\underline{y}_{n+1}$, and an improved vector of Lagrange multipliers $\underline{h}_{n+1}$, where:

$$\begin{aligned} \underline{y}_{n+1} &= \underline{y}_n + \Delta\underline{y}_{n+1} \\ \underline{h}_{n+1} &= \underline{h}_n + \Delta\underline{h}_{n+1}. \end{aligned} \tag{69}$$

Equations (68) and (69) comprise the set of recurrence relations needed in the Newton-Raphson procedure.

Beginning with an initial estimate of the vectors $\underline{y}$ and $\underline{h}$, the equations (68) and (69) are successively applied to yield better and better approximation. The initial vector of generalized coordinates is obtained by transforming to the eigenvector basis the initial guess on the stream function vector, which consists of all zero entries except for the constrained ones, when the problem is started up with Re = 1.

The Jacobian of the system, that is, the determinant of the system matrix, is used as a test on the convergence of the procedure. At each iteration the Jacobian is recorded and compared with the Jacobian of the previous iteration. The process is stopped when the test

$$\frac{|\underline{J}^{n+1} - \underline{J}^n|}{|\underline{J}^n|} < \varepsilon \tag{70}$$

is satisfied, where ε is the preassigned accuracy criterion.

5.3 Final Remarks

In both transient and steady state analyses, after the generalized coordinates have been computed, the corresponding nodal stream function variables are obtained via Eq. (35). Then the stream function subvector, consisting of the stream function and its first and second derivatives, can be readily obtained at any point in the domain. It is done, element

by element, by computing the polynomial coefficients for the element under consideration using Eq. (18), then calculating the stream function subvector in the local coordinate system via Eq. (14), and finally transforming this subvector back to the global finite element coordinates. The interpolated values of the stream function are needed, in particular, to plot the streamlines. A rectangular grid is used for contour plotting.

CHAPTER 6

Pressure Field

In our approach, based on the stream function only, the dimensionless pressure field can be calculated when all the nodal variables in the global finite element coordinates have been found.

The pressure is governed by the Poisson equation obtained by taking the divergence of the momentum equations. By employing the continuity equation Eq. (2) the simplified expression for pressure is obtained in the form:

$$\nabla^2 p = -2(u_y v_x - u_x v_y) = 2(\psi_{xx}\psi_{yy} - \psi_{xy}^2) = f. \tag{71}$$

The equivalent variational principle for the above equation can be stated as:

$$\Pi = \iint_{\Omega} \left(\frac{1}{2}(\nabla p)^2 + \bar{f}p\right) d\Omega - \oint_{\Gamma} \frac{\partial \bar{p}}{\partial n} p d\Gamma \tag{72}$$

where $\frac{\partial p}{\partial n}$ is calculated from the momentum equation Eq. (1) written for the n direction:

$$\frac{\partial p}{\partial n} = -\frac{1}{Re}(\psi_{snn} + \psi_{sss}) + (\psi_n \psi_{ss} - \psi_s \psi_{sn}). \tag{73}$$

The functional on the element level in the local coordinates, (Fig. 1), is defined by the following expression:

$$\Pi^e = \iint_{\Omega^e} \left(\frac{1}{2}(p_\xi^2 + p_\eta^2) + \bar{f}p\right) d\xi d\eta + \int_b^a \frac{\partial \bar{p}}{\partial \eta} p \Big|_{\eta=0} d\xi. \tag{74}$$

We adopt the same finite element mesh for pressure as we have used for stream function, hence the source function f can be expressed, via Eq. (14), as:

$$f = 2 \sum_{r}^{20} \sum_{s}^{20} a_r a_s m_r (m_r - 1) n_s (n_s - 1) - m_r m_s n_r n_s] \xi^{m_r+m_s-2} \eta^{n_r+n_s-2} . \tag{75}$$

The pressure gradient along the boundary edge 1-2 is given by:

$$p_{\eta}\Big|_{\eta=0} = [- \frac{1}{Re} (\psi_{\xi\xi\xi} + \psi_{\xi\eta\eta}) + (\psi_{\eta}\psi_{\xi\xi} - \psi_{\xi}\psi_{\xi\eta})_{\eta=0}] . \tag{76}$$

It should be noted, that as the functional Eq. (73) contains derivatives of p up to the first order, it would have been sufficient to use any element of C^0 class. Here in order to conform with the solution the same truncated quintic polynomial is used for interpolation of pressure within the element, that is:

$$p = \sum_{i=1}^{20} b_i \xi^{m_i} \eta^{n_i} . \tag{77}$$

By repeating the steps equivalent to those, indicated in Eqs. (15), (16), (17), and (18), substituting then Eqs. (75), (76), and (77) into the functional Eq. (74), carrying out the integrations and transforming to global finite element coordinates, the discretized functional on the element level is obtained in the form:

$$\Pi^e = \frac{1}{2} \underline{P}^T \underline{\underline{K}} \underline{P} + (\underline{\bar{G}} + \underline{\bar{F}}) \underline{P} \tag{78}$$

where $\bar{\underline{\underline{K}}}$ is the element matrix, $\bar{\underline{G}}$ is the load vector of 'body' load terms, and $\bar{\underline{F}}$ is the load vector of 'surface' load terms.

By forming the global problem in the usual manner the following system of equations is obtained:

$$\underline{\underline{K}}\underline{P} + \underline{F} = 0 \tag{79}$$

where $\underline{\underline{K}}$ is symmetric and positive definite matrix, and $\underline{P}$ is the solution vector.

We note, that the functional Eq. (72) yields the Poisson equation Eq. (71) as Euler equation, and the boundary conditions of

$$\text{either} \quad \frac{\partial p}{\partial n} = \frac{\partial \bar{p}}{\partial n} \quad \text{or} \quad \delta p = 0. \tag{80}$$

Since the pressure gradient is known everywhere, via Eq. (73), all the boundary conditions are of the Neumann type. That makes the solution of Eq. (79) nonunique, however, because the system matrix $\underline{\underline{K}}$ is singular. To avoid this difficulty we have to impose a Dirichlet boundary condition at an arbitrary node.

For more details, concerning the calculation of pressure field it is referred to Tuann and Olson [5,6].

CHAPTER 7

Numerical Implementation

All our programs are written in Fortran in double precision arithmetic. We employ the dynamic storage option, so that we can control the size of all the arrays at execution time, rather than at compilation time. Thus we are able to run problems of various sizes without wasting any of the virtual memory and we can accomodate in core a much bigger transformed nonlinear matrix $\bar{\underline{\underline{Q}}}$.

As we have already mentioned previously we need to compute all the modes of the general linear eigenvalue problem Eq. (38) in an efficient manner. For this purpose we use the very fast direct eigenvalue solver contained in the program DRSGAL. The eigenvalue problem is solved as follows. Firstly, as the global consistent mass matrix is positive definite, its inverse can be found by LU decomposition. The global linear dissipative matrix $\underline{\underline{K}}$ is premultiplied by this inverse to transform the general eigenvalue problem to the simpler form

$$\bar{\underline{\underline{K}}}\ \underline{\psi} = \lambda\ \underline{\psi} \tag{81}$$

The symmetric matrix $\bar{\underline{\underline{K}}}$, of the order N, is reduced to a symmetric tridiagonal matrix, after N-2 orthogonal similarity transformations, using the Householder method. The eigenvalues and the eigenvectors of the tridiagonal matrix are found by QL transformations, and transformed back to the eigenvectors of $\bar{\underline{\underline{K}}}$. The CPU time, in seconds, for the eigenvalue analysis, is about $1.8 \times 10^{-5} \times N^3$, where N is the size of 'net' problem.

Then we solve the linear steady equivalent of Eq. (51) in order to determine which modes give a reasonable representation of the solution of the linear

problem with the convective terms taken equal to zero. This is conveniently done by a direct solver which is based on Gaussian elimination. The CPU time for this procedure, in seconds, is approximately 5.2×10^{-6} $(NT)^3$, where NT is equal to the number of the eigenvectors used plus the number of constraints of the problem. We note, that it is particularly important to perform this procedure in the square cavity flow problem, where, as it turns out, some higher modes must be included in order to approximate even the solution of the linear problem. The flow around a circular cylinder, on the other hand, due to the less stringent boundary conditions, behaves much like the problems encountered in structural dynamics, that is, the higher modes need not be included.

After having established which modes we are going to use as the new basis, we proceed to set up the complete nonlinear problem in the finite element coordinates. ThewCPU time for setting up the matrices is about 2.6 seconds per each new group of elements, where a group consists of elements, which have the same dimensions and the same orientation in space. We note, that for the square cavity flow and the flow around a circular cylinder problems we choose the origin of the global coordinate system, so that there exists one axis of symmetry. Consequently, the modes are either symmetric or antisymmetric, which results in some special properties of the transformed nonlinear convective matrix $Q_{lmn} = Q_{ijk}E_{il}E_{jm}E_{kn}$. Namely, if all three of the modes l, m, and n are symmetric, or if any two of them are antisymmetric and the third is symmetric, the corresponding entry in the transformed matrix Q is zero, otherwise it is nonzero. Consequently, only the multiplications in the transformation, which result in the nonzero entries, are performed increasing the efficiency of the transformation procedure. The CPU time, in seconds, for the transformation, can be estimated by the formula

$7.0 \times 10^{-6} \times N \times [NE \times LB3 \times (LB3-1) + NE^2 \times LB3 + NE^2 \times (NE+1) / 2]$, where N is the 'net' size of the problem, NE is the number of the modes used in the transformation, and LB3 = 2 x LB - 1 is the bandwidth of the problem in the finite element coordinates. We note, that the dynamic storage option increased the number of modes, that can be used in the analysis, to 62. This limit of maximum 62 modes is imposed by the capacity of the virtual memory of the IBM 370/168 machine at UBC, that is, the maximum order of the transformed nonlinear matrix $\underline{\underline{\bar{Q}}}$ that can be kept in core if double precision arithmetic is used, even taking account of the symmetry in the first two indices, is 62. Otherwise, auxiliary storage locations have to be employed.

Having stored the global consistent mass matrix, the eigenvalues and the corresponding modes, and the transformed nonlinear matrix $\underline{\underline{\bar{Q}}}$ on tape, we have all the arrays indicated in Eq. (50) and can run both steady state and time dependent analyses. In both cases, due to the Lagrange multipliers technique, the system matrix is nonpositive definite, although it is non-singular. Accordingly, the Gaussian elimination with partial pivoting, and forward and backward substitution is used to solve the resulting set of linearized algebraic equations. The CPU time for one iteration of the Newton-Raphson process, in seconds, is about $4.0 \times 10^{-6} \times (NT)^3$. For the first time dependent algorithm, with the nonlinear term transposed to the right hand side, and evaluated at the preceding time step, the CPU time per time step, in seconds, is approximately $2.4 \times 10^{-6} \times (NT)^3$. The CPU time for the second time dependent algorithm, where the system matrix is updated at every time step, in seconds, is about $3.4 \times 10^{-6} \times (NT)^3$. As before, NT denotes the number of eigenvectors plus the number of constraints.

The scalar vorticity $\zeta = \nabla^2 \psi$ is obtained by the interpolation program,

which is used for plotting. After the stream function subvector has been obtained at all points of a specified regular interpolation mesh, the vorticity at each of those points is simply equal to the sum of the second derivatives of the stream function ψ_{xx} and ψ_{yy}. The mesh is, in general, nonuniform with variable spacings in x- and y- directions. The whole domain can be covered by the mesh, or just some regions of interest. The streamlines, the pressure field, and the vorticities are then plotted using the standard contour subroutines. We note, that while the stream function and the velocities are continuous, the vorticity is only piecewise continuous, which accounts for not so good vorticity plots, especially for crude finite element grids. The pressure field representation is excellent, however, because the method for calculating pressures has a tendency of 'smearing out'.

CHAPTER 8

Example Applications

The foregoing modal finite element method has been used to solve several example flow problems. Our criterion in choosing example problems has been availability of known results, so that ready checks would be provided.

Numerical results for fully developed plane Poiseuille flow, circulatory flow in a square cavity and the flow around a circular cylinder problems, obtained by modal finite element method, are presented in this chapter. The results for Poiseuille flow problem are compared with the exact closed form solution. The steady state results for circulatory flow in a square cavity and the flow around a circular cylinder problems are compared to the results obtained by direct finite element approach using the same finite element grid and to the results obtained by various finite difference techniques, considered exact herein, as no closed form solutions exist for these problems.

8.1 Fully Developed Plane Poiseuille Flow

The first example chosen was that of a fully developed flow between parallel walls. The exact solution for this problem shows the flow laminar and distributed parabolically between the walls, with a corresponding linear pressure field decreasing downstream. The finite element grid used for this problem is shown in Fig. (3). The following boundary conditions were used, all of them kinematic in the sense of the restricted variational principle: (a) on the stream function ; $\psi = \psi(y) = 3y^2 - 2y^3$ on the upstream section, $\psi = 1$ on the upper wall, and $\psi = 0$ on the lower wall ; (b) on its normal derivative ; $\psi_x = - v = 0$ on the upstream and the downstream sections, and $\psi_y = u = 0$ on the upper and the lower wall. On the downstream section the

natural boundary conditions of zero pressure gradient across the flow $p_y = 0$ were to be approximated. The 'net' size of the problem was 12 with 4 constraints ; $\psi = 1$ at nodes 2 and 5, $\psi_{yy} = 6$ at node 1, and $\psi_{yy} = -6$ at node 2. We note, that because the finite element used contains a complete cubic for velocity interpolation, it was capable of exactly representing the parabolic velocity profile and the downstream natural boundary conditions of constant pressure.

The 12 mode shapes from the linear eigenvalue analysis are shown in Fig. (4), along with the corresponding eigenvalues for Re = 1. The curves represent equal steps in stream function values.

These modes were then used to represent the nonlinear equations indicated in Eq. (50). Both steady state and transient analyses were then performed using 5,6,7,8,9,10,11, and 12 modes, respectively. We note, that the lowest number 5 actually gave only one free mode, because of the 4 constraints imposed on the problem. The calculations were started with all free nodal variables equal to zero in both the analyses.

The Newton-Raphson steady state procedure converged in 3 or less iterations in all cases.

This simple problem was also used to check the efficiency of the three time integration algorithms. In the first and the third algorithms we used the time step of $\Delta t = 2/\lambda_{max}$, where λ_{max} was the eigenvalue associated with the highest mode kept in the analysis. In the second algorithm, due to its greater numerical stability, we could use a bigger time step, so we arbitrarily chose $\Delta t = 0.15$ seconds.

The first algorithm, with the nonlinear term transposed to the right hand side and evaluated at the previous time step, converged to the steady state in maximum 67 increments, when all 12 modes were used. We assumed that the steady state was achieved, when the maximum absolute difference in

the two entries corresponding to the same coordinate did not exceed $\varepsilon = 10^{-8}$.

In the second algorithm the steady state solution was attained in 7 increments, with ε of Eq. (62) prescribed as 10^{-7}.

When the exact solution was used as the initial guess the third algorithm was able to reproduce this result in 3 steps. When all the free nodal variables were zeroed, however, the algorithm did not converge.

On the basis of these calculations we decided to employ only the first two algorithms in this work, although the third one might have converged, as well, had the initial conditions been closer to the true solution.

The resulting streamlines and the predicted maximum velocities in the direction of the flow at the midnode 3 for 5,6,7,9, and 12 modes, respectively, are shown in Fig. (5). We see, that although the 5 mode result is rather poor, the 6 mode one is already quite acceptable, and compares very well with the exact result. As a matter of fact, as long as at least first 9 modes are used the exact result is obtained and only the generalized coordinates associated with modes 1,6, and 9 are finite, so that just these modes contribute to the solution. The exact solution is namely antisymmetric in stream function with respect to the axis z of Fig. (3), so that none of the symmetric modes can affect it. Taking that into account we reproduced the exact solution with just 5 modes, but we had to include modes 1,6, and 9, which possess the antisymmetric properties, while the remaining 2 modes were arbitrary. The generalized coordinate associated with mode 1 is always predominant. All results are independent of the Reynolds number.

8.2 Circulatory Flow in a Square Cavity

As the second problem we chose the flow within a square cavity which is bounded by three fixed walls and an upper lid moving with constant

velocity in its own plane, shown in Fig. (6).

Mathematical singularities are present in the problem in the regions of the upper vertices, 2 and 4, where a fixed wall meets a moving lid, due to the flow having to move without slip at the speed of the moving lid and yet be zero at the fixed wall. To avoid this difficulty two extra nodes were introduced close to the upper vertices, thus allowing for transition from zero normal velocity at the fixed walls to the prescribed tangential velocity of the moving lid at these new nodes. Two additional nodes were needed in the neighbourhood of the upper vertices on the fixed walls, as well, because of existing asymmetric pressure singularities.

All boundary conditions imposed on the problem were 'rigid' in the sense of the restricted variational principle. Accordingly, the only free nodal variable along the fixed walls 1-2 and 3-4 was ψ_{xx}, along the bottom fixed wall 1-3 ψ_{yy}, while on the upper lid ψ_y and ψ_{yy} were the only free nodal variables, so that the three fixed walls and the moving lid actually were zero streamlines.

The size of the cavity was assumed to be unity, and the given velocity of the moving lid was also taken to be unity in the direction to the left. Thus, the Reynolds number was naturally defined as $\mathrm{Re} = \frac{1}{\nu}$.

The three finite element grids used are shown in Fig. (7) together with the number of elements (NE), the number of nodes (NO), the size of the 'net' problem (NN), and the half bandwidth in the finite element coordinates (LB). The number of constraints for all three grids was equal to 1, because by using the 'master-slave' option we forced all the tangential velocity degrees of freedom ψ_y on the upper lid to be the same, thereby leaving only free variables.

All 15 mode shapes with associated eigenvalues for SQCA 12-13 grid

and the first 30 modes for SQCA 36-29 grid are shown in Fig. (8), arranged in the order of the ascending eigenvalues. We note, that the shape of the highest modes of the SQCA 12-13 grid is already influenced by the finite element layout. The most noteworthy feature, valid for all grids, is the strking increase in complexity of the modes with only one order of magnitude increase in the corresponding eigenvalues. The lowest and the highest eigenvalue for all three grids, together with the number of symmetric and antisymmetric modes and the total number of modes are given in Table (I). The interval bounded by the lowest and the highest eigenvalue of the finer grids also includes all the eigenvalues of the cruder grids, which serves as a check on the eigenvalue solver. The lowest eigenvalue only changes slightly from grid to grid, which seems to suggest that it is predicted accurately enough even for the very crude SQCA 12-13 grid. The corresponding modes are also almost identical. The modes are subdivided into the symmetric and the antisymmetric ones with respect to the vertical y axis. Only the symmetric modes are directly loaded by the velocity constraint on the moving lid, while the antisymmetric modes are excited only through nonlinear coupling. It is then obvious that the antisymmetric modes do not contribute to the linear solution for Re = 10^{-4}, while without these modes no nonlinear behaviour can be simulated.

When the modal approach was tried on this problem, we found that reasonable results could only be obtained if some of the higher modes were included in the analysis. This was true even for the linear problem with Re = 0, so we included all the symmetric modes, whose generalized coordinates were greater than some prescribed small value ε for Re = 0 decomposition. The antisymmetric modes used corresponded to the lowest eigenvalues.

On the SQCA 12-13 grid we used 15 and 11 modes, on the SQCA 36-29 grid 36 and 42 modes, and on the SQCA 26-53 grid 60 modes, respectively. Only the Newton-Raphson steady state procedure was run. The calculations were started with the Reynolds number $Re = 10^{-4}$ using the null solution, with all free variables equal to zero, as an initial guess in the finite element coordinates. The transformation to the eigenvector basis using the orthonormal properties of the eigenvectors had obviously to be performed before the iterations were started to yield an initial guess in the generalized coordinates. After the solution in the eigenvector basis had been obtained the transformation back to the finite element coordinates was performed via Eq. (35) to yield the stream function solution. This solution was then used as an initial guess for the next higher Reynolds number and the process repeated. These steps were carried out at $Re = 10^{-4}$, 1, 10, 20, 40, 100, 200 and 400 for all three grids. For SQCA 76-53 grid the rangee of Reynolds numbers was extended to Re = 3000 with the additional steps carried out at Re = 600, 1000, 1400, 1700, 2000, 2200, 2400, 2800 and 3000. The accuracy test on the Jacobian ε of Eq. (70) was set equal to 10^{-6}. Regardless of the grid and the number of modes used, that is the problem size, convergent solutions for the whole range of Reynolds numbers under consideration were obtained in 3 to 6 iterations. We note that this held true even for Reynolds numbers up to 3000, so it is concluded that numerical stability of modal method is quite high.

When the Poisson equation, Eq. (79), was solved to obtain the pressure field, the Dirichlet boundary condition p = 0 was imposed at the node located in the middle of the bottom wall. This effectively means that the pressure distribution is referenced to the pressure at the middle of the bottom wall. All the other pressure nodal variables were left free,

and accordingly, for all triangular finite elements with two of the vertices located on any part of the boundary, the boundary integral of Eq. (74) had to be included in the element functional expression to conform with the variational principle.

Error in stream function at midnode 5 of the SQCA 12-13 grid for various combinations of modes is listed in Table (II). We note that just one antisymmetric mode is enough to produce results with maximum 1% error for Reynolds numbers up to about 40, when compared to the direct finite element solution on the same grid.

Complete results for Reynolds numbers Re = 0, 10, 20, 40, 100, 200 and 400 are plotted in Figs. (9) - (11). The total number of modes and the number of symmetric and antisymmetric modes, together with predicted coordinates of the vortex centre and predicted values of stream function vorticity and pressure at the vortex centre are listed in Table (III). These results are compared with the direct finite element results on the same grids and with the Burggrâf's finite differences results [12]. Some small discrepancies between the direct finite element results reported here and the ones of [5] are due to the different interpolation grids used. Namely, we used crude 20x20 interpolation grid in this work, while [5] employed more accurate irregular interpolation grid. Only the general shape of streamlines from modal method and direct finite element approach can be compared with Burggrâf's results, because contour levels do not match. The vorticities and the pressures can be compared directly, however.

The SQCA 12-13 grid is too crude to produce accurate results even for low Reynolds numbers and if the direct finite element approach is used. This is especially true for the vorticity predictions, but also, for the stream function and the pressure predictions, which are in general too high.

The 11 modes results with just 1 antisymmetric mode do agree quite well with the 15 modes results and the direct finite element approach results on the same grid, which are of course identical, up to Re of about 40. For higher Re the agreement rapidly deteriorates. In the 15 modes results the change of position of the vortex centre with increasing Re is followed to some extent, while 11 modes results show the vortex centre stationary for the whole range of Re under consideration.

In the 60 modes results on the SQCA 76-53 grid the lower right secondary vortex, which appears in the exact solution, does show at Re = 40, then increases gradually at Re = 100 and 200, but disappears at Re = 400. For all these Reynolds numbers the seconary vortex is shifted a little to the left. The stronger lower left vortex of the exact solution does not show at all. The vorticity contours are somewhat wavy in appearance, especially in the region close the bottom wall, but the general trend seems to be preserved. The pressure contours agree quite well with the exact results except for the region close to the bottom wall. The position of the vortex centre is predicted very well for the whole range of Reynolds numbers under consideration. The same is true for the stream function and the pressure values at the vortex centre. The vorticity value at the vortex centre agrees well with the exact result for Re up to about 20, while for higher Re the predicted vorticity values are much too high.

B Best modal results are achieved with 36 modes and 42 modes on the SQCA 36-29 grid. Both the 36 modes and the 42 modes results appear to reproduce the streamlines predicted by the direct finite element approach on the same grid very well for the whole range of Reynolds numbers considered, especially near the upper lid where the gradients are high. They also compare reasonably well with Burggraf's results, considered exact herein, reproducing the lower right

secondary vortex, but not the stronger lower left secondary vortex. The vorticity predictions also compare satisfactorily with the direct finite element approach results and even Burggraf's results, considered exact again, for the whole range of Reynolds numbers under consideration. The 42 modes results are slightly better than the 36 modes ones as could have been expected for both the stream function and the vorticity. The pressure results are in excellent agreement with the results obtained for the full SQCA 36-29 grid and even with the full SQCA 76-53 grid results, considered exact herein, up to Re of about 100. For higher Re the agreement is still fair, especially between modal results and the direct finite element approach on the same grid with the 42 modes results again having a slight edge over 36 modes results.

From all these results we conclude that good agreement with the 'exact' solution of the discretized problem, obtained by direct finite element approach, for this range of Reynolds numbers, can be achieved by employing about 50% of the modes, that is, the number of modes, which are required, goes up with the refinement of the finite element mesh. That explains why 36 modes and 42 modes on the cruder SQCA 36-29 grid yield better results than 60 modes on the finer SQCA 76-53 grid, which contains much more degrees of freedom.

8.3 Flow Around a Circular Cylinder

The final example considered was the classical problem of the flow around a circular cylinder.

Physically the problem involves an infinitely long cylinder immersed in a fluid medium of infinite extent. We adopted finite domains, however, as it is usually done in computational fluid dynamics involving exterior flow.

The first domain was used for numerical simulation of the steady flow, while the second domain, obtained by extending the first domain for six units downstream, was used for the transient flow simulation. Both domains are shown in Fig. (12), together with the adopted finite element grids, the number of elements (NE), the number of nodes (NO) and the central angle (ΔQ). The centre of the cylinder is located at the origin of the (x,y) plane for both domains. The boundary is divided into the inflow section Γ_i, the outflow section Γ_o, the cylinder wall Γ_w and the top and the bottom sections Γ_u parallel to the incident uniform stream flow of unit velocity along the positive x-axis.

The boundary conditions at the inflow section Γ_i were all 'rigid', obtained by specifying the uniform stream flow defined by u=1 and $v=\hat{0}$. The stream function nodal variables, as the direct result of these 'rigid' boundary conditions, were given as $\psi=y$, $\psi_x=0$, $\psi_y=1$, $\psi_{xy}=0$, and $\psi_{yy}=0$, while ψ_{xx} was left free. On the outflow section Γ_o the 'rigid' boundary condition v=o was used to pair up with the 'natural' boundary condition of constant pressure $\bar{p}_y=0$ in the steady case. These conditions allowed the u=- velocity to develop on this section. The $v=-\psi_x=0$ 'rigid' boundary condition implied that $\psi_{xy}=0$, which in turn indicated that ψ_y was to be unknown. The 'natural' boundary condition $\bar{p}_y=0$ required that ψ and ψ_{yy} were to be unknown. Accordingly, on this section the boundary conditions in terms of nodal stream function variables were given as $\psi_x=0$ and $\psi_{xy}=0$ with ψ, ψ_y, ψ_{xx} and ψ_{yy} left free. The 'rigid' boundary conditions of no-slip $\psi_n=0$ and $\psi_s=0$ were directly imposed at each of the nodes located on the cylinder wall Γ_w. The $\psi_s=0$ condition implied that $\psi_{ns}=0$ and $\psi_{ss}=0$ on Γ_w, and also that ψ was a constant, which was set equal to zero. Accordingly, at any node on Γ_w of the six nodal variables in the local (s,n) system, which was used in place of the global (x,y) system, only ψ_{nn} was retained while all others were zeroed and eliminated. This had the effect

of satisfying the no-slip conditions exactly only at discrete nodes on the cylinder wall, unlike the straight boundaries, where the prescribed boundary conditions can be realized pointwise. On the top and the bottom sections Γ_u the 'rigid' boundary condition of u=1 was set to pair up with the 'natural' boundary condition of constant pressure $p_x=0$ for the steady state analysis. These conditions allowed the v- component to develop along Γ_u. The $u=\psi_y=1$ 'rigid' boundary condition implied that $\psi_{xy}=0$ which required ψ_x to be unknown. The 'natural' boundary condition $p_y=0$ indicated that ψ and ψ_{xx} had to be unknown. Consequently, the boundary conditions in terms of nodal stream function variables were given as $\psi_y=1$ and $\psi_{xy}=0$ with ψ, ψ_x, ψ_{xx} and ψ_{yy} left free.

Alternatively, for the steady flow the assumption can be made that the flow is symmetric with respect to the x-axis and so only flow in the upper half domain $y \geq 0$ need be considered. The symmetry of the flow implies that u is an even function of y and v is an odd function of y, so that both v_y and v_x are odd and vanish on the x-axis. It follows that both ψ and ζ are odd and therefore also vanish on y=0. So the 'rigid' boundary condition $\psi=0$ is imposed on the x-axis, which has become the part of the boundary, to pair up with the 'natural' boundary condition of zero shear stress or $\zeta=0$. The 'natural' boundary condition requires that $\psi_{xx}=0$ and $\psi_{yy}=0$, the latter of which in turn implies that ψ_y is unknown. Hence ψ_{xy} is also unknown, and the boundary conditions in terms of nodal stream function variables are given as $\psi=0$, $\psi_x=0$, $\psi_{xx}=0$ and $\psi_{yy}=0$, with ψ_y and ψ_{xy} left free. We note that the 'natural' boundary condition $\zeta=0$ holds only at the nodes on x-axis.

The transient analysis requires the full domain to be represented, since the symmetry has vanished. The same boundary conditions were imposed on the inflow boundary Γ_i and the cylinder wall Γ_w as in the steady case.

The top and the bottom sections Γ_u were assumed to be zero friction smooth walls and so the 'rigid' boundary conditions $\psi=y$ and $v=\psi_y=1$ were imposed there. The nodal stream function variables on Γ_u, as the direct result of these 'rigid' boundary conditions, were given as $\psi=y$, $\psi_x=0$, $\psi_y=1$, $\psi_{xx}=0$ and $\psi_{xy}=0$, while ψ_{yy} was left free. On the outflow section Γ_o we needed the flow to be as unconstrained as possible, so that the 'rigid' boundary condition $v=0$ was definitely out of question. The best that we could do was to leave all nodal stream function variables on Γ_o free, thus in lieu of the governing restricted variational principle effectively specifying the 'natural' boundary conditions of zero shear stress $\tau=0$ and constant pressure $p_y=0$. We note, that even these less stringent boundary conditions are erroneous. That is why we extended the computational domain for six units downstream thus hoping to reduce the influence of the outflow boundary conditions on the region of special interest behind the obstacle, where unsteady behaviour was expected at a certain value of Reynolds number.

When the eigenvalue problem was solved the ψ_y along the boundaries Γ_i and Γ_u were constrained to be equal by using the 'master-slave' option. For the CYLFL 92-63 grid the stream function ψ was also constrained to be equal along the boundary Γ_u using the same option. The number of unknowns for the CYLFL 84-58 grid was 223 and for the CYLFL 92-63 grid 226. The first 15 mode shapes, antisymmetric in stream function, with the associated eigenvalues, are shown in Fig. (13-1) for the CYLFL 84-58 grid. The first 20 mode shapes, antisymmetric in stream function with the associated eigenvalues, and the first 10 mode shapes, symmetric in stream function, with the associated eigenvalues, are shown in Fig. (13-2). The contour levels represent equal steps in stream function and are plotted for the upper half domain $y \geq 0$ to save space. The net for plotting was 26 x 48 for the CYLFL 84-58 grid and

26 x 54 for the CYLFL 92-63 grid, with x- and y- spacings varying from 0.4 to 1.0, increasing outwardly from the centre of the cylinder, for both grids. We observe that the eigenvalues increase quite rapidly with mode number compared to the square cavity flow problem.

When modal approach was tried on the CYLFL 84-58 grid for the steady flow we observed that no higher modes were needed in order to attain reasonable results. We also observed that the generalized coordinates associated with the symmetric modes were all practically zero for the whole range of Reynolds numbers considered, confirming that, as expected, the symmetric modes could not contribute to the solution which was antisymmetric in stream function. Hence, in all subsequent calculations reported herein, we used the upper half domain $y \geq 0$ of Fig. (13-1) only, applying on the boundary defined by the x-axis the boundary conditions as covered previously. The discrete problem, thus obtained, had 104 degrees of freedom in the finite element coordinates, while the bandwidth was 48. The number of elements was 42 and the number of nodes 34. 62 modes were used in the modal representation, all of them evidently antisymmetric in stream function. The number of constraints in the problem was 3, ψ=3.0 and ψ=20.0 at the two nodes on the Γ_i boundary obtained from the boundary condition ψ=y there, and ψ_y=1 at all nodes located on the Γ_i and Γ_u boundaries. The calculations were started with Re = 1 using the null solution with all variables, except for the constrained ones, zeroed as an initial guess in the finite element coordinates. This initial guess vector was then transformed to the eigenvector basis to yield an initial guess vector in the generalized coordinates. After the solution in terms of generalized coordinates had been obtained by Newton-Raphson iterative procedure, it was transformed back to the finite element coordinates via Eg.(35) to yield the stream function solution. This solution was then used

as an initial guess for next higher Re, and the process repeated. These steps were carried out at Re = 1,5,7,10,20,40,70 and 100. Maximum 5 iterations were needed to attain an accuracy of $\varepsilon=10^{-6}$ in the whole range of Reynolds numbers considered. No oscillatory solutions or instabilities were encountered.

The pressure field was computed only for the steady flow. The upper half domain $y \geq 0$ only was considered. When the Poisson equation (79), was solved for pressure, all the boundary conditions were of the Neumann type, as already mentioned previously in Chapter (6). Tuann and Olson [6] found, however, that the predicted pressure on the far boundaries Γ_i, Γ_u and Γ_o was very nearly zero, as it should have been according to boundary conditions imposed on the stream function ψ. As all our boundary conditions on the stream function ψ are the same as those of [6], for the steady flow, we forced p to be identically zero on these boundaries. The symmetry condition $p_y=0$ was also enforced all along the x-axis. The dimensionless total drag coefficient C_D was obtained as the sum of the friction drag coefficient C_f calculated as $C_f = \frac{2}{Re}\int_0^{\pi}\psi_{nn}\Big|_{n=0}\sin\theta d\theta$, and the pressure drag coefficient C_p, given by the expression $C_p = -\int_0^{\pi} p\cos\theta d\theta$. These line integrals were only approximated, however, because the integrations were not performed along the cylinder, but along the polygonal segments of the finite element grid approximating the cylinder. The number of unknowns in the discrete problem was 155, the bandwidth 50, while the number of elements and the number of nodes were 42 and 34, respectively, that is the same as for the stream function calculations.

Complete stream function and vorticity results for steady flow for Reynolds numbers Re = 1,5,7,10,20,40,70 and 100 are plotted in Figs. (14) and (15), respectively. Only the region of interest is shown extending from 3 units upstream to 9 units downstream in the x direction measured from the centre of the cylinder, and for 3 units in the direction of the positive

y-axis measured from the x-axis. The interpolation net was 25 x 66 with the x-spacings varying from 0.1 to 0.4, and the y-spacings from 0.1 to 0.2, both increasing outwardly from the centre of the cylinder. The net functions, ψ and ζ, at the interior points of the cylinder were set to zero. The contour levels were specified to match those reported by Tuann and Olson [6], so that direct comparison would be possible. These modal results are compared with the direct finite element results on the same grid [6] and the finite difference results by Dennis and Chang [13] or Takami and Keller [14,15].

The agreement between modal stream function results and stream function results by the direct finite element method on the same grid is excellent up to Re of about 40, although the first appearance of a negative valued stream function becomes visible at Re = 10, whereas it is observable at Re = 7 in the direct finite element results. At Re = 70 the zero streamline does not extend far enough downstream and this trend gets even more pronounced at Re = 100 resulting in the wake being too short. The agreement between modal and finite differences results is excellent up to Re of about 20. For higher Re the length of the wakes and the positions of the vortex centre predicted by modal method do not match those predicted by finite differences. This discrepancy increases with Re, so that while modal results for Re = 40 are still acceptable, the predicted wakes at Re = 70 and 100 are much too short.

Modal vorticity predictions agree quite well with the direct finite element approach predictions again up to Re of about 40. The agreement deteriorates with increasing Re, though, and while for higher Re in this range modal values in the regions of most interest behind and immediately above the cylinder are very close to finite element values, in the region in front and farther above the cylinder modal method predicts values which

do not seem to exist in direct finite element results. At Re = 70 and 100 the predicted values in these regions get even worse, but, while the values in the regions of most interest behind and close above the cylinder are not very close to those predicted by direct finite element approach, the general trend of equi-vorticity lines is still reproduced. Equi-vorticity lines predicted by modal method agree with the finite differences results up to Re = 20 in the regions of most interest. For higher Re modal results are somewhat wavy and some equi-vorticity lines have kinks showing the influence of the grid. Again the discrepancies, as expected, increase with increasing Re.

Equi-pressure lines were not plotted because no comparisons were available. The friction drag coefficient C_f, the pressure drag coefficient C_p, the total drag coefficient C_D and the pressure values at the leading edge and the trailing edge of the cylinder are listed in Table (IV), however, and compared to the direct finite element approach results [6] and the finite differences results [13,14]. All these results are consistently lower than the direct finite element results on the same grid for the whole range of Reynolds numbers under consideration. The difference is drag coefficients, C_f, C_p and C_D, increases with increasing Reynolds numbers with the maximum difference of about 30% at Re = 100. The difference in the pressure value at the leading edge of the cylinder is consistently much higher than the difference in the pressure value at the trailing edge. Modal results are not consistently higher than the finite differences results, considered exact herein, as the direct finite element results are. Amazingly enough, though, all modal results for Re up to 40 are closer to the finite differences results than the direct finite element approach results on the same grid. This can only be explained by reasoning that some approximation errors

introduced in the pressure calculations by finite element discretization were cancelled by further approximation errors introduced by modal analysis.

From these results we conclude that good agreement with the direct finite element approach results for the steady case can be achieved by modal method for Reynolds numbers up to about 70 by employing about 50% of the modes. The agreement between modal results and the 'exact' results obtained by finite differences is good for Reynolds numbers only up to about 40, as it is also a function of finite element discretization.

For the transient analysis on the CYLFL 92-63 grid 62 modes were employed. First 52 modes, antisymmetric in stream function, and first 10 modes symmetric in stream function. The transformation of the nonlinear convective $\underline{\underline{Q}}$ matrix to the eigenvector basis, spanned by these modes, would have been very expensive for the full grid. We succeeded, however, to reduce the CPU time needed for the transformation 3.5 times by making use of the special properties of the transformed nonlinear convective $\underline{\underline{\bar{Q}}}$ matrix, covered in Chapter (7). It was done as follows. Firstly, the $\underline{\underline{Q}}$ matrix was formed for the upper half of the CYLFL 92-63 grid. All boundary conditions imposed on the Γ_i, Γ_o, Γ_u and Γ_w boundaries were the same as for the full grid, while all nodal variables at the nodes located on the x-axis, which became a boundary, were left free. The number of degrees of freedom for this grid was 139 and the bandwidth was 48, while for the full grid they would have been 226 and 78, respectively. Then the modes of the full grid were truncated, so that only entries corresponding to the degrees of freedom of the half grid were retained and the transformation performed using these truncated modes. By multiplying all entries of the resulting array by a factor of 2.0, the transformed nonlinear convective matrix $\underline{\underline{\bar{Q}}}$ for the full grid was finally obtained. The mass matrix, needed in the time algorithms for transformation from finite element coordinates

to generalized coordinates and vice versa, was computed for the full grid. The constraints on the stream function, obtained from the boundary condition $\psi=y$ imposed on the Γ_i and Γ_u boundaries, were $\psi= 3.0$ and $\psi= -3.0$ at the two nodes located on the Γ_i boundary, $\psi= 20.0$ at all nodes located on the top Γ_u boundary and $\psi= -20.0$ at all nodes located on the bottom Γ_u boundary. In addition, the constraint $\psi_y=1$ was imposed at all nodes situated on both the Γ_i and Γ_u boundaries, so that the total number of constraints in the problem was 5.

The time integrations were started with an initial solution obtained by perturbing the steady state results for a particular Reynolds number under consideration. The constrained variables on the boundary were kept fixed throughout the time integrations which in effect amounted to specifying time independent boundary conditions.

The calculations at Re=20 were performed with two time integration algorithms, the first one defined by Eq. (56) and the second one by Eq. (57). From these trial calculations we found, that while both algorithms yielded the same results the second algorithm was more efficient, because a much larger time step could be used without endangering the numerical stability. So, in all subsequent calculations we exclusively used this algorithm. When the time analysis was performed at Re=20, 40 and 70 the steady state was reached in all three cases. We would have expected that to happen at Re=20 and 40, but not at Re=70, where the flow should have become unsteady with oscillations of the downstream part of the wake. We reasoned, that this was the result of finite element discretization errors and further truncation errors introduced by modal analysis, which employed only 10 modes, symmetric in stream function. These errors introduced an 'artificial viscosity' effect which lowered the 'effective' Reynolds number. This 'artificial

viscosity' was, we thought, the main cause of numerical over-stability of our discrete problem, Eq. (50), as compared to the actual hydrodynamic stability inherent in the governing partial differential equation, Eq. (5). So we decided to increase the Reynolds number, thus also hoping to increase the 'effective' Reynolds number, and to perform the time integrations at Re=140, although judging from the steady results reported in [6], the finite element grid was too crude at such a high Re. The integrations were performed with a time step $\Delta t=0.15$ seconds, while the test on whether the steady state had been achieved, Eq. (62), was set to be $\varepsilon=10^{-6}$. The initial solution was arbitrarily specified by perturbing the steady state stream function values at the nodes located in the upper half domain $y>0$ upstream in the neighbourhood of the cylinder by 10% and at the mirror images of these nodes located in the lower half domain $y<0$ by 15%. The stream function results at time T=3, 6, 9, 12, and 16.5 seconds are plotted in Fig. (16). These results seems to indicate expected oscillatory behaviour, but finally the steady state solution, antisymmetric in stream function, was obtained, anyway. We speculate that this happened primarily because of the wrong downstream boundary conditions whose influence was reflected to the computational domain forcing the flow back to steady state. Unfortunately, we could not come up with any better downstream boundary conditions and this is left for some future study. We also note that the extension of the domain downstream, indicated in Fig. (12-2) might not have been enough to reduce this boundary conditions effect on the region of interest. To summarize, it seems that the inability of our procedure to predict the expected unsteady flow was caused to some extent by truncation errors introduced by finite element discretization and additional modal truncation errors, but primarily by the boundary conditions specified on the downstream boundary Γ_o.

CHAPTER 9

Conclusions

A modal finite element method for the steady state and the transient analyses of the plane flow of incompressible Newtonian fluid has been presented. The governing restricted functional was discretized with a high precision triangular stream function finite element of C^1 class [3]. Eigenvalue analysis was carried out on the linear part of the problem obtained by deleting the nonlinear convective term. It was found that the Lagrange multipliers technique was computationally more efficient for incorporating the nonhomogeneous boundary conditions than the condensation procedure. In the latter procedure numerical difficulties were encountered when dealing with the nonlinear convective matrix. The matrix equations to be solved, when the Lagrange multipliers technique is applied, are nonsingular but indefinite. We found that this posed no computational difficulties as the Gaussian elimination with partial pivoting and forward and backward substitution could conveniently be used to solve such equations. The number of modes was restricted to 62 because of the computer core capacity and this limitation has to be further explored. We found that the computer time for the transformation of the nonlinear convective matrix to modal coordinates could be significantly reduced by taking advantage of the symmetric and antisymmetric properties of the modes. The transformation procedure was still quite expensive. Therefore, it is concluded that there will be some practical limit on the size of the problem that can be solved by modal method.

When modal method was applied to several flow problems we found that the number of modes, which were to be retained in the analysis in order to achieve reasonable results, increased with the refinement of the finite element grid. Furthermore, the choice of modes depended on the problem. In the square cavity flow problem some higher modes had to be included in order to approximate even the linear part, while for the flow around a circular cylinder no higher modes needed to be included.

In the steady state analysis the convergent solution was obtained in 6 or less iterations, for the whole range of Reynolds numbers considered, regardless of the grid and the number of modes used. That is, numerical instabilities frequently encountered in the finite difference method at higher Reynolds numbers were never experienced. It is concluded, that this new modal finite element method in general yields good results in the range of moderate Reynolds numbers with about 50% or less of the total modes.

When the time dependent analysis was applied to the flow around a circular cylinder it was concluded that the inability to predict unsteady behaviour, expected at higher Reynolds numbers, was primarily caused by the outflow boundary conditions. This lends hope that once these boundary conditions have been corrected or at least their influence reduced by extending the computational domain further downstream, it will be possible to perform the time integrations on a greatly reduced number of equations by employing modal analysis. Hence, significant savings in computer costs can be achieved. Finally, as good results have been obtained in this thesis for moderate Reynolds numbers employing a greatly reduced number of linear modes, we speculate, that the extension of modal method to higher Reynolds numbers is quite feasible. It could be achieved, as suggested by Nickel [10], by introducing modal decompositions for the subsequent nonlinear states based upon the tangent matrix.

BIBLIOGRAPHY

1. Olson, M.D., "Comparison of Various Finite Element Solution Methods for the Navier-Stokes Equations", Proceedings of International Conference on Finite Elements in Water Resources, Princeton University, Princeton, U.S.A., July 12-16, 1976.

2. Finlayson, B.A., The Method of Weighted Residuals and Variational Principles, Academic Press, New York, 1972.

3. Olson, M.D., "A Variational Finite Element Method for Two-Dimensional Steady Viscous Flows", Proceedings of McGill-Engineering Institute of Canada Conference on Finite Element Methods in Civil Engineering, McGill University, Montreal, June 1-2, 1972, pp. 518-618. Also in Finite Elements in Fluids - Volume 1, (Ed. Gallagher, R.H., Oden, J.T., Taylor, C., and Zienkiewicz, O.C.), John Wiley & Sons, New York, 1975.

4. Yamada, Y., Ito, K., Yokouchi, Y., Tamano, T. and Ohtsubo, T., "Finite Element Analysis of Steady Fluid and Metal Flow", Finite Elements in Fluids - Volume 1, (Ed. Gallagher, R.H., Oden, J.T., Taylor, C., and Zienkiewicz, O.C.), John Wiley & Sons, New York, 1975.

5. Tuann, S.Y., and Olson, M.D., "A Study of Various Finite Element Methods for the Navier-Stokes Equations", Structural Research Series, Report No. 14, Department of Civil Engineering, University of British Columbia, Vancouver, Canada, May 1976.

6. Tuann, S.Y., and Olson, M.D., "Numerical Studies of the Flow Around a Circular Cylinder by a Finite Element Method", Structural Research

Series, Report No. 16, Department of Civil Engineering, University of British Columbia, Vancouver, Canada, December 1976.

7. Cowper, G.R., Kosko, E., Lindberg, G.M., and Olson, M.D., "A High Precision Triangular Plate Bending Element," Aeronautical Report LR-514, National Research Council of Canada, Ottawa, 1968.

8. Gallagher, R.H., Finite Element Analysis, Prentice-Hall, Englewood Cliffs, New Jersey, 1975.

9. Clough, R.W., and Penzien, J., Dynamics of Structures, McGraw-Hill, 1975.

10. Nickel, R.E., "Nonlinear Dynamics by Mode Superposition", Computer Methods in Applied Mechanics and Engineering, 7 (1976), pp. 107-129, North-Holland.

11. Stricklin, J.A., Martinez, J.E., Tillerson, J.R., Hong, J.H., and Haisler, W.E., "Nonlinear Dynamic Analysis of Shells of Revolution by the Matrix Displacement Method", American Institute of Aeronautics and Astronautics Journal, 9 (4), pp. 629-636, April 1971.

12. Burggraf, O.R., "Analytical and Numerical Studies of the Structure of Steady Separated Flows", Journal of Fluid Mechanics, Vol. 24, Part 1, pp. 113-151, 1966.

13. Dennis, S.C.R., and Chang, G.Z., "Numerical Solutions for Steady Flow Past a Circular Cylinder at Reynolds Numbers Up to 100", Journal of Fluid Mechanics, Vol. 42, Part 3, pp. 471-489, 1970.

14. Takami, H., and Keller, H.B., "Steady Two-Dimensional Viscous Flow of an Incompressible Fluid Past a Circular Cylinder", Phys. Fluids Supplement II, Vol. 12, pp. 11-51, 1969.

15. Keller, H.B., and Takami, H., "Numerical Studies of Steady Viscous Flow Around Cylinders", Numerical Solutions of Nonlinear Differential Equations, (Ed. Greenspan D.), John Wiley & Sons, pp. 115-140, 1966.

Grid	Number of Modes			Eigenvalues					
				Symmetric		Antisymmetric		Total	
	Symm.	Antisymm.	Total	Lowest	Highest	Lowest	Highest	Lowest	Highest
SQCA 12-13	10	5	15	53.3062	12799.6	108.352	9516.34	53.3062	12799.6
SQCA 36-29	40	31	71	51.6295	45973.8	92.4626	44085.0	51.6295	45973.8
SQCA 76-53	94	81	175	50.7516	49398.6	92.1604	48683.4	50.7516	49398.6

TABLE I Number of Symmetric and Antisymmetric Modes and Lowest and Highest Eigenvalues for Three Finite Element Grids Used for Square Cavity Flow Problem Simulation

Number of Modes			Reynolds Number, R						
			1	10	20	40	100	200	400
Symm.	Antisymm.	Total	Error in % at Midnodes5						
10	5	15	0.	0.	0.	0.	0.	0.	0.
9	5	14	0.76	0.78	0.85	1.08	1.63	1.96	1.94
8	5	13	1.40	1.42	1.47	1.65	2.06	2.26	1.31
8	4	12	1.40	1.42	1.49	1.75	2.36	2.75	9.18
10	1	11	0.	0.	0.27	1.02	11.33	17.22	42.73

TABLE II Error in Stream Function at Midnode 5 for Various Number of Modes and Various Reynolds Numbers for SQCA 12-13 Grid

Method	Grid	Number of Modes			$x_{v.c.}$	$y_{v.c.}$	$\psi_{v.c.}$	$\zeta_{v.c.}$	$\dot{p}_{v.c.}$	Grid for Plotting
		Symm.	Antisymm.	Total						
Modal	SQCA 12-13	10	5	15	0.0	0.25	0.1355	5.5225	0.0	20 x 20
		10	1	11	0.0	0.25	0.1355	5.5225	0.0	
	SQCA 36-29	27	15	42	0.0	0.25	0.0989	2.8059	-0.0892	
		26	10	36	0.0	0.25	0.0984	1.8501	-0.0835	
	SQCA 76-53	39	21	60	0.0	0.25	0.1040	2.7424	-0.0003	
Direct Finite Element Approach	SQCA 12-13	-	-	-	0.0	0.25	0.1355	5.225	0.0	
	SQCA 36-29	-	-	-	0.0	0.25	0.0986	3.033	-0.0862	
	SQCA 76-53	-	-	-	0.0	0.25	0.0996	2.9775	-0.0928	
[12]	50 x 50	-	-	-	0.0	0.27	0.100	3.20	0.0	

R = 0

TABLE III Comparison of Numerical Results for Square Cavity Flow Problem

Method	Grid	Number of Modes			$x_{v.c.}$	$y_{v.c.}$	$\psi_{v.c.}$	$\zeta_{v.c.}$	$\bar{p}_{v.c.}$	Grid for Plotting
		Symm.	Antisymm.	Total						
Modal	SQCA 12-13	10	5	15	0.0	0.25	0.1355	5.5196	-2.3096	20 x 20
		10	1	11	0.0	0.25	0.1355	5.5207	-2.3092	
	SQCA 36-29	27	15	42	0.0	0.25	0.0988	2.8050	-0.8911	
		26	10	36	0.0	0.25	0.0984	1.8494	-0.8347	
	SQCA 76-53	39	21	60	0.0	0.25	0.1040	2.7276	-0.9828	
Direct Finite Element Approach	SQCA 12-13	-	-	-	0.0	0.25	0.1355	5.5196	-2.3096	
	SQCA 36-29	-	-	-	0.0	0.25	0.0985	3.0090	-0.8607	
	SQCA 76-53	-	-	-	0.0	0.25	0.0995	2.9657	-0.9270	

R = 10

TABLE III (cont.) Comparison of Numerical Results for Square Cavity Flow Problem

Method	Grid	Number of Modes			$x_{v.c.}$	$y_{v.c.}$	$\psi_{v.c.}$	$\zeta_{v.c.}$	$p_{v.c.}$	Grid for Plotting
		Symm.	Antisymm.	Total						
Modal	SQCA 12-13	10	5	15	0.0	0.25	0.1355	5.5107	-4.6126	20 x 20
		10	1	11	0.0	0.25	0.1354	5.5157	-4.6096	
	SQCA 36-29	27	15	42	-0.05	0.25	0.0987	2.2439	-1.2252	
		26	10	36	-0.05	0.25	0.0986	1.9595	-1.1424	
	SQCA 76-53	39	21	60	-0.05	0.25	0.1046	2.8044	-1.5328	
Direct Finite Element Approach	SQCA 12-13	-	-	-	0.0	0.25	0.1355	5.5107	-4.6126	
	SQCA 36-29	-	-	-	-0.05	0.25	0.0985	2.2887	-1.1057	
	SQCA 76-53	-	-	-	-0.05	0.25	0.0996	3.1068	-1.2662	

R = 20

TABLE III (cont.) Comparison of Numerical Results for Square Cavity Flow Problem

Method	Grid	Number of Modes			$x_{v.c.}$ $x_{v.c.}$	$y_{v.c.}$ $y_{v.c.}$	$\psi_{v.c.}$ $\psi_{v.c.}$	$\zeta_{v.c.}$ $\zeta_{v.c.}$	$p_{v.c.}$ $p_{v.c.}$	Grid for Plotting
		Symm.	Antisymm.	Total						
Modal	SQCA 12-13	10	5	15	0.0	0.25	0.1354	5.4729	-9.1711	20 x 20
		10	1	11	0.0	0.25	0.1350	5.4965	-9.1518	
	SQCA 36-29	27	15	42	-0.05	0.25	0.0995	2.2381	-3.1196	
		26	10	36	-0.05	0.25	0.0995	1.9080	-2.9461	
	SQCA 76-53	39	21	60	-0.10	0.25	0.1062	6.9153	-3.3526	
Direct Finite Element Approach	SQCA 12-13	-	-	-	0.0	0.25	0.1354	5.4729	-9.1711	
	SQCA 36-29	-	-	-	-0.05	0.25	0.0994	2.2729	-3.0044	
	SQCA 76-53	-	-	-	-0.05	0.25	0.1003	3.1277	-3.2471	

R = 40

TABLE III (cont.) Comparison of Numerical Results for Square Cavity Flow Problem

Method	Grid	Number of Modes			$x_{v.c.}$	$y_{v.c.}$	$\psi_{v.c.}$	$\zeta_{v.c.}$	$p_{v.c.}$	Grid for Plotting
		Symm.	Antisymm.	Total						
Modal	SQCA 12-13	10	5	15	0.0	0.20	0.1359	5.1545	-21.0284	20 x 20
		10	1	11	0.0	0.25	0.1331	5.4002	-22.022	
	SQCA 36-29	27	15	42	-0.10	0.20	0.1045	2.3892	-9.2827	
		26	10	36	-0.10	0.20	0.1061	2.4479	-9.4048	
	SQCA 76-53	39	21	60	-0.10	0.25	0.1127	7.1780	-12.3943	
Direct Finite Element Approach	SQCA 12-13	-	-	-	0.0	0.20	0.1359	5.1545	-21.0284	
	SQCA 36-29	-	-	-	-0.10	0.20	0.1054	3.0346	-9.8903	
	SQCA 76-53	-	-	-	-0.10	0.25	0.1037	2.8612	-9.7013	
[12]	50 x 50	-	-	-	-0.13	0.24	0.101	3.14	-18.1	

R = 100

TABLE III (cont.) Comparison of Numerical Results for Square Cavity Flow Problem

Method	Grid	Number of Modes			$x_{v.c.}$	$y_{v.c.}$	$\psi_{v.c.}$	$\zeta_{v.c.}$	$p_{v.c.}$	Grid for Plotting
		Symm.	Antisymm.	Total						
Modal	SQCA 12-13	10	5	15	0.0	0.20	0.1428	4.9600	-42.3894	20 x 20
		10	1	11	0.0	0.25	0.1307	5.2643	-41.5979	
	SQCA 36-29	27	15	42	-0.05	0.15	0.1152	2.7952	-25.2413	
		26	10	36	-0.10	0.15	0.1186	1.9509	-23.4828	
	SQCA 76-53	39	21	60	-0.15	0.15	0.1202	4.7300	-26.6176	
Direct Finite Element Approach	SQCA 12-13	-	-	-	0.0	0.20	0.1428	4.9600	-42.3894	
	SQCA 36-29	-	-	-	-0.10	0.15	0.1182	2.9340	-25.6447	

R = 200

TABLE III (cont.) Comparison of Numerical Results for Square Cavity Flow Problem

Method	Grid	Number of Modes			$x_{v.c.}$	$y_{v.c.}$	$\psi_{v.c.}$	$\zeta_{v.c.}$	$p_{v.c.}$	Grid for Plotting
		Symm.	Antisymm.	Total						
Modal	SQCA 12-13	10	5	15	0.0	0.15	0.1703	7.3450	-117.7910	20 x 20
		10	1	11	0.0	0.25	0.1790	5.1650	-78.950	
	SQCA 36-29	27	15	42	-0.05	0.10	0.1246	1.9322	-57.0767	
		26	10	36	-0.05	0.05	0.1279	2.1609	-51.2457	
	SQCA 76-53	39	21	60	-0.05	0.05	0.1315	1.2139	-54.7102	
Direct Finite Element Approach	SQCA 12-13	-	-	-	0.0	0.15	0.1703	7.3450	-117.7910	
	SQCA 36-29	-	-	-	-0.10	0.10	0.1319	4.6136	-58.6027	
[5]	SQCA 76-53	-	-	-	-0.056	0.083	0.1213	2.5099	-49.8779	irregular
[12]	SQC40 x 40	-	-	-	-0.06	0.12	0.102	2.15	-71.7	

R = 400

TABLE III (cont.) Comparison of Numerical Results for Square Cavity Flow Problem

Method & Grid	Reynolds Number, R							
	1	5	7	10	20	40	70	100
Friction Drag Coefficient, C_f								
Modal CYLFL 42-34	7.525	2.301	1.816	1.408	0.848	0.506	0.325	0.239
[6] 42	7.573	2.386	1.918	1.529	0.997	0.653	0.447	0.347
[13]	-	1.917	1.553	1.246	0.812	0.524	0.360	0.282
Pressure Drag Coefficient, C_p								
Modal CYLFL 42-34	7.557	2.538	2.089	1.712	1.199	0.896	0.737	0.654
[6] 42	7.837	2.704	2.263	1.906	1.443	1.149	0.965	0.874
[13]	-	2.199	1.868	1.600	1.233	0.998	0.852	0.774
Drag Coefficient, C_D								
Modal CYLFL 42-34	15.082	4.839	3.905	3.120	2.047	1.402	1.062	0.893
[6] 42	15.410	5.091	4.181	3.435	2.440	1.802	1.412	1.221
[13]2	-	4.116	3.421	2.846	2.045	1.522	1.212	1.056
[14]	10.109	-	3.303	2.800	2.013	1.536	-	-
Pressure at Leading Edge, $P(\pi)$								
Modal CYLFL 42-34	5.602	2.004	1.666	1.375	0.965	0.763	0.708	0.690
[6] 42	5.829	2.228	1.919	1.678	1.418	1.351	1.315	1.282
[13]	-	1.872	1.660	1.489	1.269	1.144	1.085	1.060
[14]	3.905	-	1.637	1.474	1.261	1.141	-	-
Pressure at Trailing Edge, $-P(0)$								
Modal CYLFL 42-34	3.876	1.222	1.013	0.845	0.638	0.545	0.502	0.479
[6] 42	3.845	1.242	1.050	0.896	0.698	0.580	0.488	0.436
[13]	-	1.044	0.8700	0.742	0.589	0.509	0.439	0.393
[14]	2.719	-	0.783	0.670	0.537	0.512	-	-

TABLE IV Comparison of Numerical Results for Flow Around a Circular Cylinder

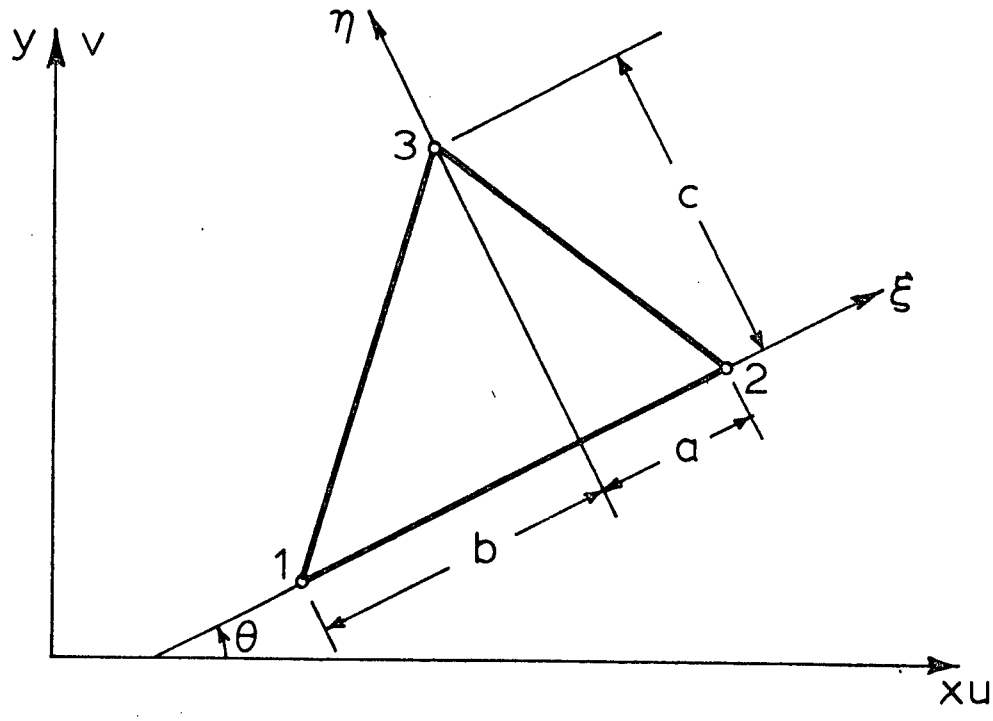

FIGURE 1 LOCAL (ξ,η) COORDINATES OF THE TRIANGULAR ELEMENT

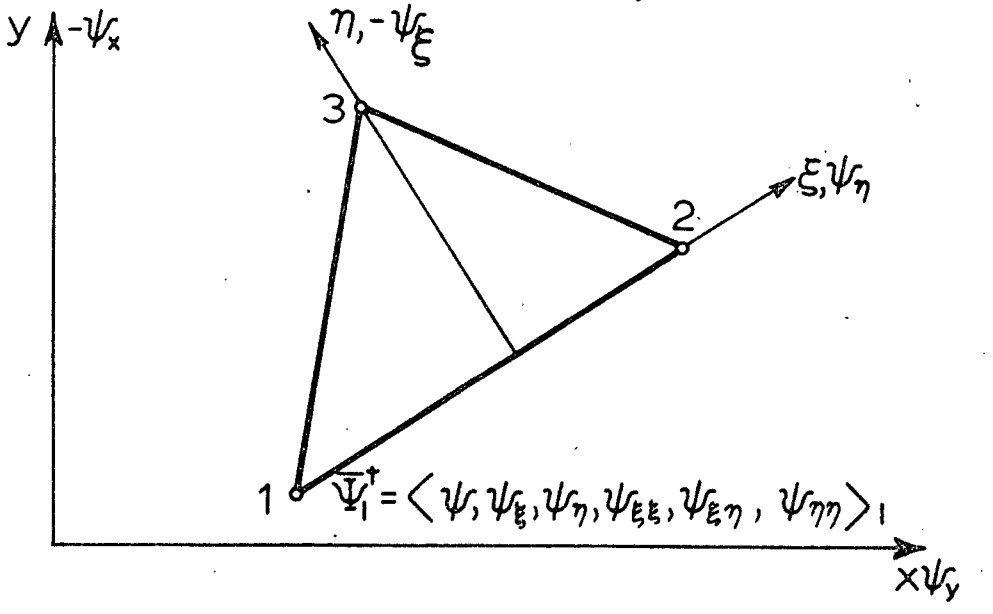

FIGURE 2 THE 18 DOF TRUNCATED QUINTIC ELEMENT

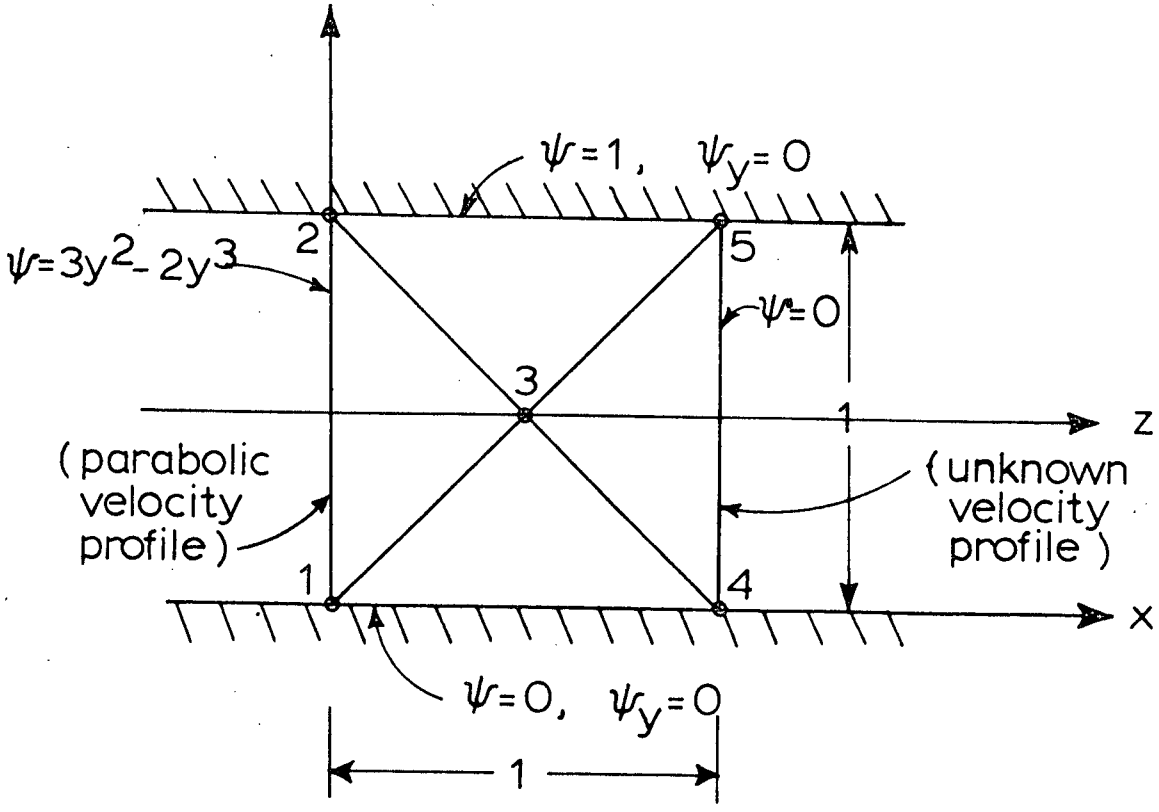

FIGURE 3 POISEUILLE FLOW PROBLEM CONFIGURATION

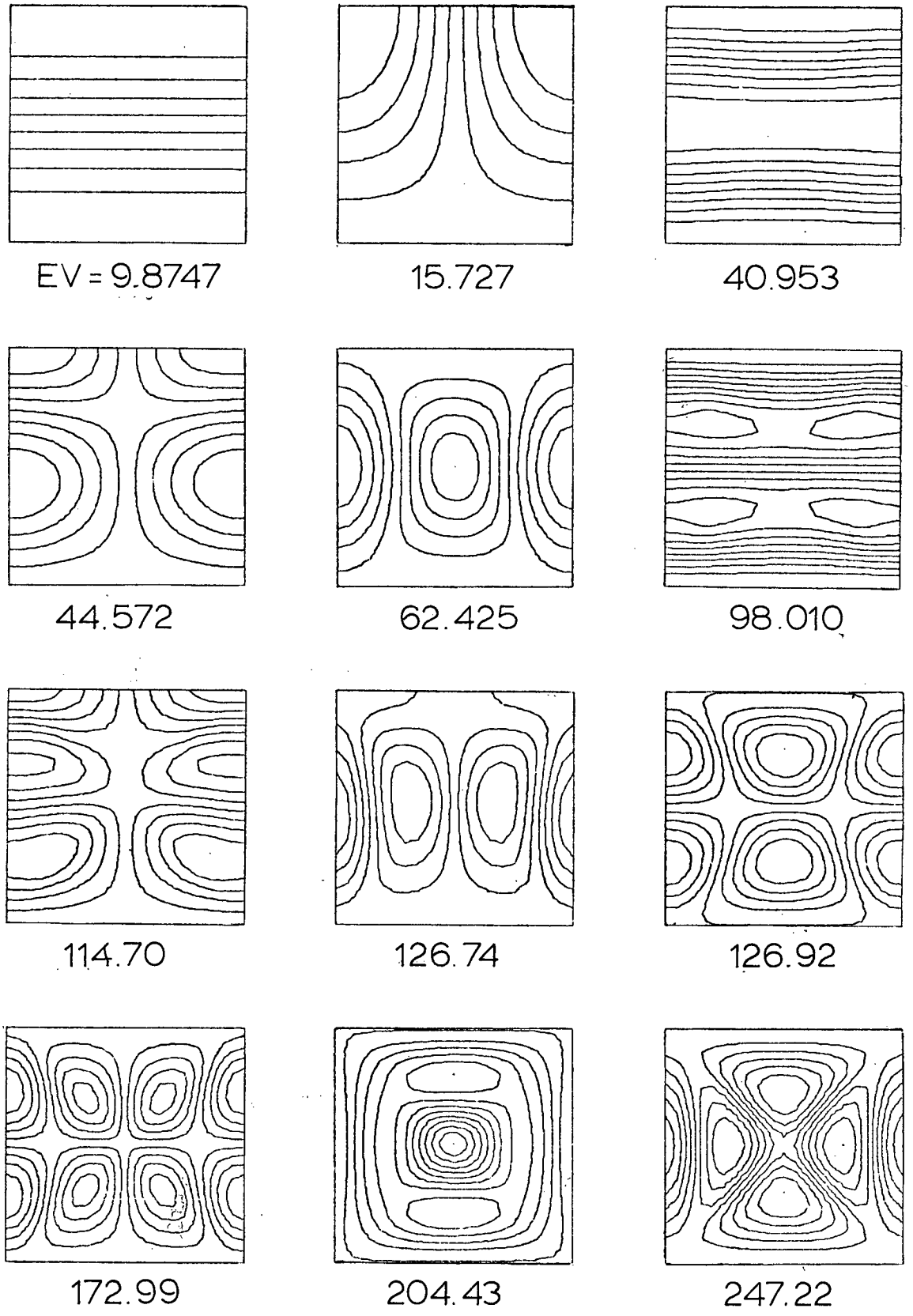

FIGURE 4 MODE SHAPES & EIGENVALUES FOR POISEUILLE FLOW

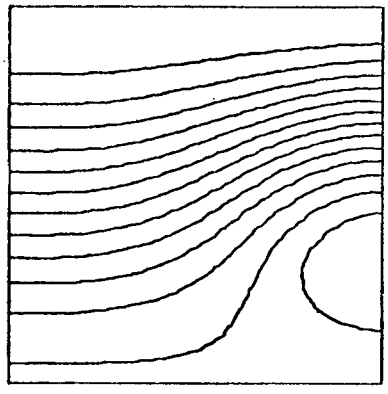

5 MODES
V_3 = 1.57808

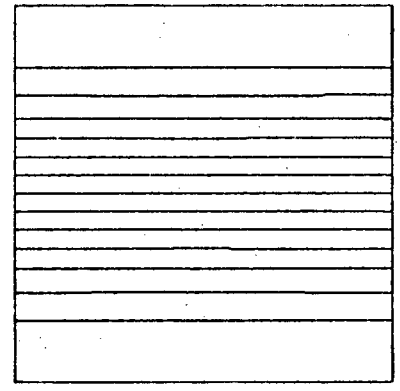

6 MODES
V_3 = 1.57524

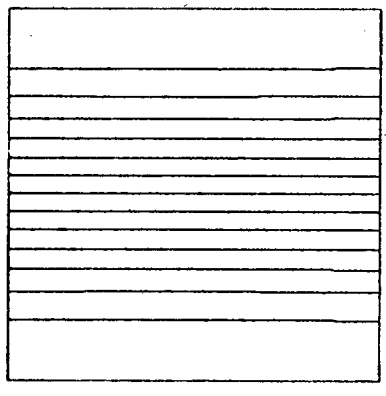

7 MODES
V_3 = 1.51168

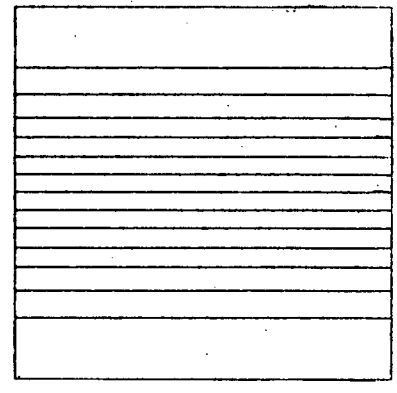

12 MODES
V_3 = 1.50000

FIGURE 5 STREAMLINES & VELOCITIES AT MIDNODE 3 FOR POISEUILLE FLOW

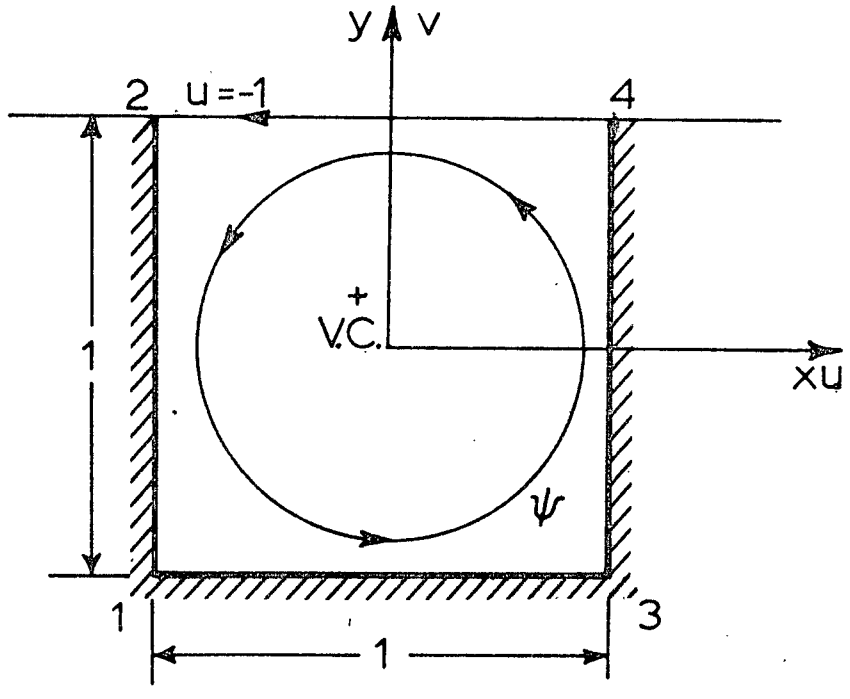

FIGURE 6 CIRCULATORY FLOW INDUCED BY A MOVING LID OVER A SQUARE CAVITY

(a)

SQCA 13-12

NE = 12, NO = 13
NNS = 15, NNP = 77
LBS = 13, LBP = 54

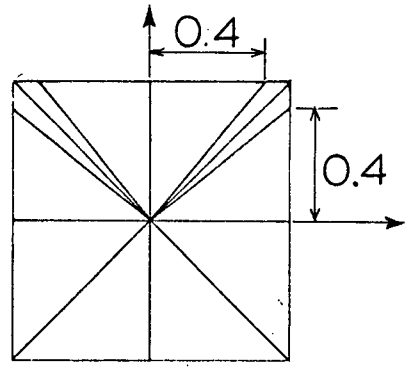

(b)

SQCA 36-29

NE = 36, NO = 29
NNS = 71 NNP = 173
LBS = 32 LBP = 78

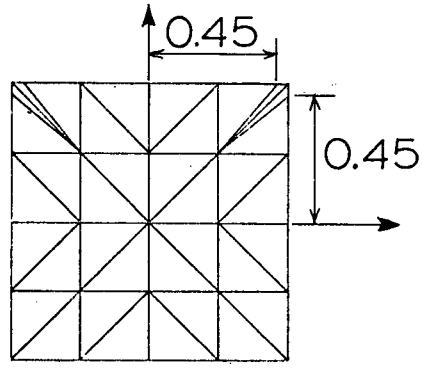

(c)

SQCA 76-53

NE = 76, NO = 53
NNS = 175 NNP = 317
LBS = 44 LBP = 78

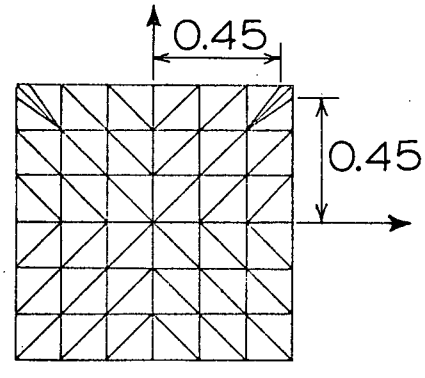

NE = NO. OF ELEMENTS, NO = NO. OF NODES
NN = NET NO. OF UNKNOWNS
LB = HALF BANDWIDTH
S = STREAM FUNCTION
P = PRESSURE

FIGURE 7 FINITE ELEMENT GRIDS FOR SQUARE CAVITY FLOW

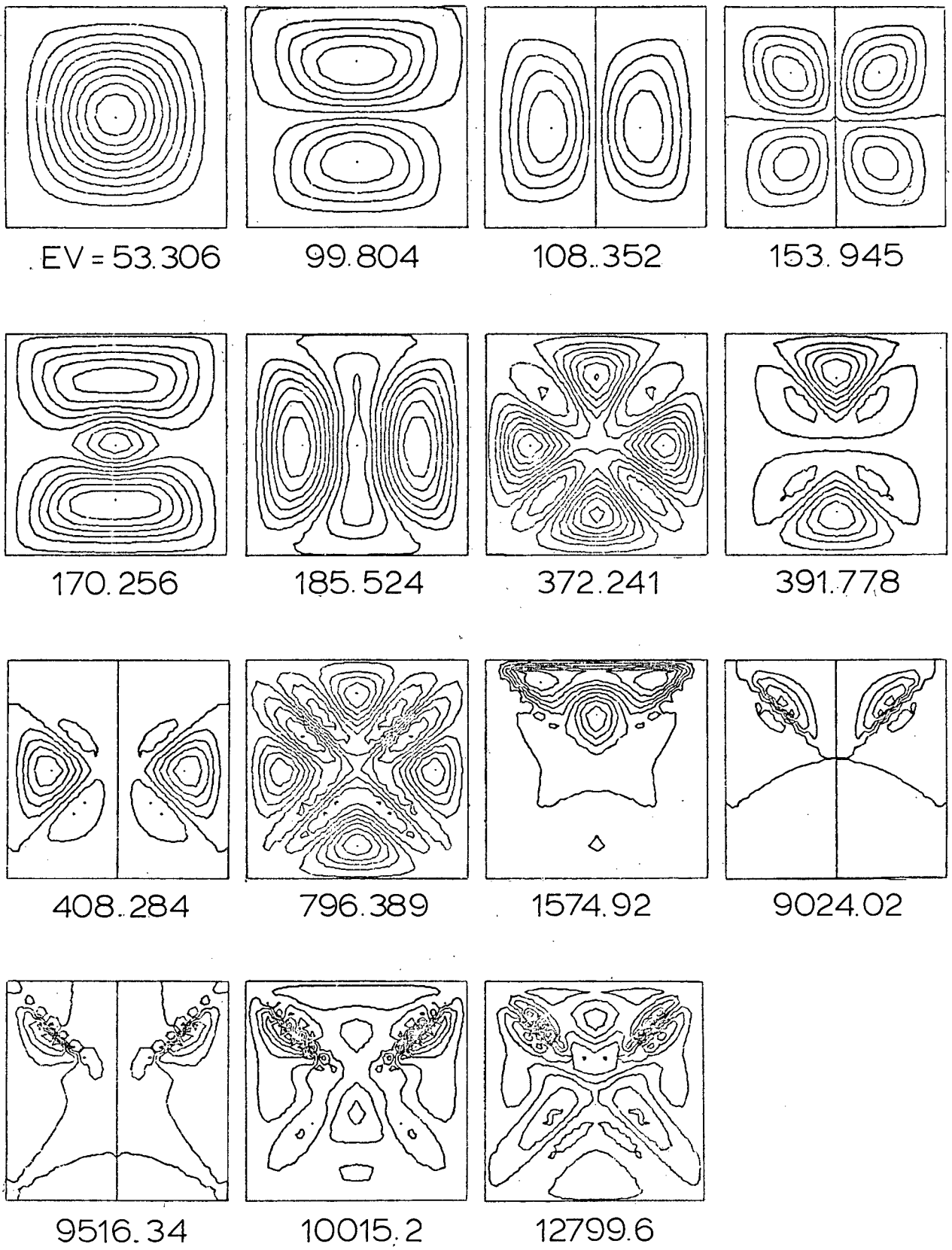

FIGURE 8-1 MODE SHAPES & EIGENVALUES FOR SQCA 12-13 GRID

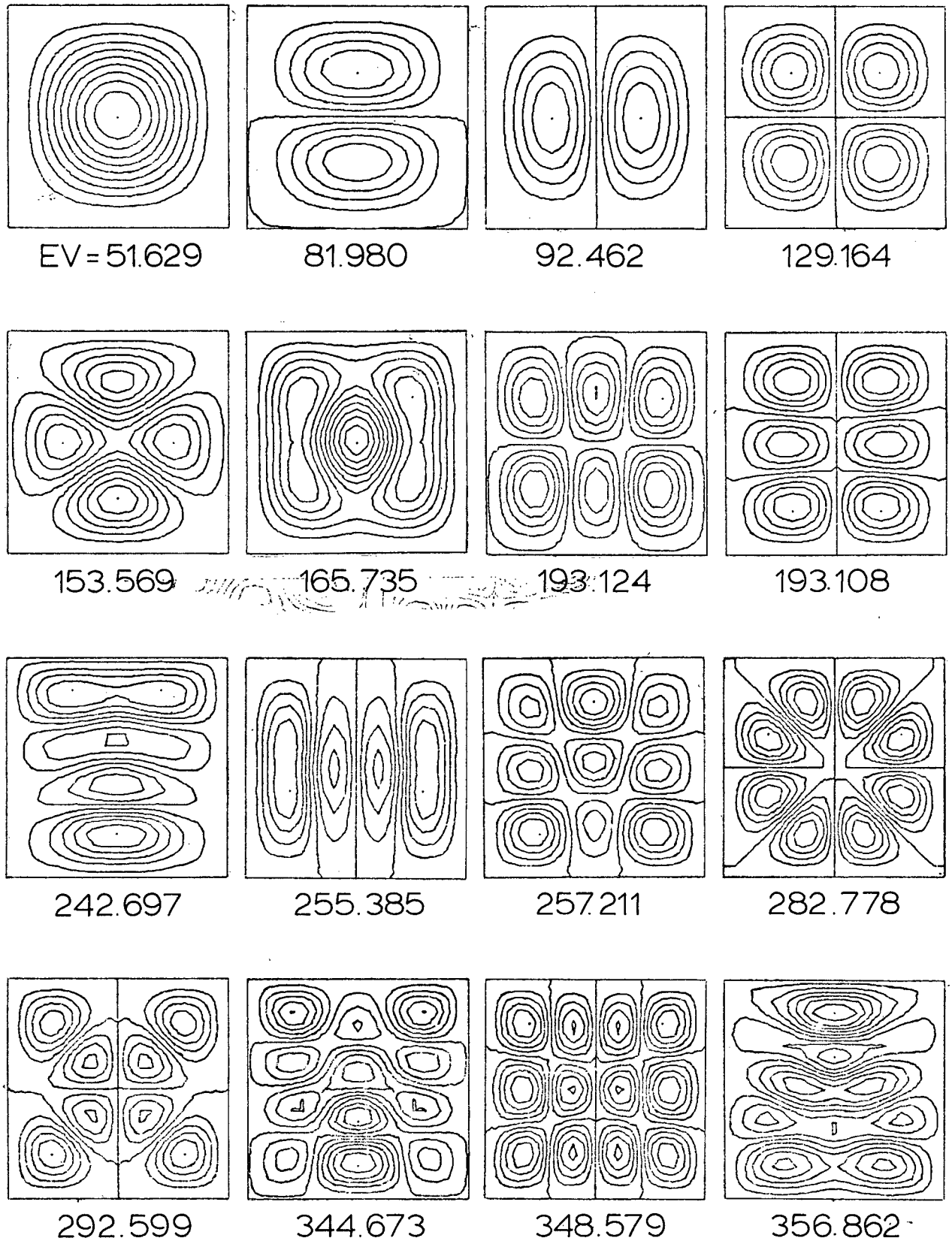

FIGURE 8 - 2 FIRST 30 MODE SHAPES & EIGENVALUES FOR SQCA 36-29 GRID

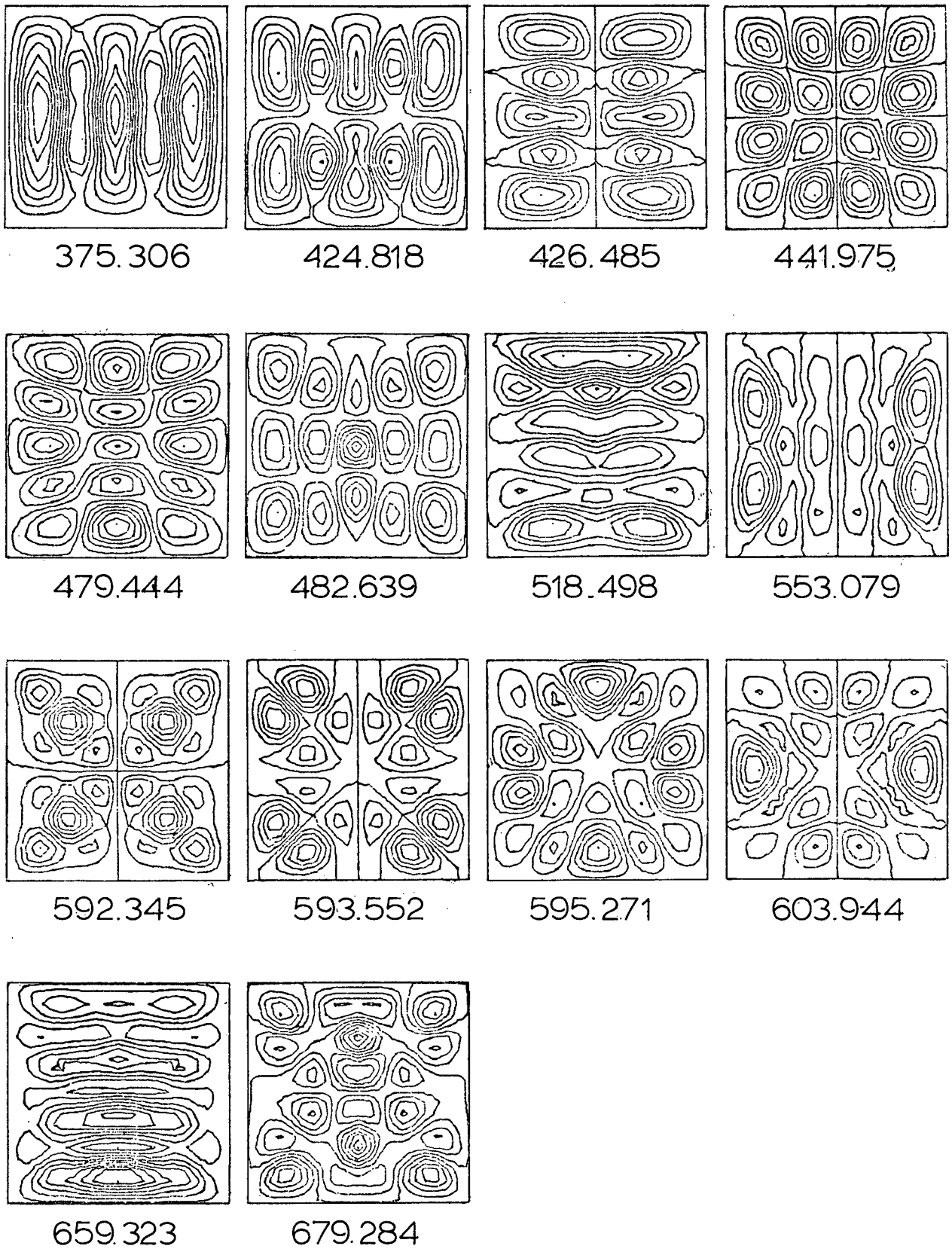

FIGURE 8-2 (CONT.) FIRST 30 MODE SHAPES & EIGENVALUES FOR SQCA 36-29 GRID

Figure 9 Streamlines for Square Cavity Flow for Various Reynolds Numbers R

Contours represent equal steps in stream function, unless specified otherwise. The vortex centre is marked by a cross. The numbers below the figures refer to the number of modes used in the calculations, while FE denotes the direct finite element approach.

(a)

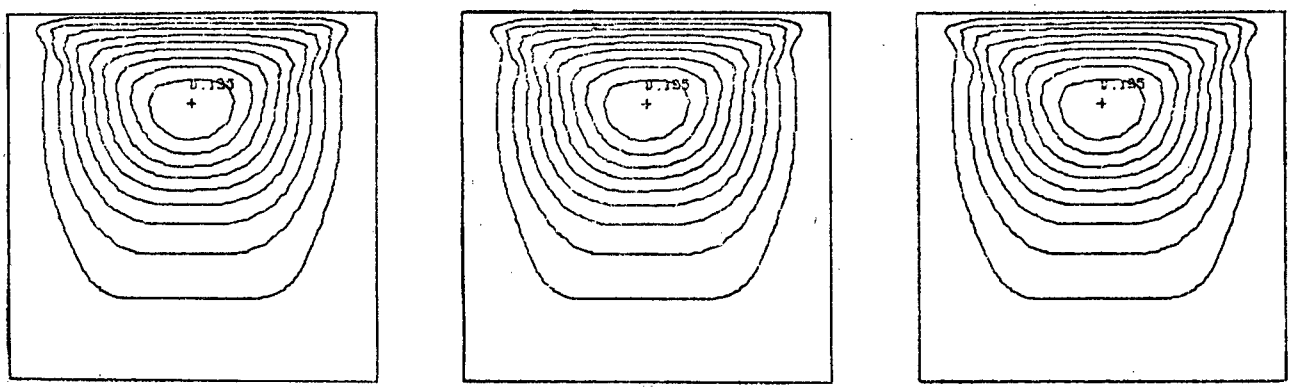

11 15 FE

(b)

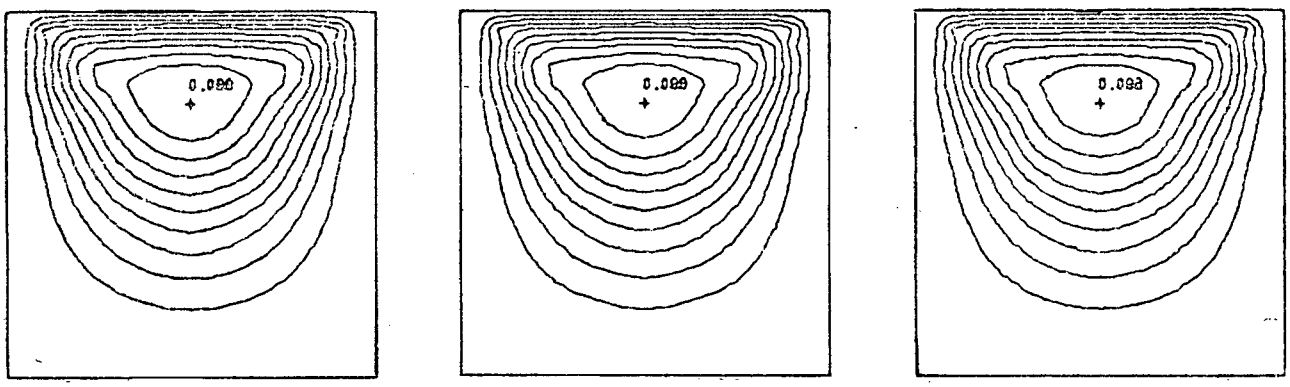

36 42 FE

(c)

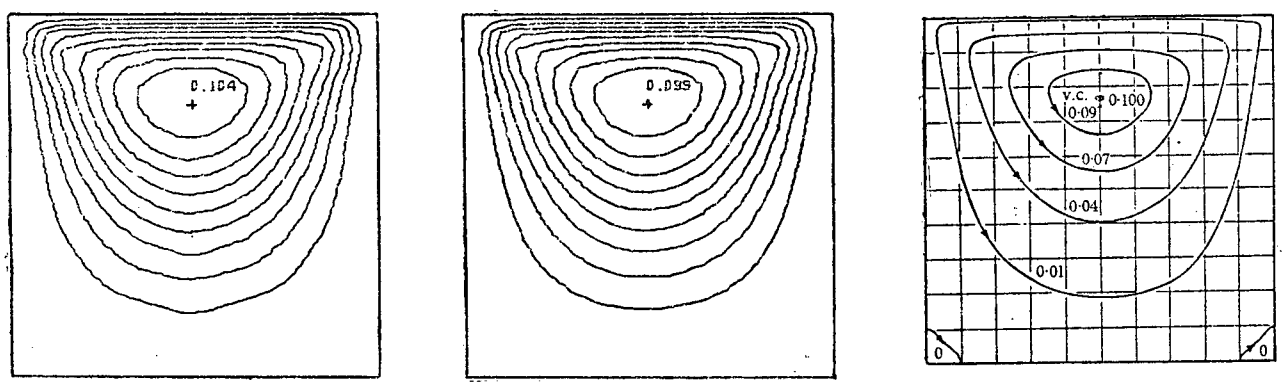

60 FE REF. 12

FIGURE 9-1 R = 0

(a)

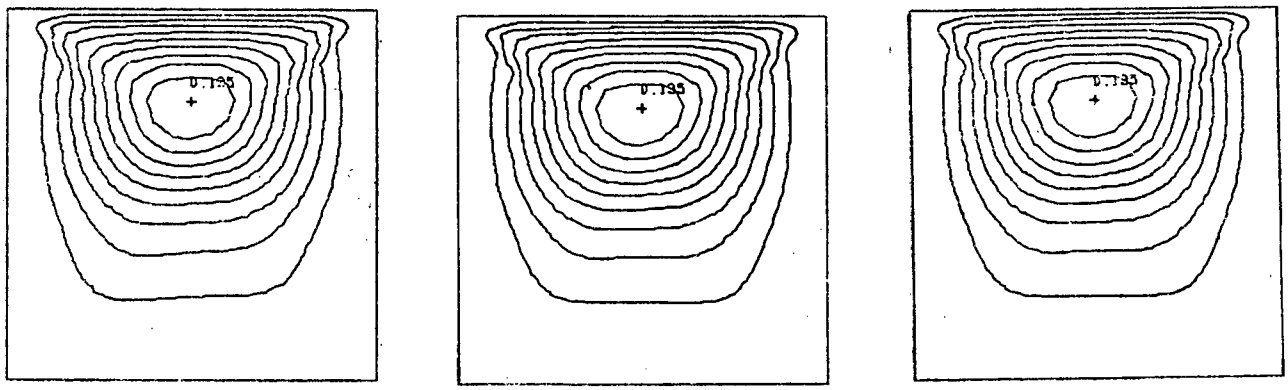

11 15 FE

(b)

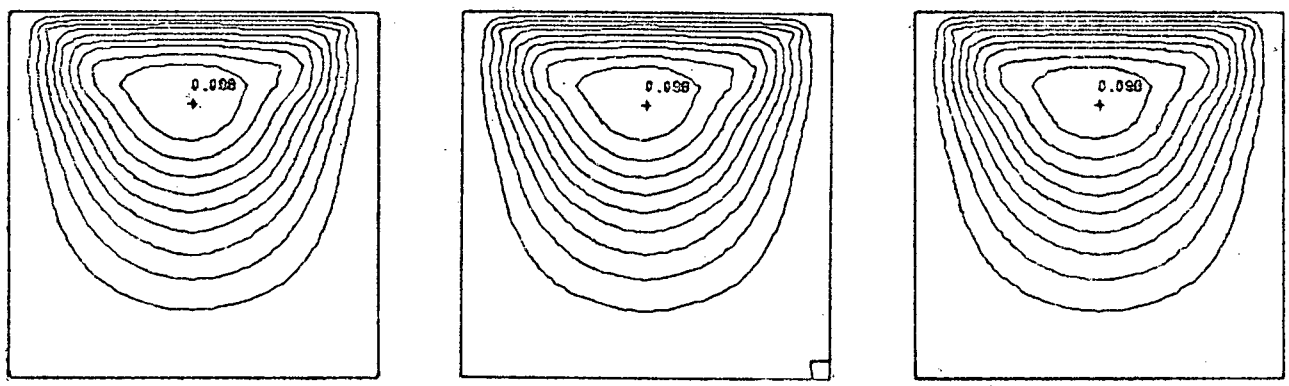

36 42 FE

(c)

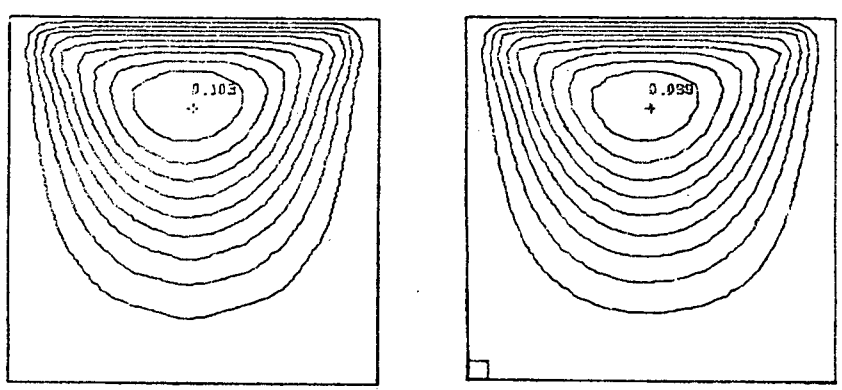

60 FE

FIGURE 9-2 R = 10

(a)

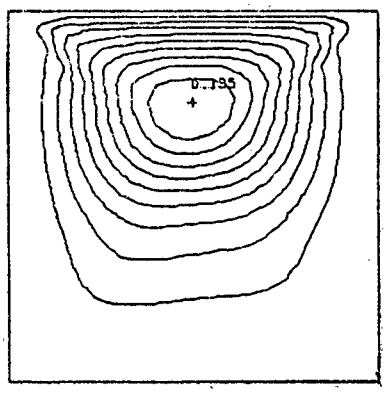

11

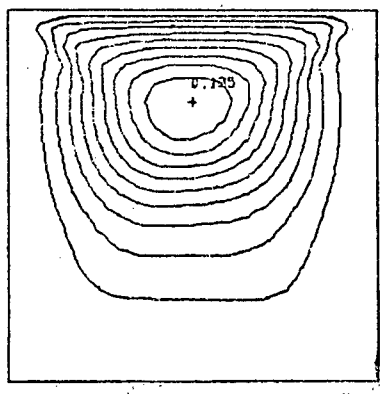

15

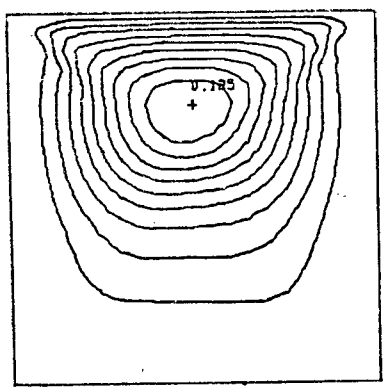

FE

(b)

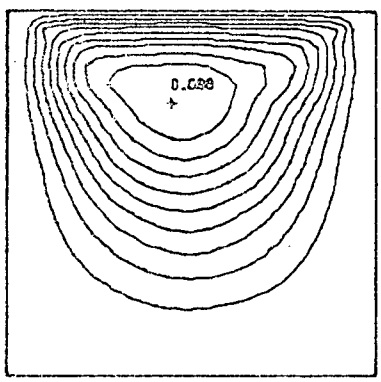

36

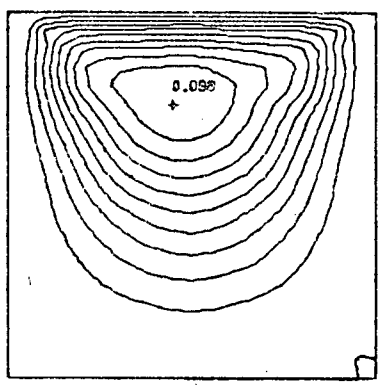

42

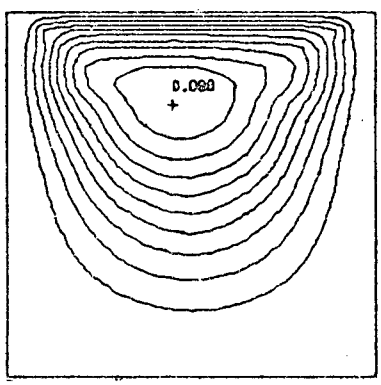

FE

(c)

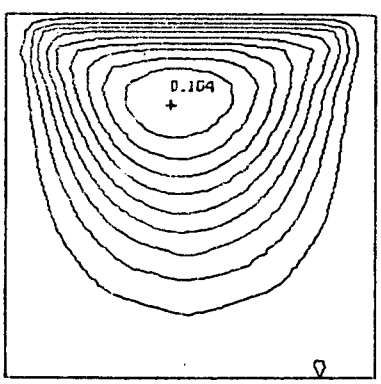

60

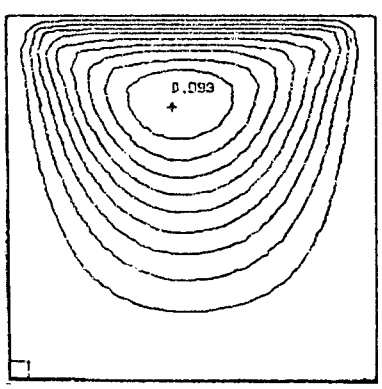

FE

FIGURE 9-3 R = 20

(a)

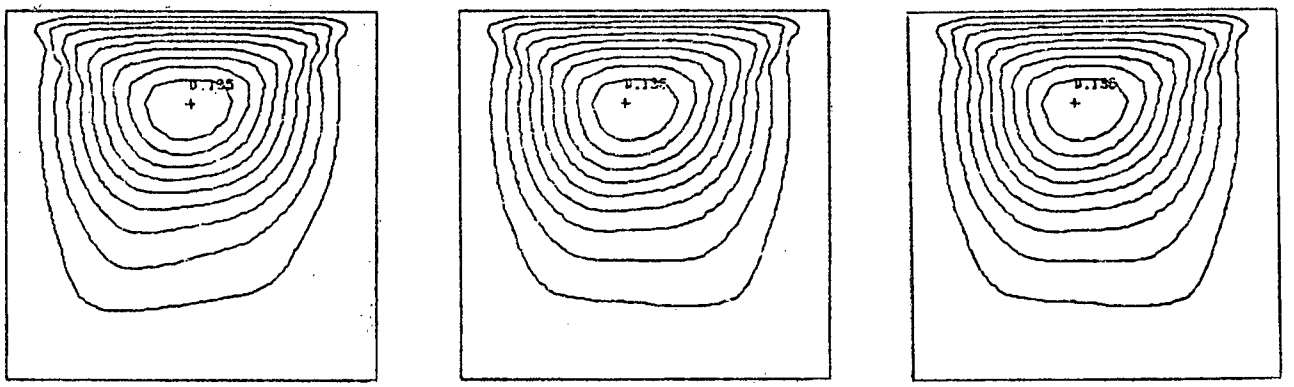

11 15 FE

(b)

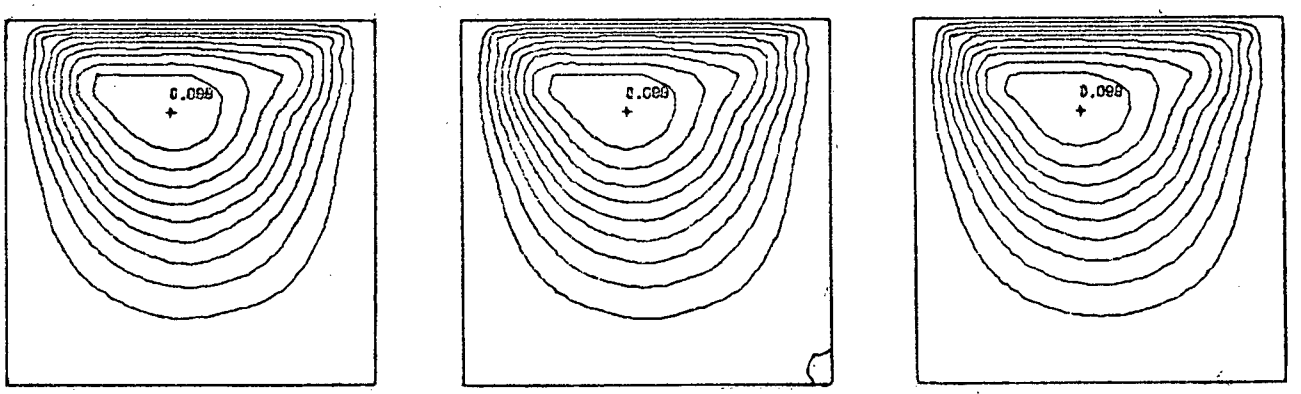

36 42 FE

(c)

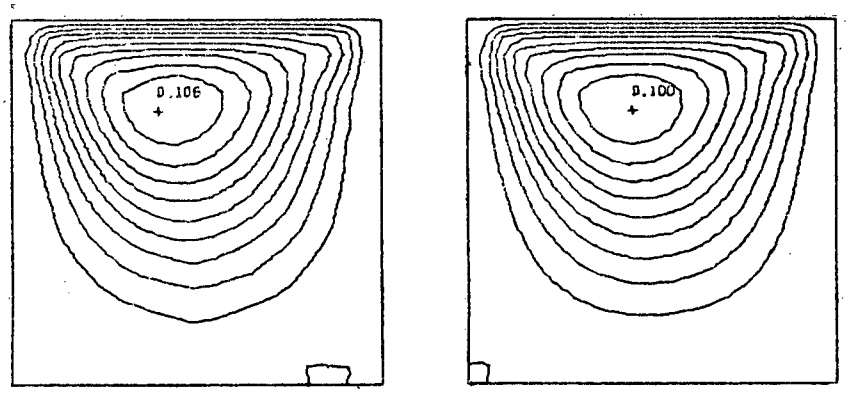

60 FE

FIGURE 9-4 R = 40

(a)

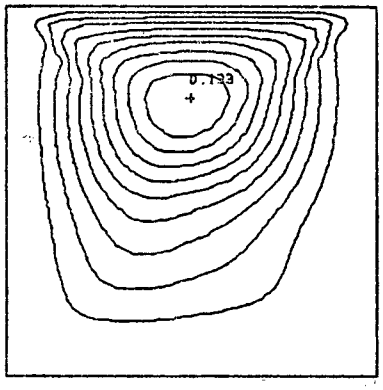

11

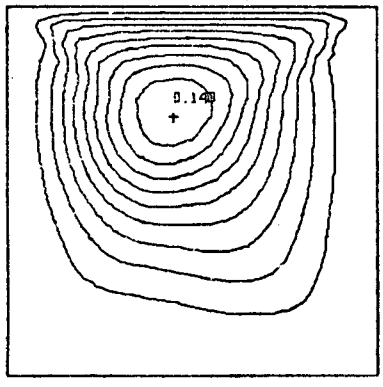

15

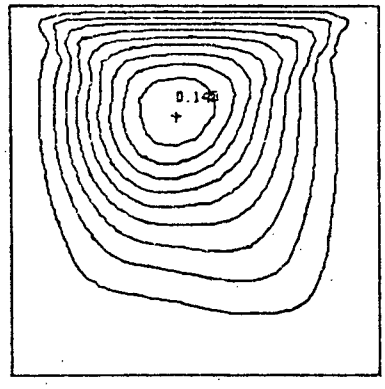

FE

(b)

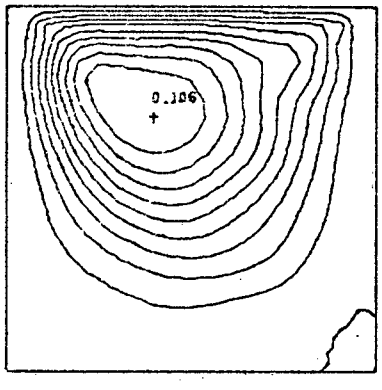

36

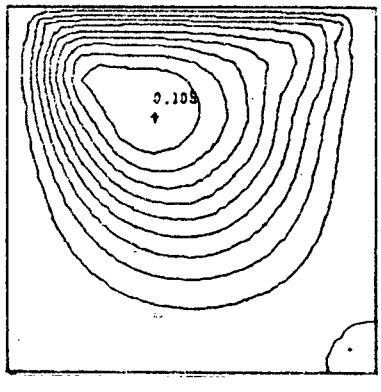

42

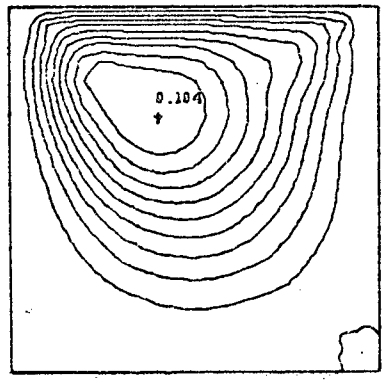

FE

(c)

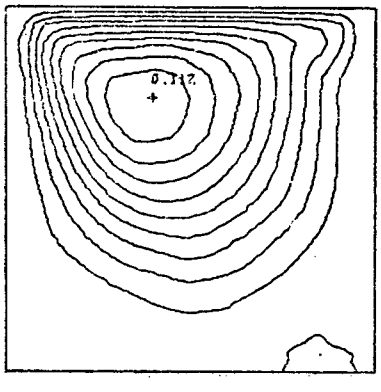

60

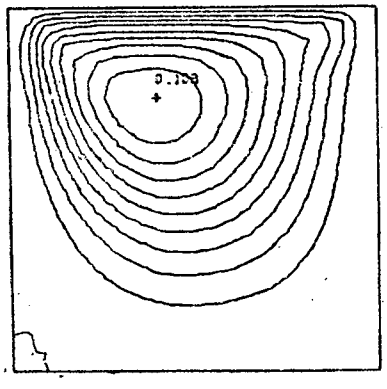

FE

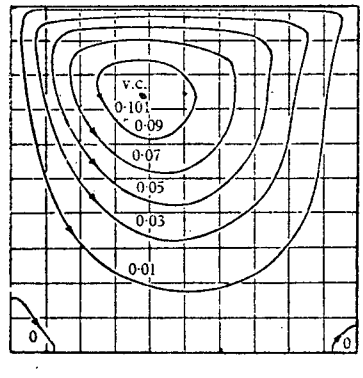

REF. 12

FIGURE 9-5 R = 100

(a)

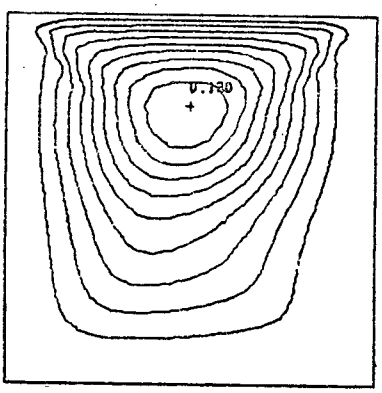

11

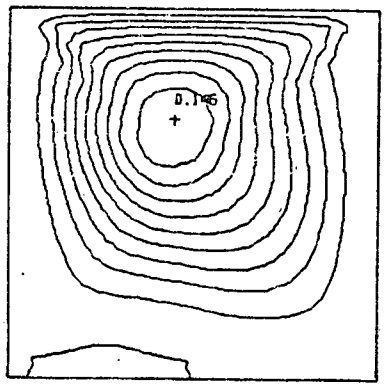

15

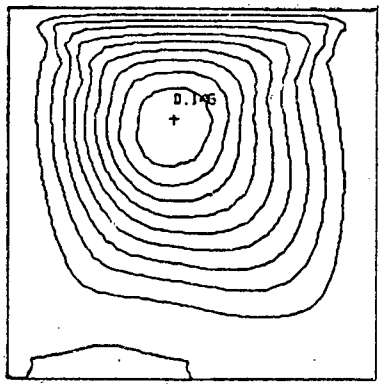

FE

(b)

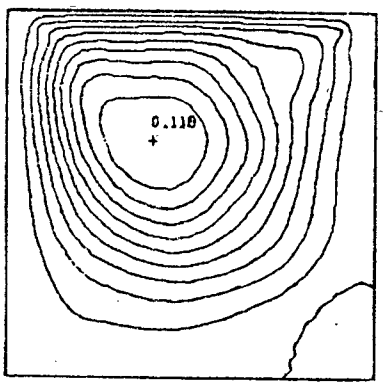

36

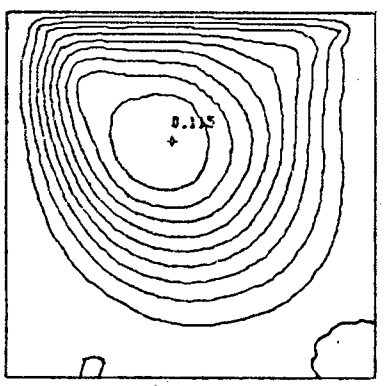

42

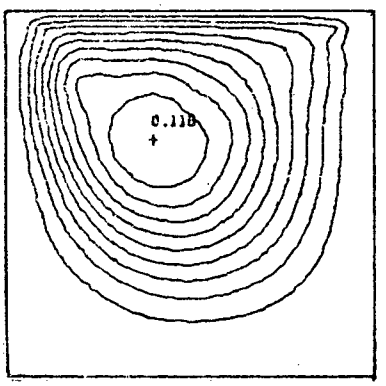

FE

(c)

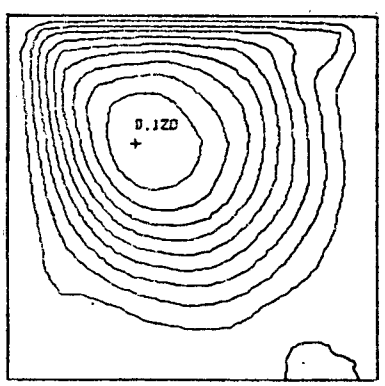

60

FIGURE 9-6 R = 200

(a)

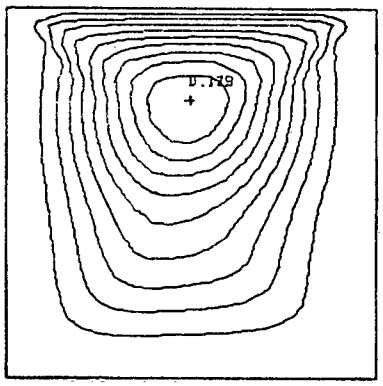

11

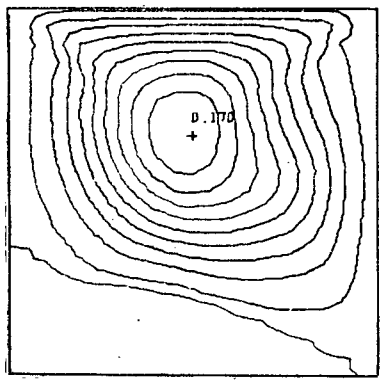

15

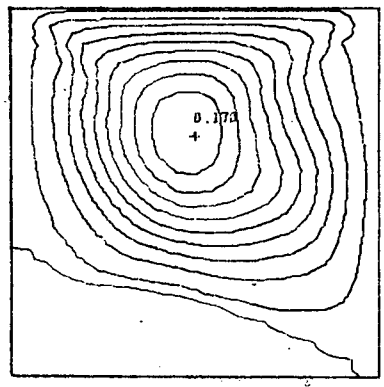

FE

(b)

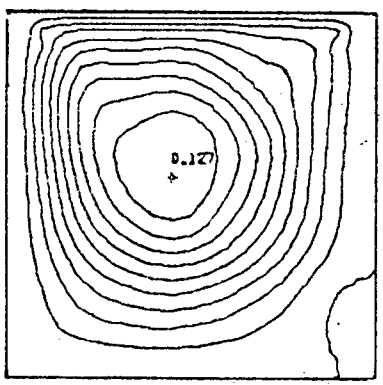

36

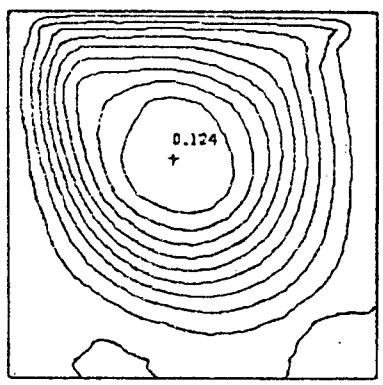

42

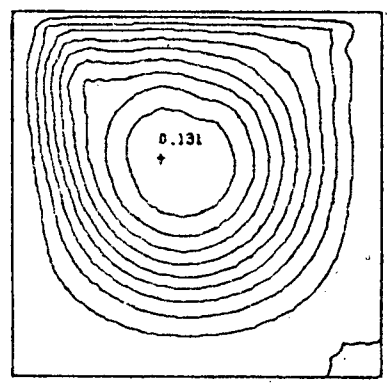

FE

(c)

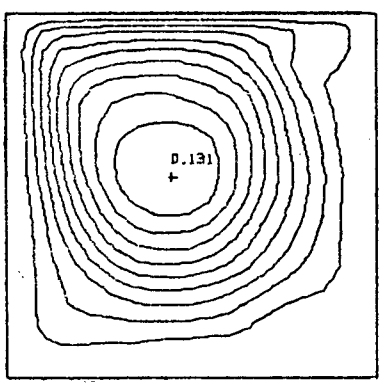

60

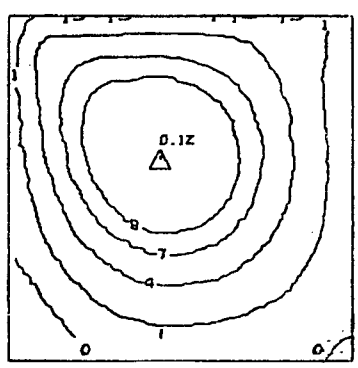

REF. 5

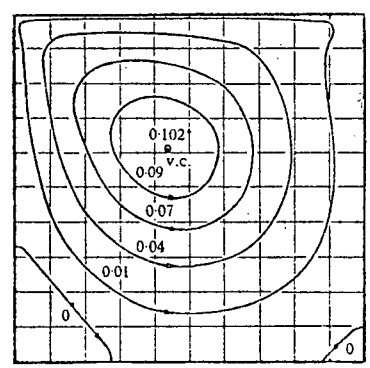

REF. 12

FIGURE 9-7 R = 400

Figure 10 Equi-Vorticity Lines for Square Cavity Flow for Various Reynolds Numbers R

The vortex centre is marked by a cross. The numbers below the figures refer to the number of modes used in the calculations, while FE denotes the direct finite element approach. Contour levels are labelled only on the central figure. For R = 0, 10,20,40 and 100, ψ = -1.0,0.0,1.0,3.0,5.0 contours are plotted, and for R = 200 and 400, ψ = -1.0,0.0,1.0,2.0,2.2, and 3.0 contours.

(a)

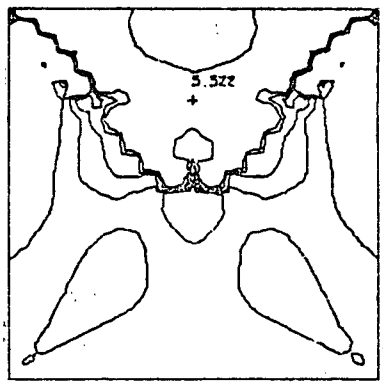

11

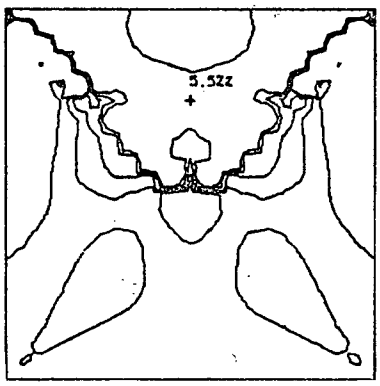

15

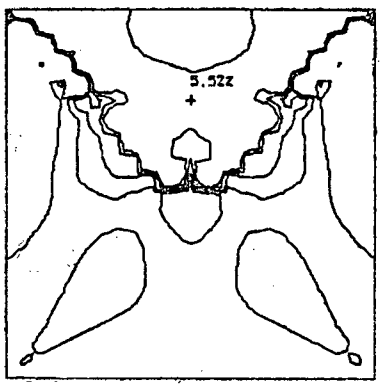

FE

(b)

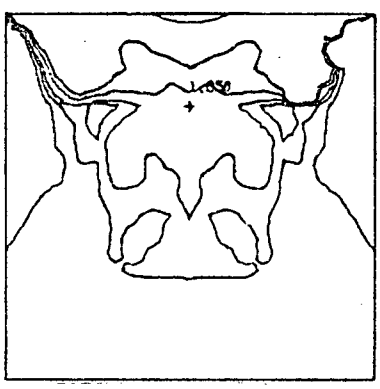

36

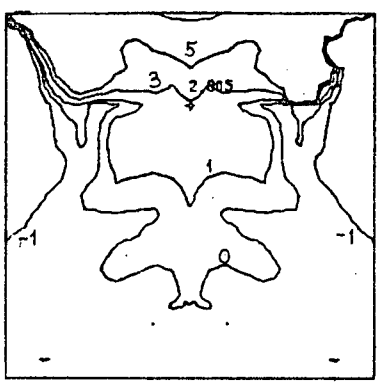

42

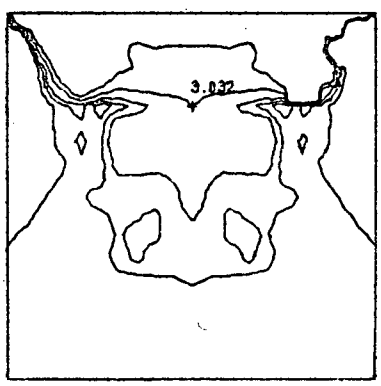

FE

(c)

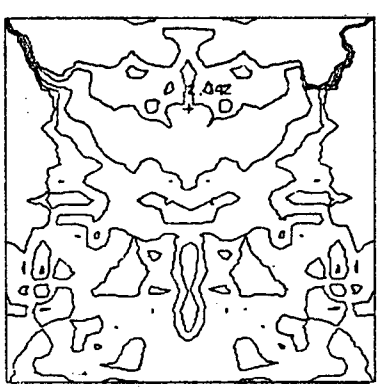

60

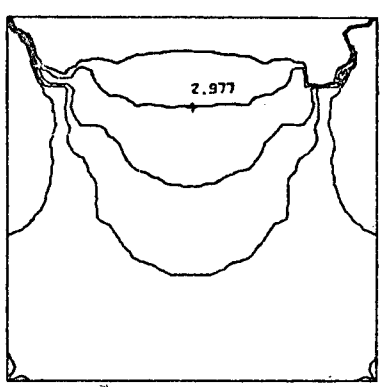

FE

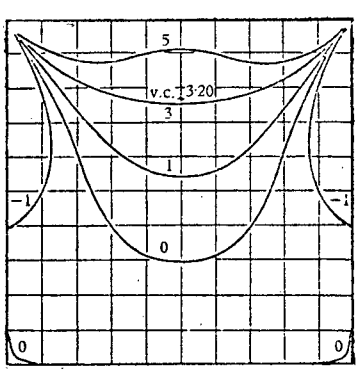

REF. 12

FIGURE 10-1 R = 0

(a)

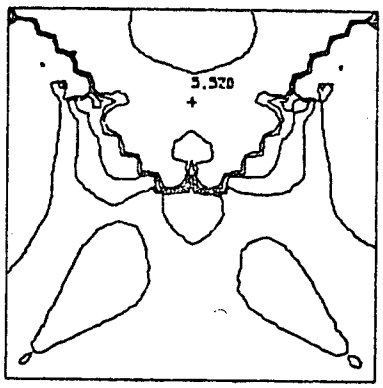

11

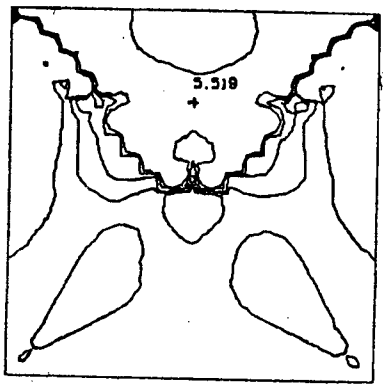

15

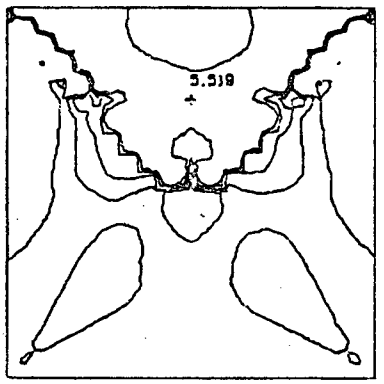

FE

(b)

36

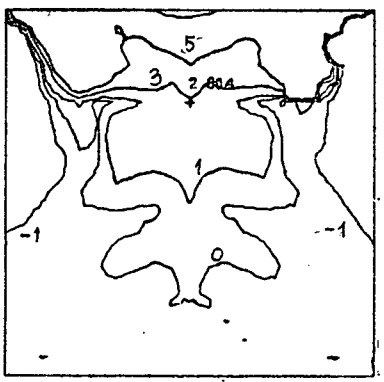

42

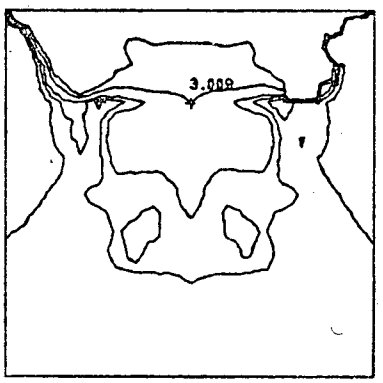

FE

(c)

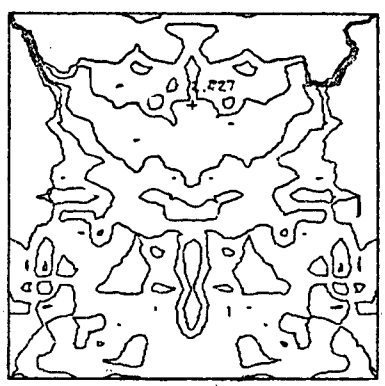

60

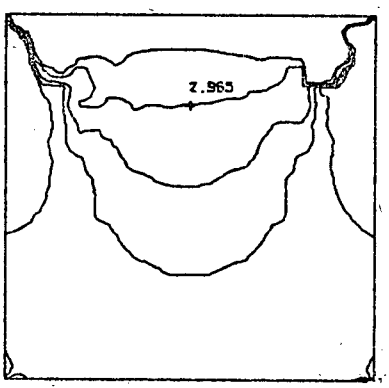

FE

FIGURE 10-2 R = 10

(a)

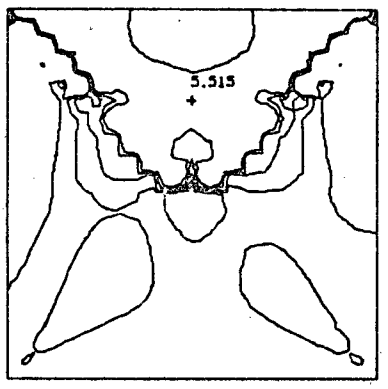

11

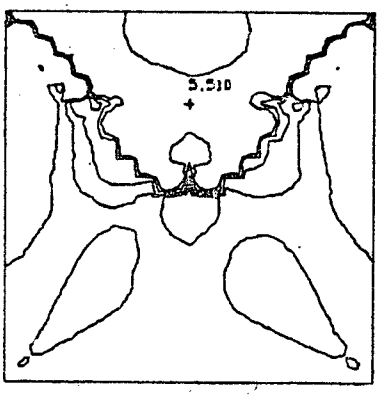

15

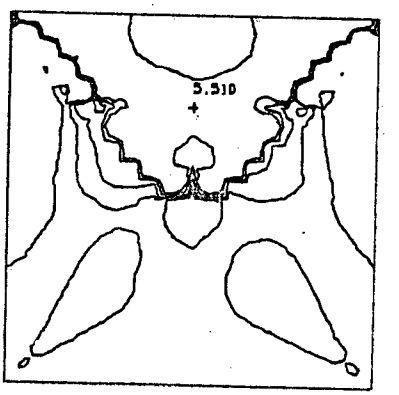

FE

(b)

36

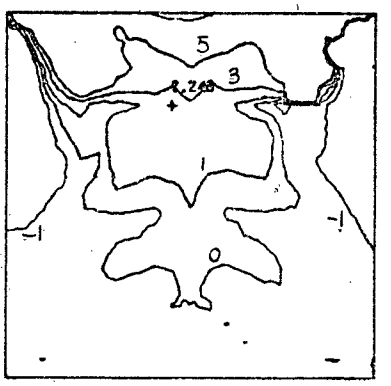

42

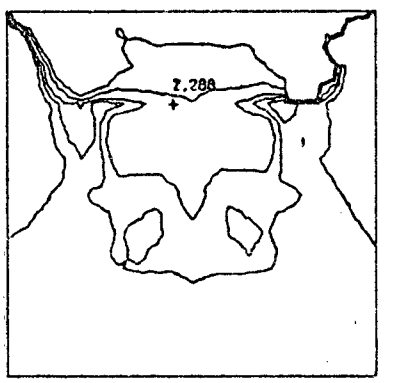

FE

(c)

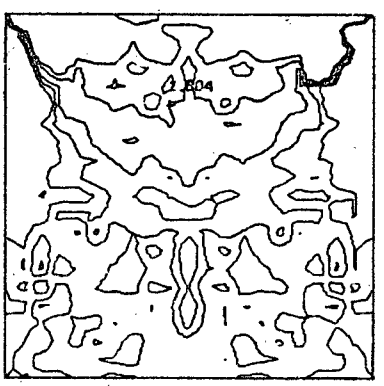

60

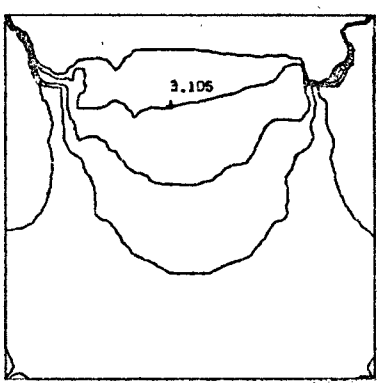

FE

FIGURE 10 - 3 R = 20

(a)

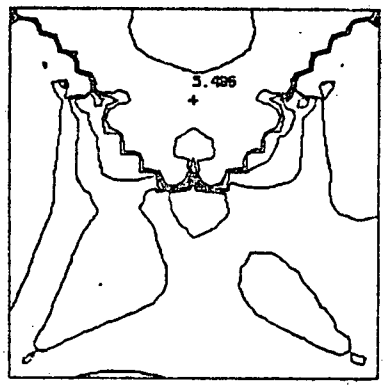

11

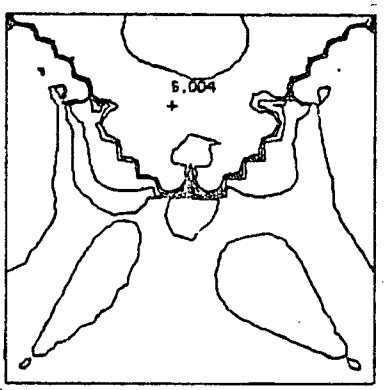

15

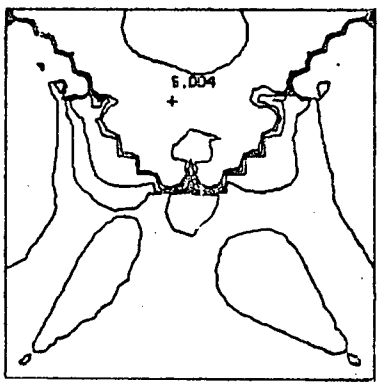

FE

(b)

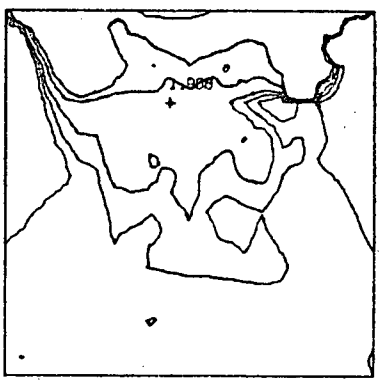

36

42

FE

(c)

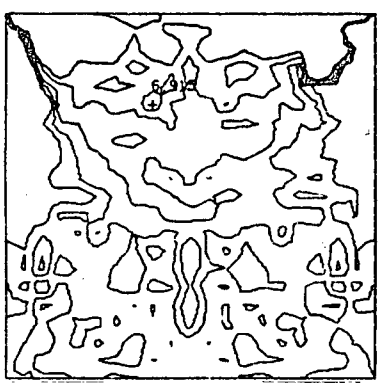

60

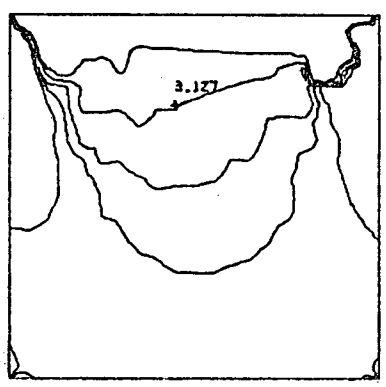

FE

FIGURE 10 - 4 R = 40

(a)

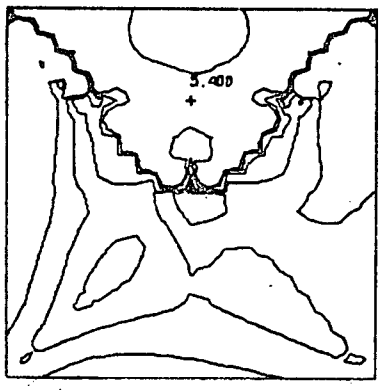

11

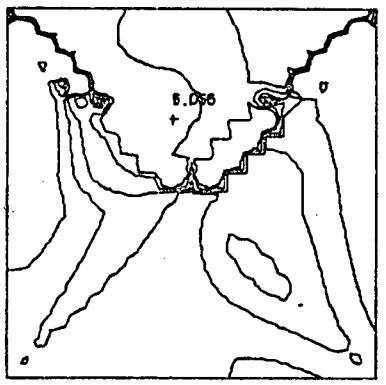

15

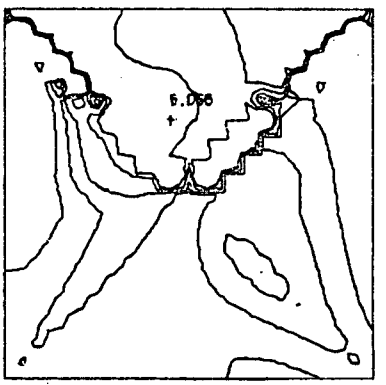

FE

(b)

36

42

FE

(c)

60

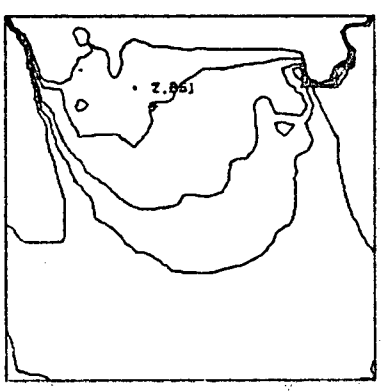

FE

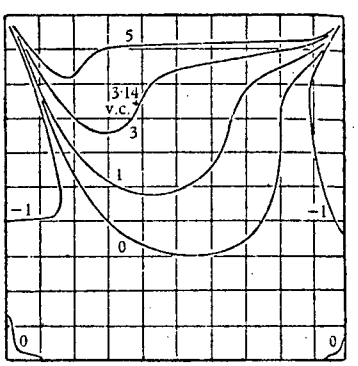

REF. 12

FIGURE 10 - 5 R = 100

(a)

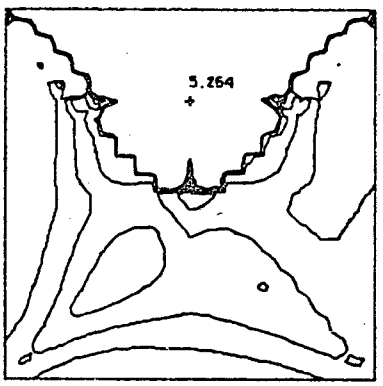

11

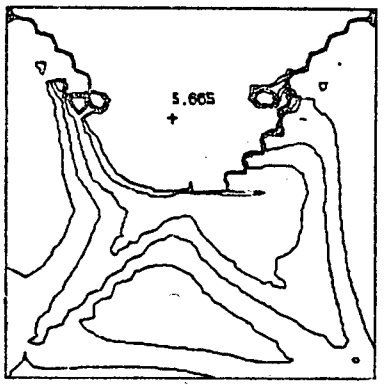

15

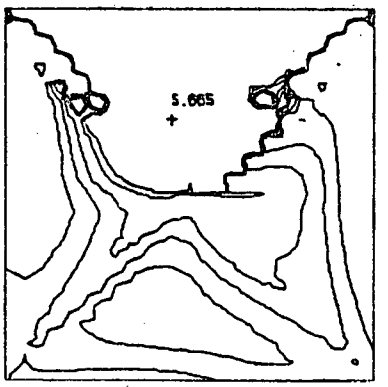

FE

(b)

36

42

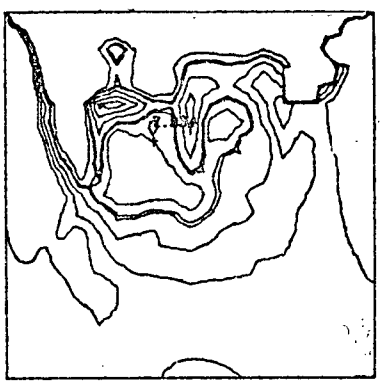

FE

(c)

60

FIGURE 10-6 R = 200

(a)

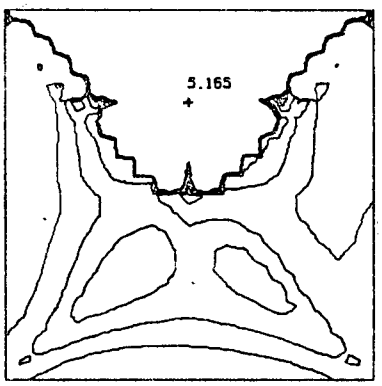

11

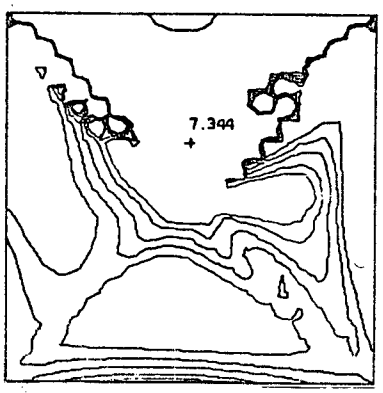

15

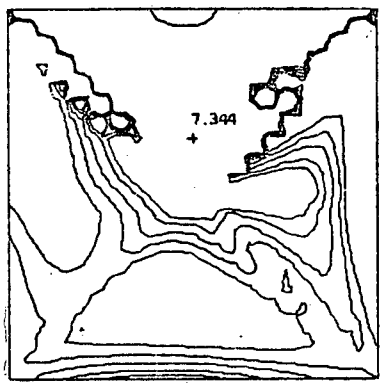

FE

(b)

36

42

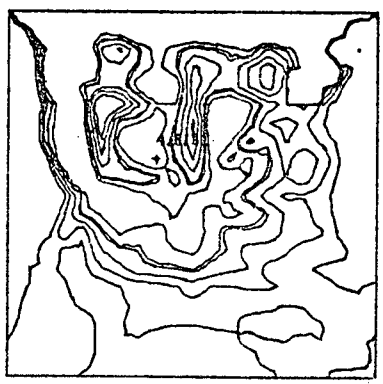

FE

(c)

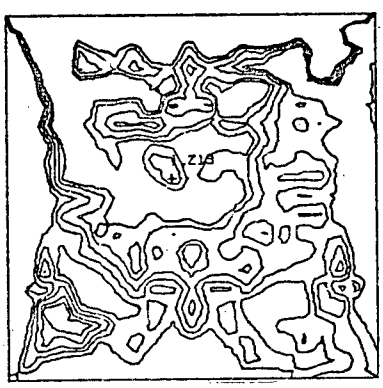

60

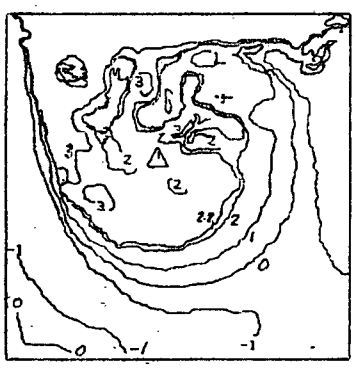

REF. 5

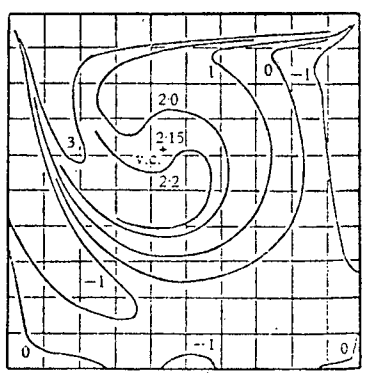

REF. 12

FIGURE 10-7 R = 400

Figure 11 Equi-Pressure Lines for Square Cavity Flow for Various Reynolds Numbers R

The vortex centre is marked by a cross. The numbers below the figures refer to the number of modes used in the calculations, while FE denotes the direct finite element approach. Contour levels are labelled only on the central figure. For R = 0,10,20, and 40, p = -20.0,-10.0,-5.0,-1.0,0.0,1.0,5.0,10.0, and 20.0, contours are plotted, for R = 100 p = -15.0,-7.5,-0.5, 0.0 and 15.0 contours, for R = 200 p = -20.0,-10.0, -5.0,-1.0,0.0,30.0, and 60.0 contours and for R = 400 p = -60.0,-30.0,0.0,30.0 and 60.0 contours.

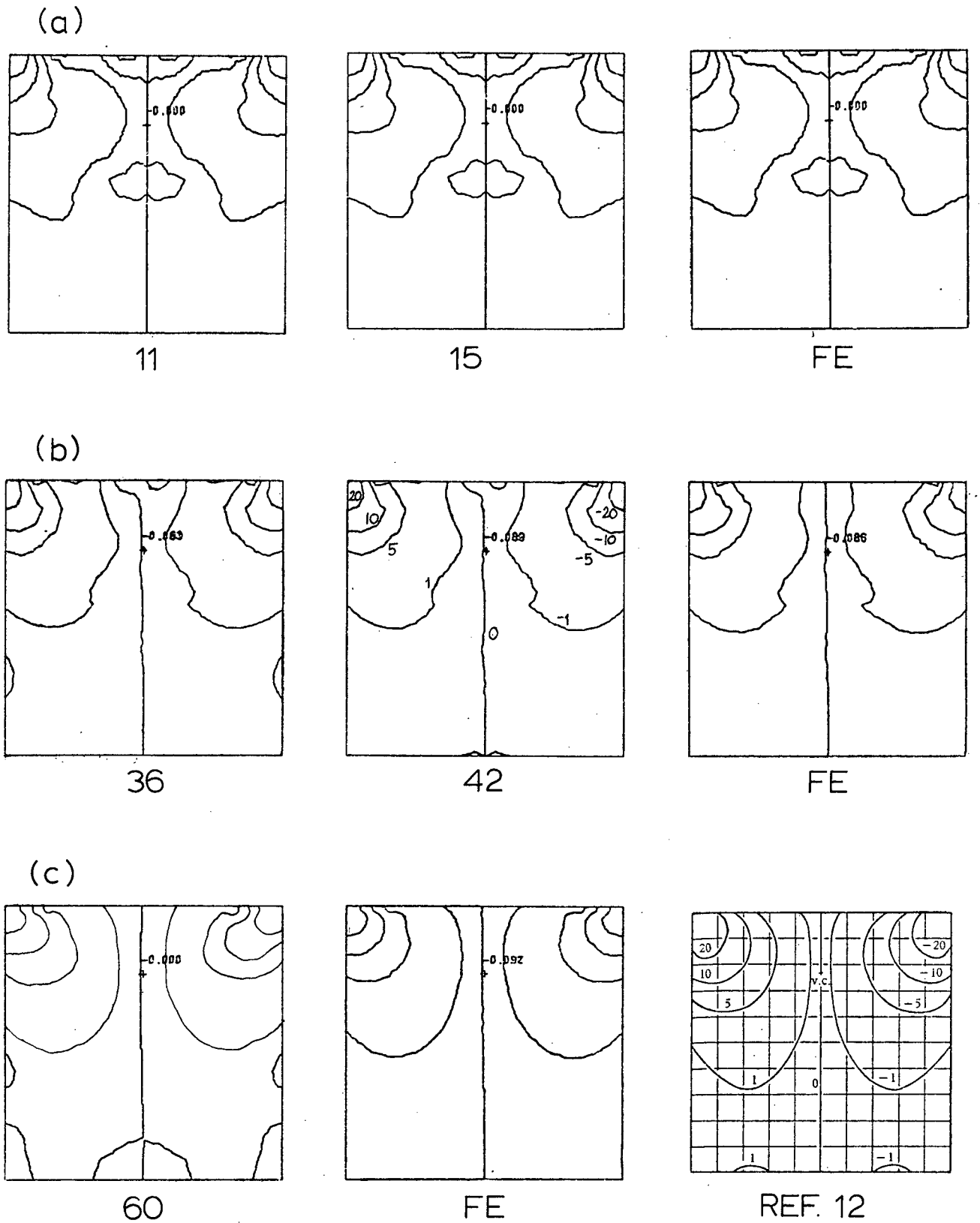

FIGURE 11-1 R=0

(a)

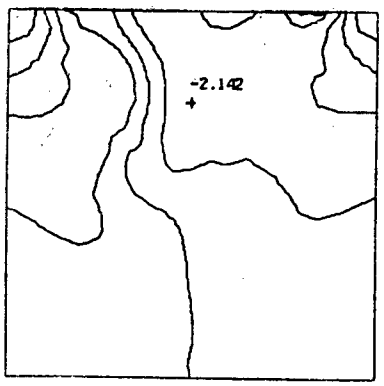

11

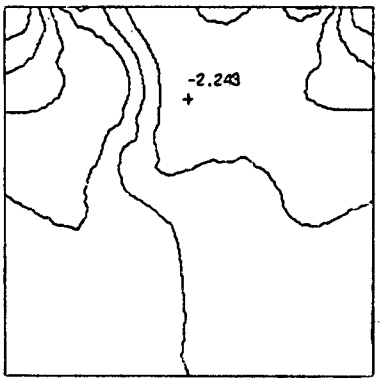

15

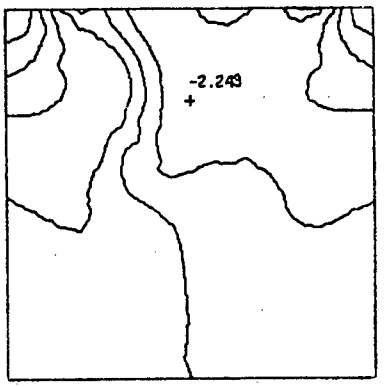

FE

(b)

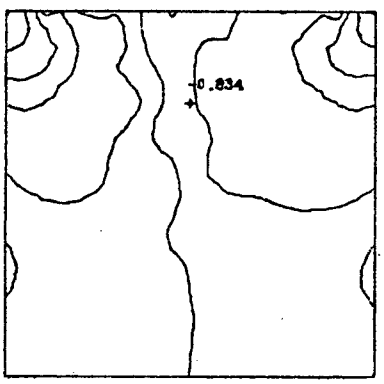

36

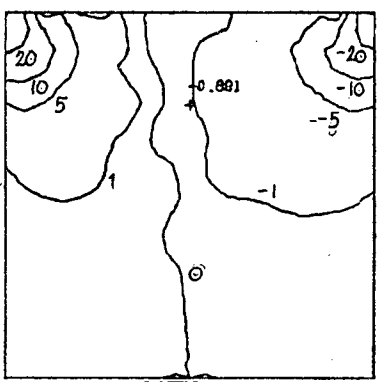

42

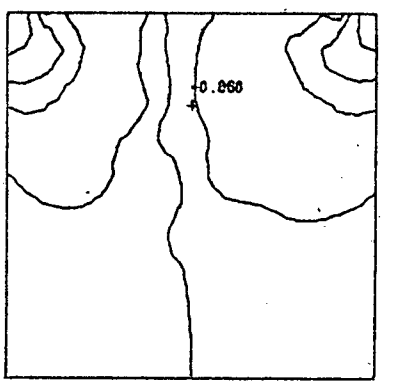

FE

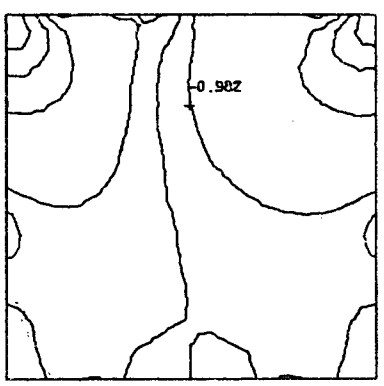

60

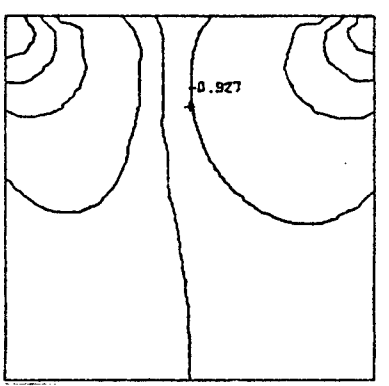

FE

FIGURE 11-2 R = 10

(a)

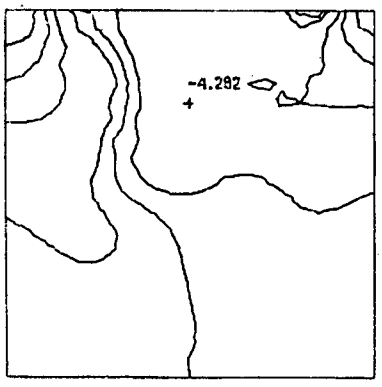

11

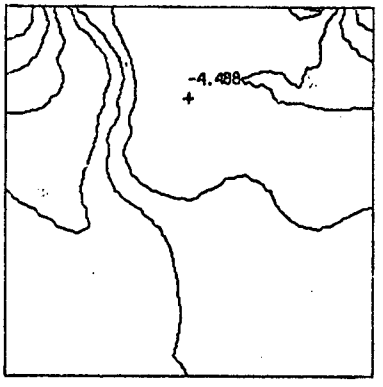

15

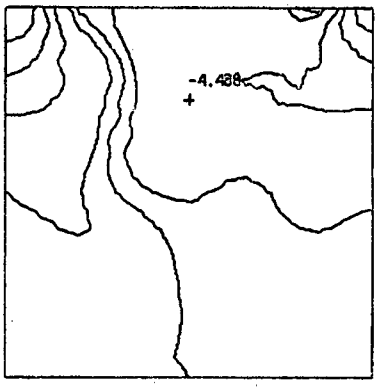

FE

(b)

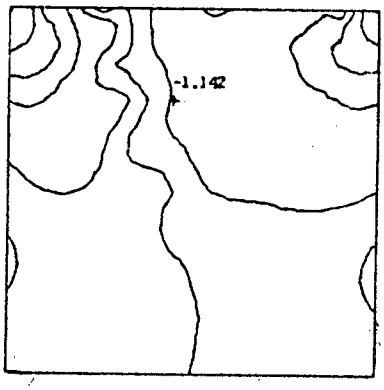

36

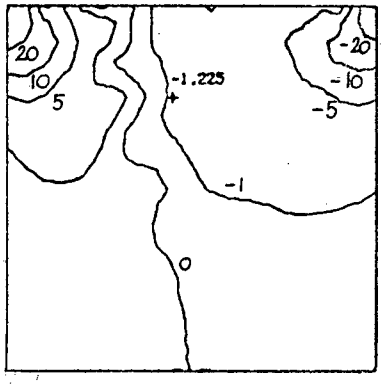

42

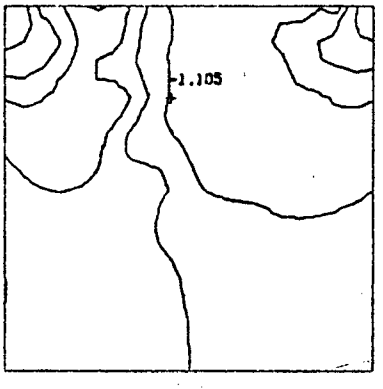

FE

(c)

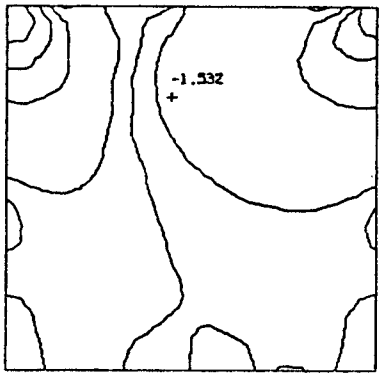

60

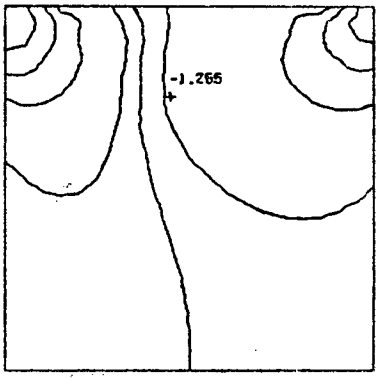

FE

FIGURE 11-3 R = 20

(a)

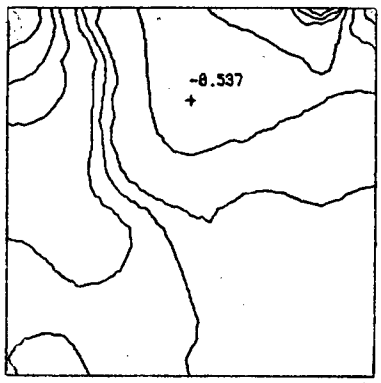

11

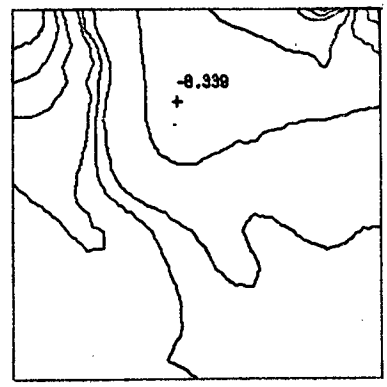

15

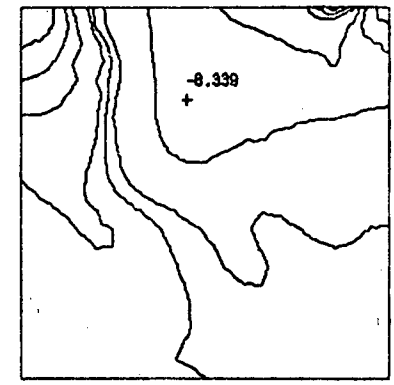

FE

(b)

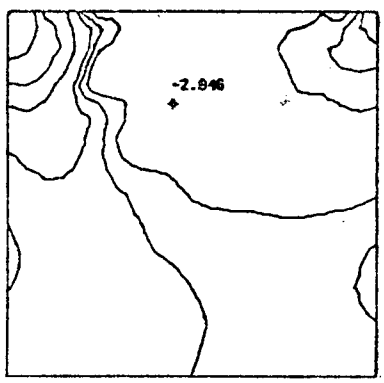

36

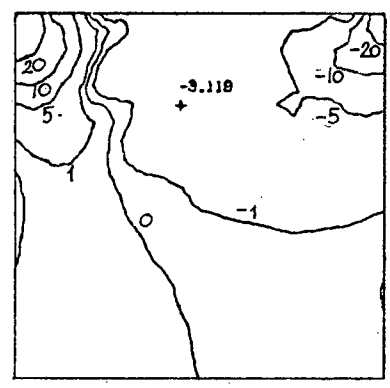

42

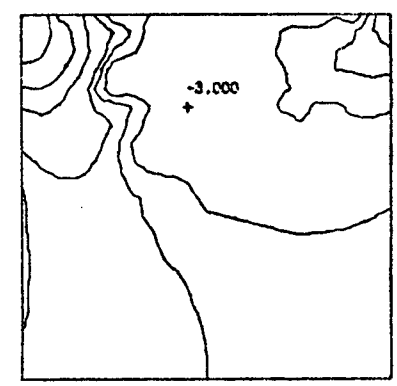

FE

(c)

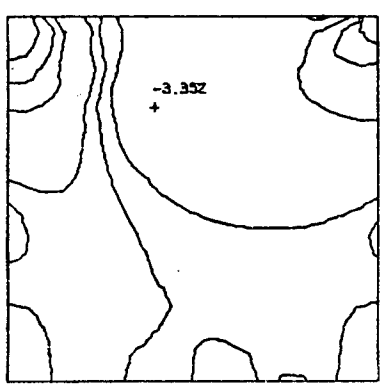

60

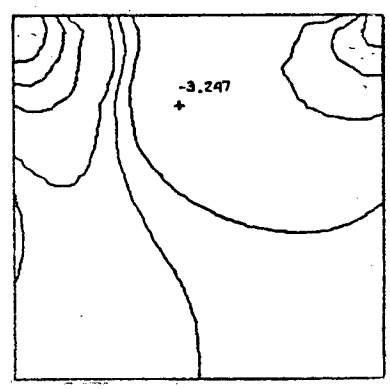

FE

FIGURE 11-4 R = 40

(a)

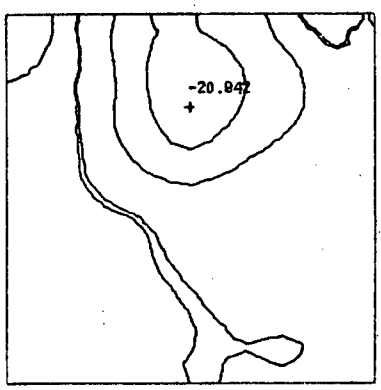

11

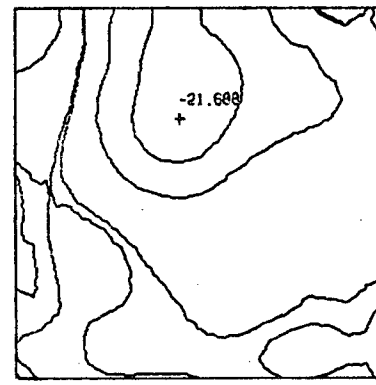

15

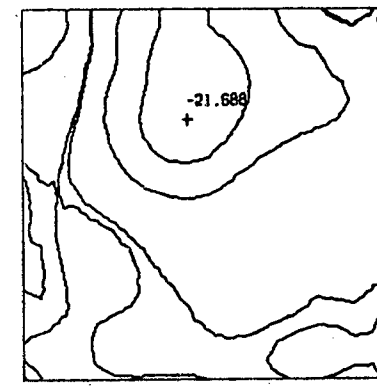

FE

(b)

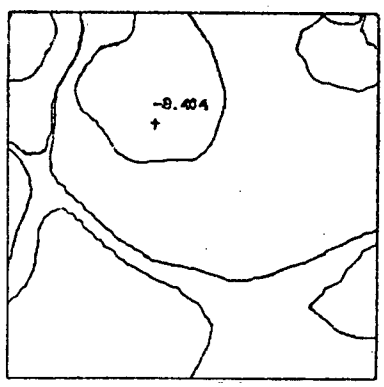

36

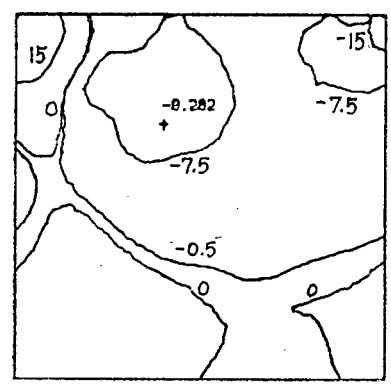

42

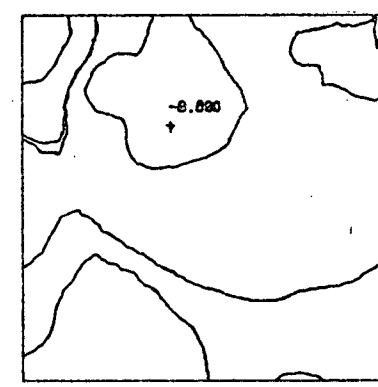

FE

(c)

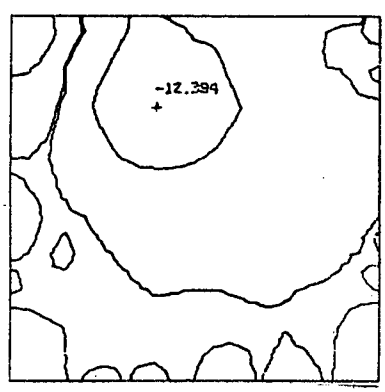

60

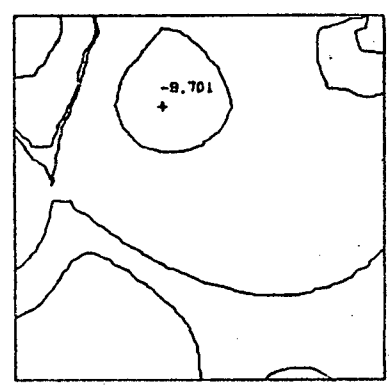

FE

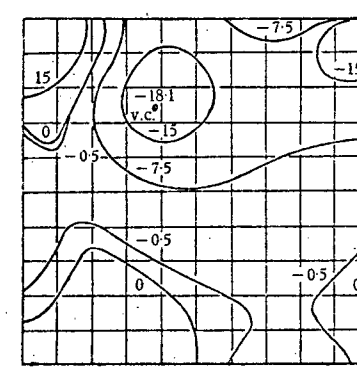

REF. 12

FIGURE 11 - 5 R = 100

(a)

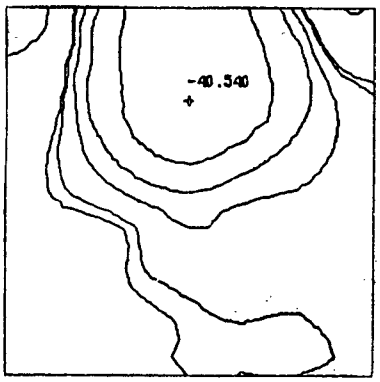

11

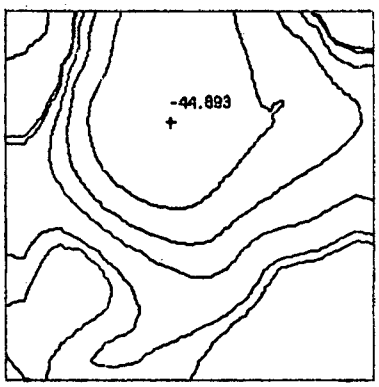

15

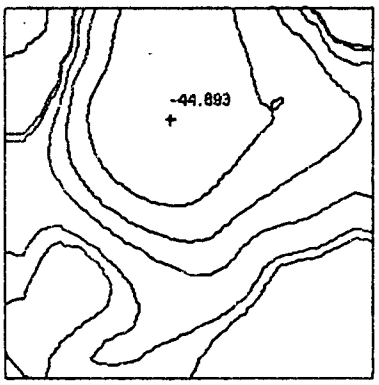

FE

(b)

36

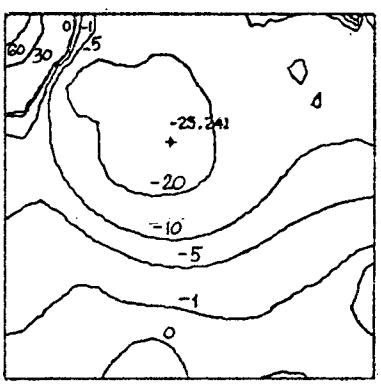

42

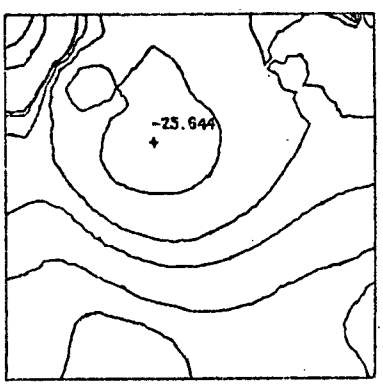

FE

(c)

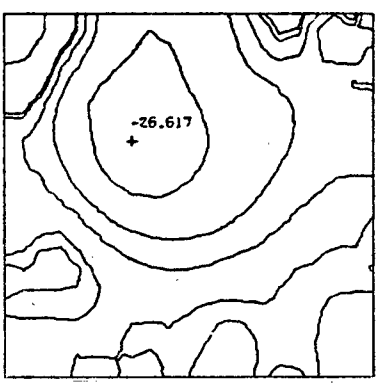

60

FIGURE 11 - 6 R = 200

(a)

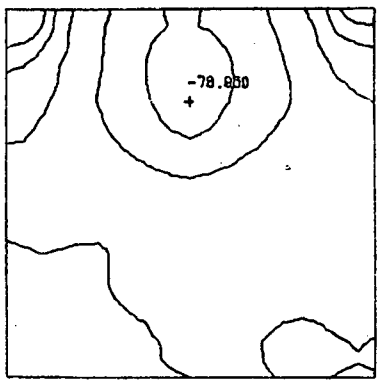

11

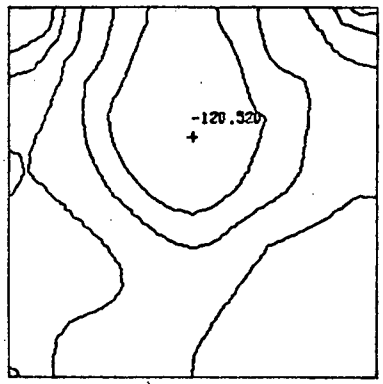

15

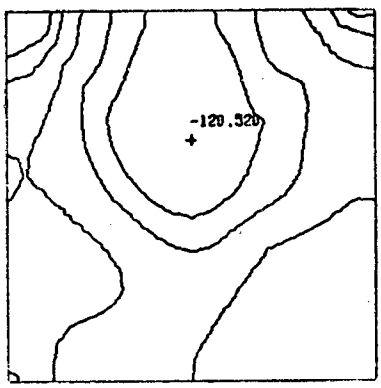

FE

(b)

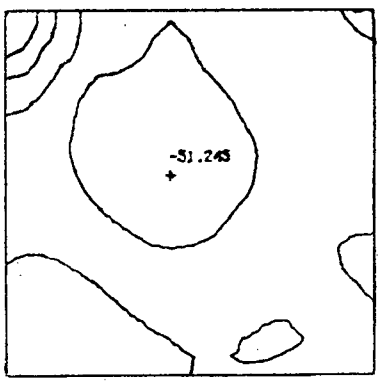

36

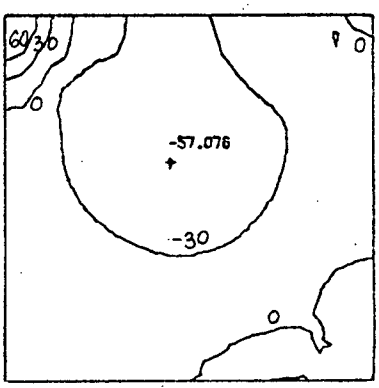

42

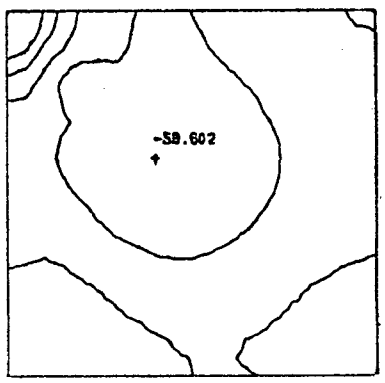

FE

(c)

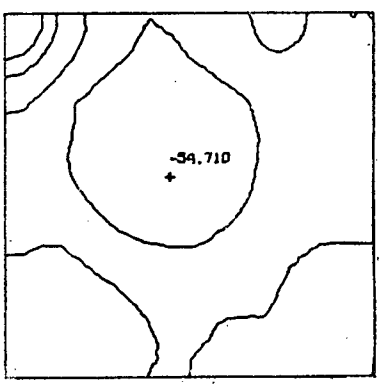

60

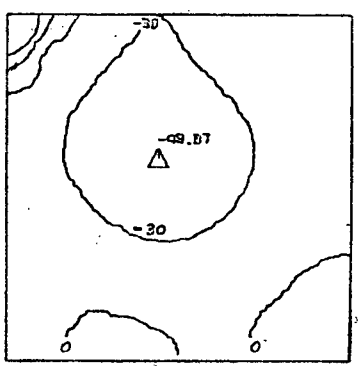

REF. 5

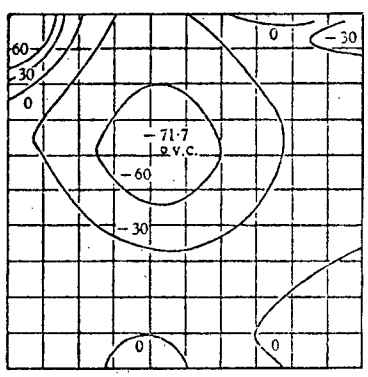

REF. 12

FIGURE 11-7 R = 400

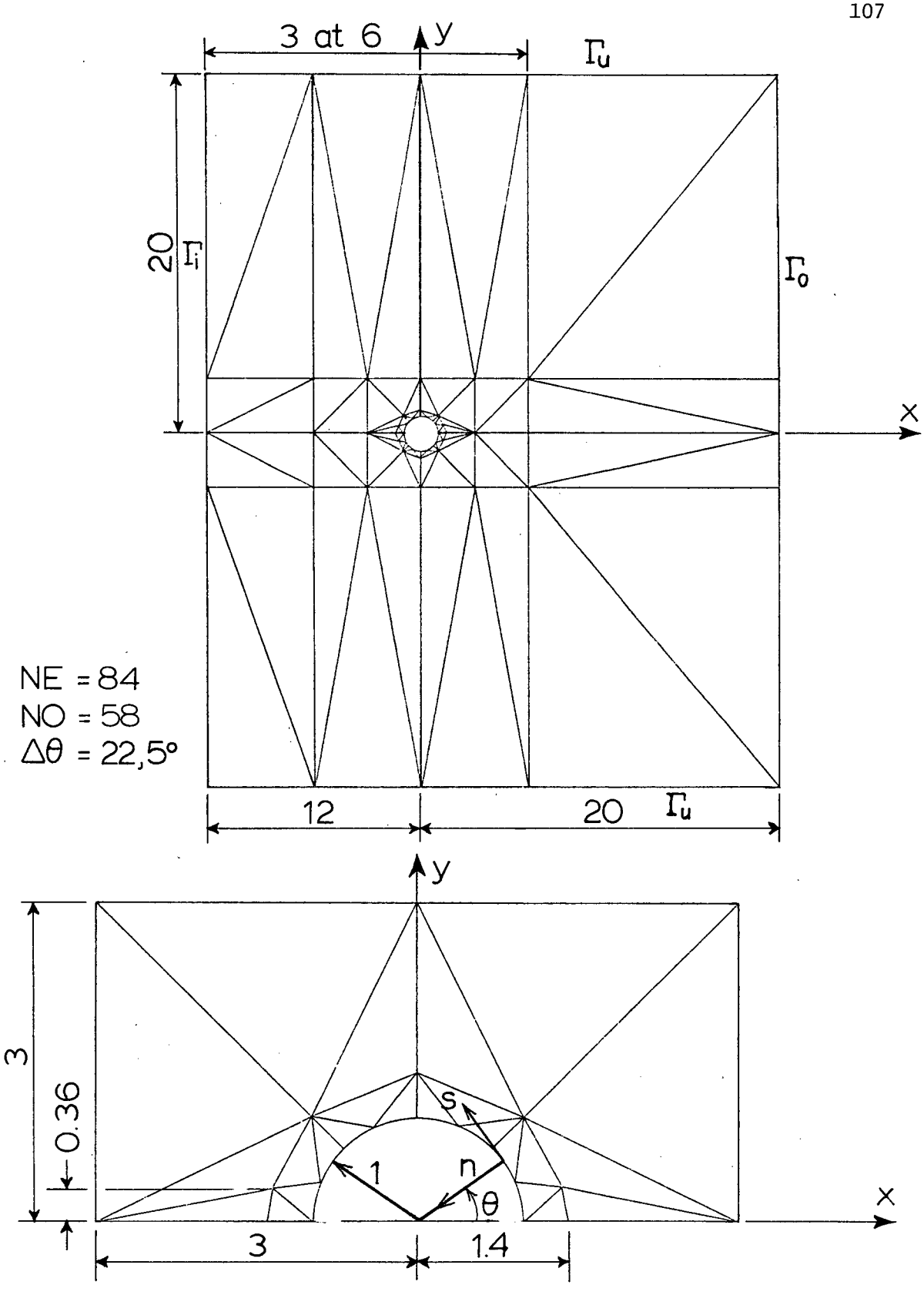

FIGURE 12-1 FINITE ELEMENT GRIDS FOR A FLOW AROUND A CIRCULAR CYLINDER CYLFL 84-58 GRID

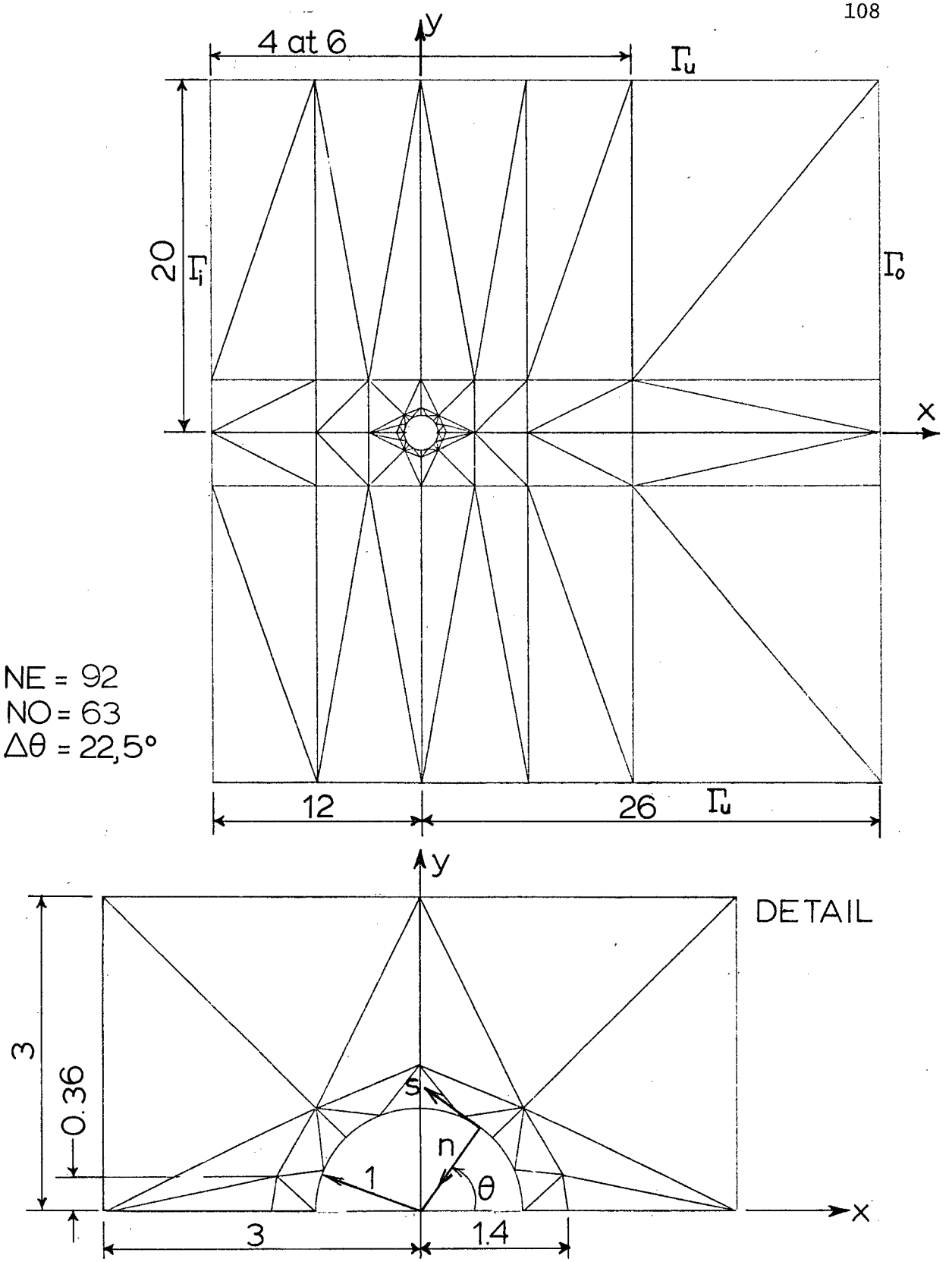

FIGURE 12-2 FINITE ELEMENT GRIDS FOR A FLOW AROUND A CIRCULAR CYLINDER CYLFL 92-63 GRID

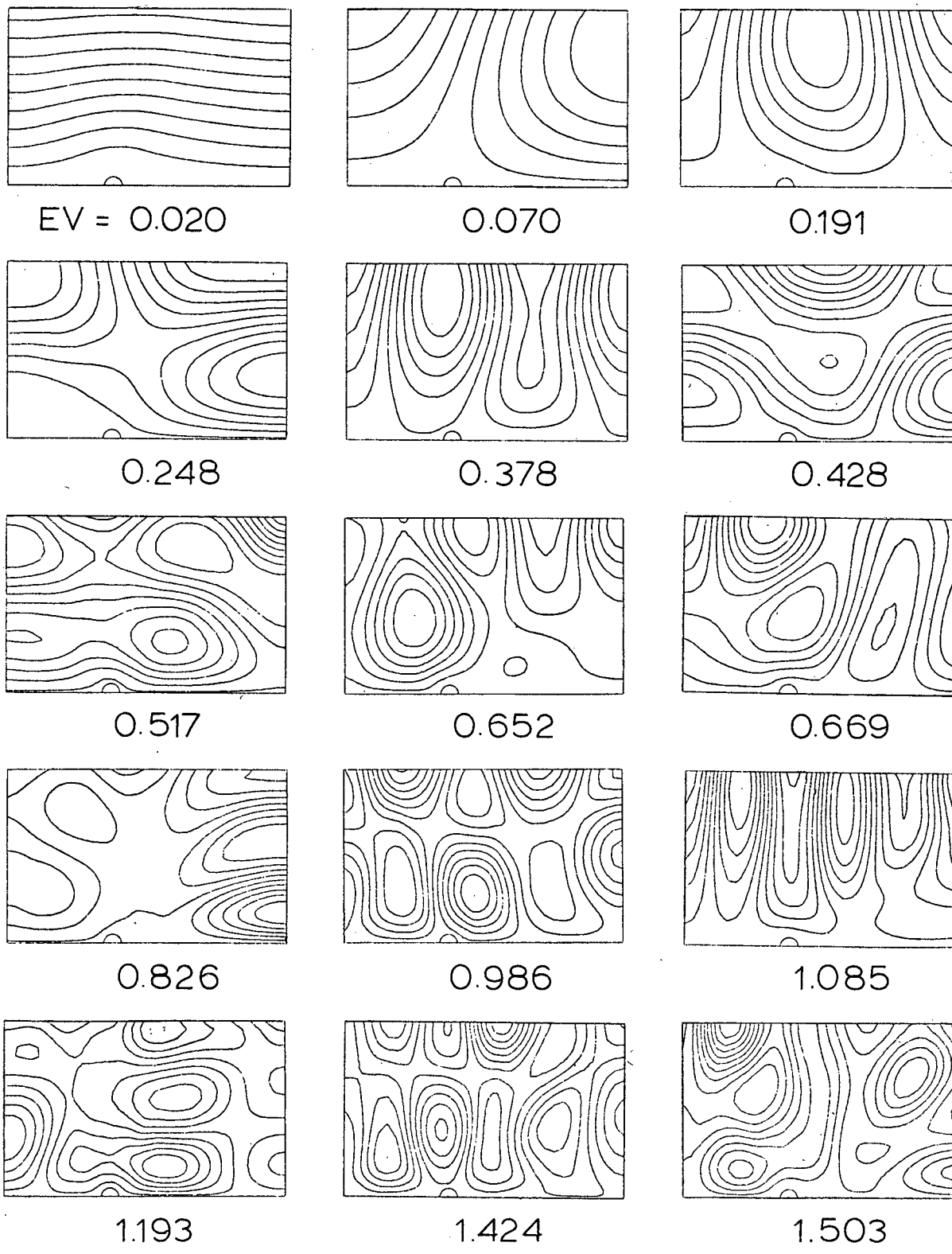

FIGURE 13-1 FIRST 15 ANTISYMMETRIC MODE SHAPES & EIGENVALUES FOR CYLFL 84-58 GRID

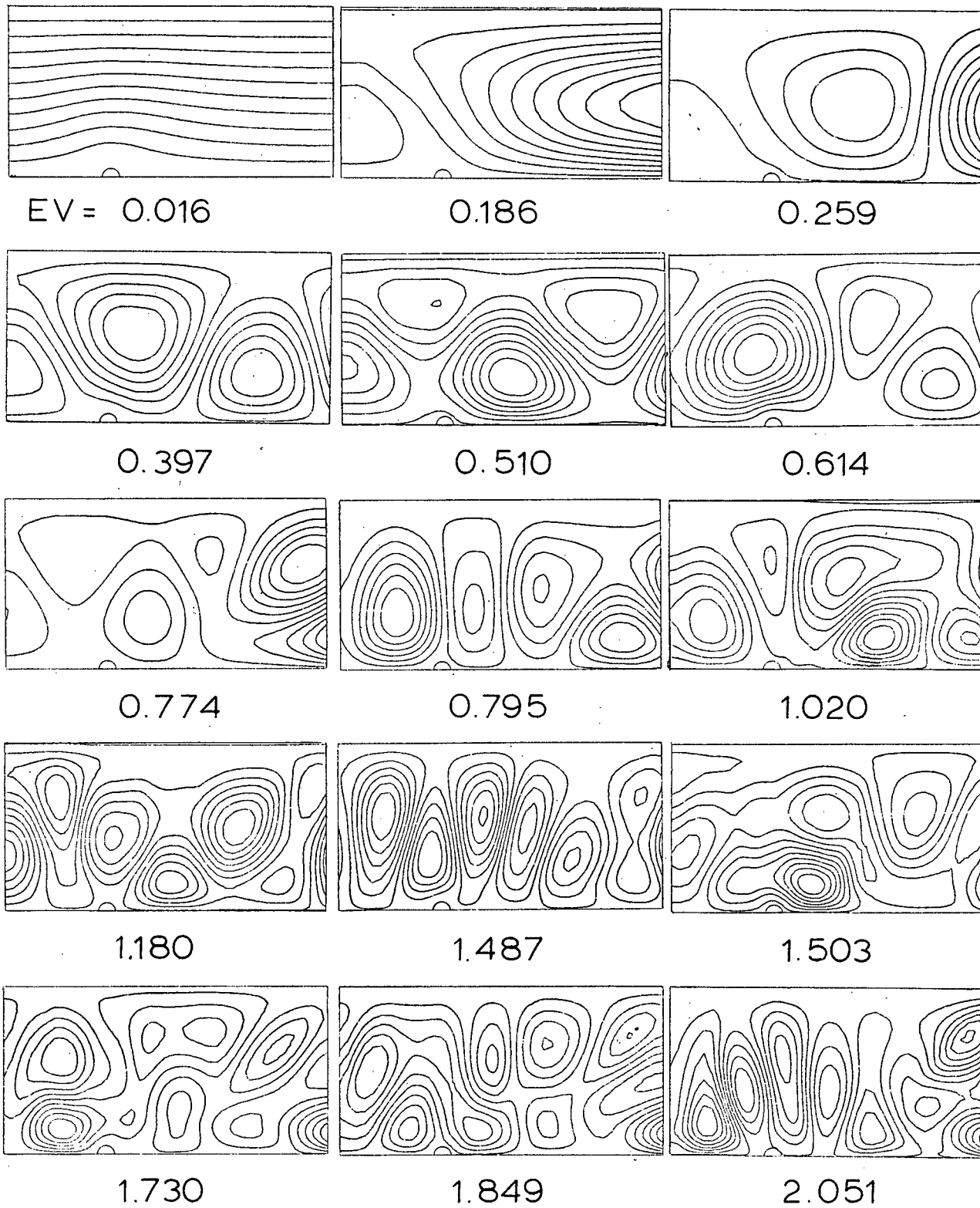

FIGURE 13-2 FIRST 20 ANTISYMMETRIC AND FIRST 10 SYMMETRIC MODE SHAPES & EIGENVALUES FOR CYLFL 92-63 GRID

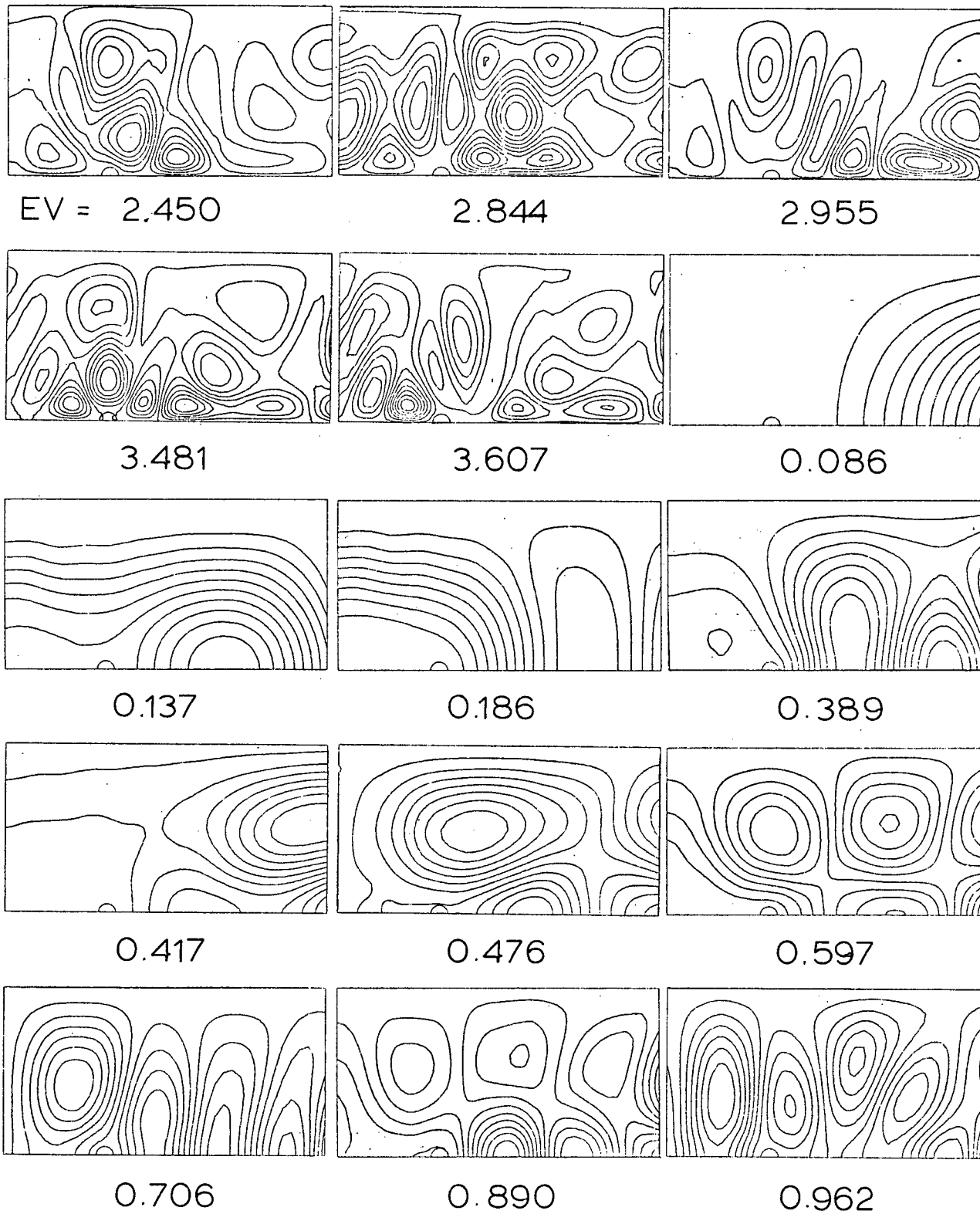

FIGURE 13-2 (CONT.) FIRST 20 ANTISYMMETRIC AND FIRST 10 SYMMETRIC MODE SHAPES & EIGENVALUES FOR CYLFL 92-63 GRID

Figure 14 Steamlines for Steady Flow Around a Circular Cylinder for Various Reynolds Numbers R

Values of the dimensionless stream function ψ are shown for each streamline on the bottom figure. Values of ψ for closed streamlines ψ_c are given below for a specified value of the Reynolds number

(4) R - 10 : ψ_c = -0.0002

(5) R = 20 : ψ_c = -0.0080, -0.0058

(6) R = 40 : ψ_c = -0.0328, -0.0246, -0.0164, -0.0082

(7) R = 70 : ψ_c = -0.07, -0.06, -0.035, -0.023

(8) R = 100: ψ_c = -0.1, -0.08, -0.05, -0.035

The number below the top figure denotes the number of modes used in the calculations, while Ref. 6 refers to the direct finite element approach using the same grid.

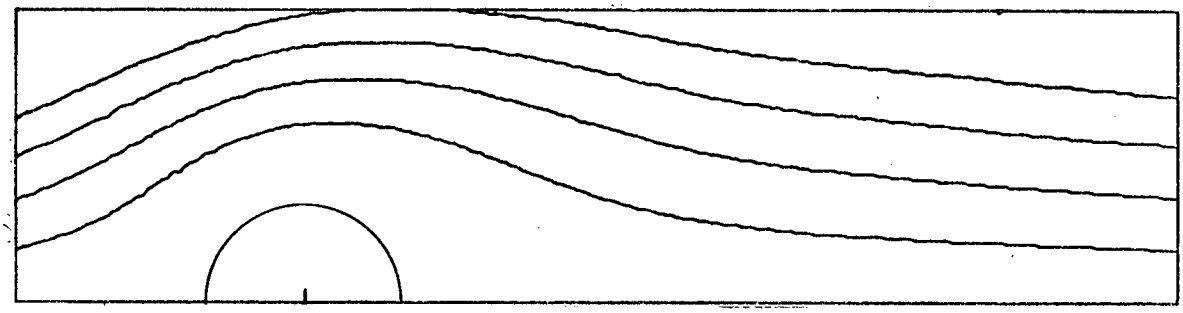

62

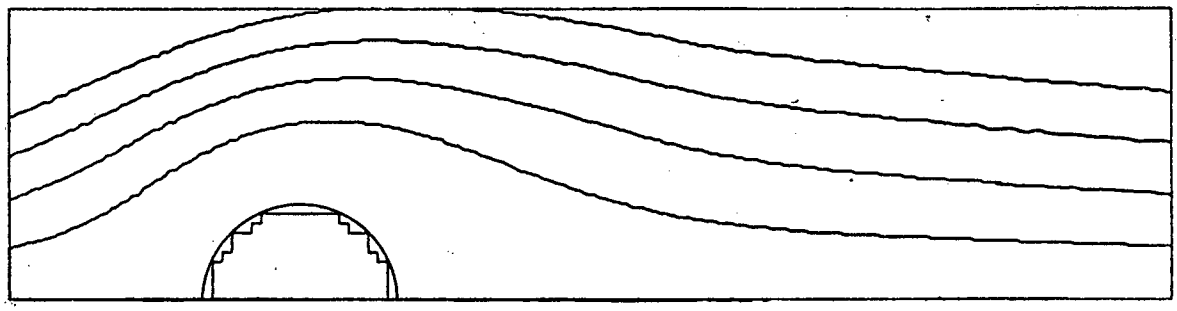

REF. 6

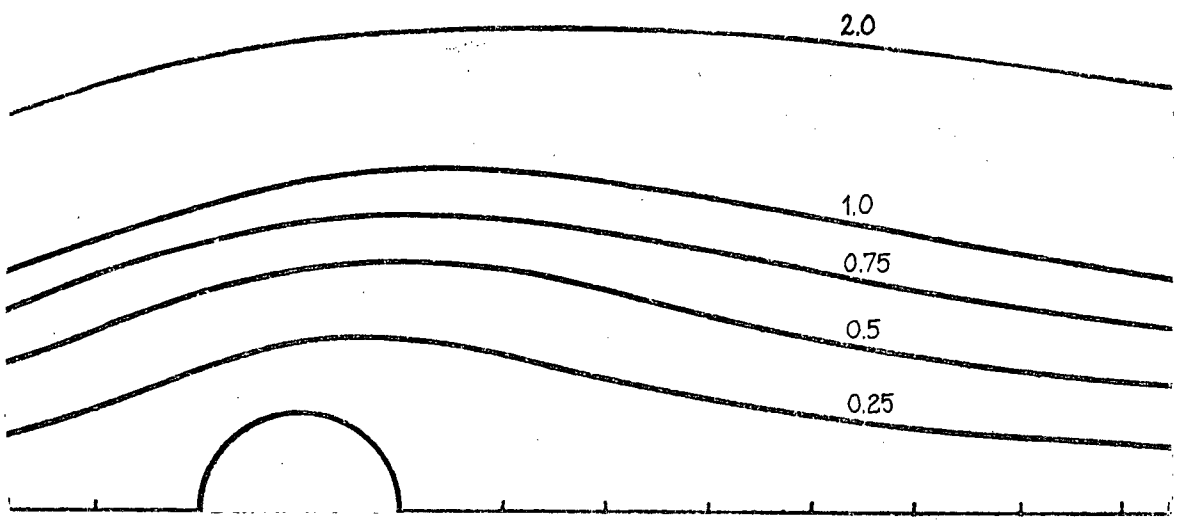

REF. 14

FIGURE 14 - 1 R = 1

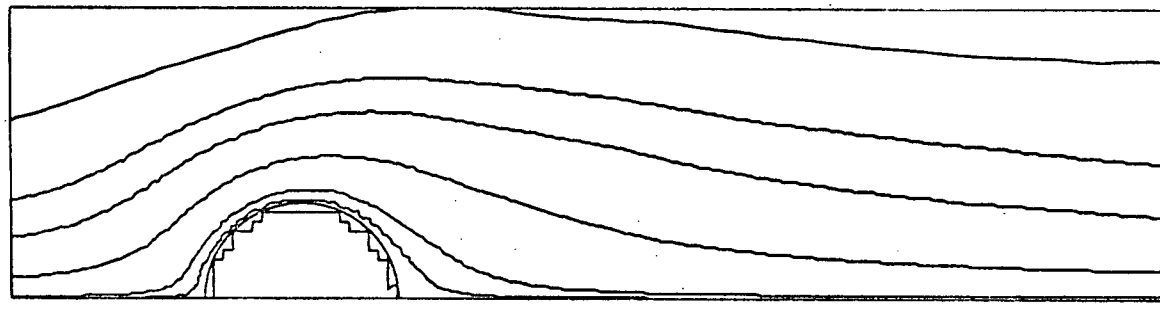

62

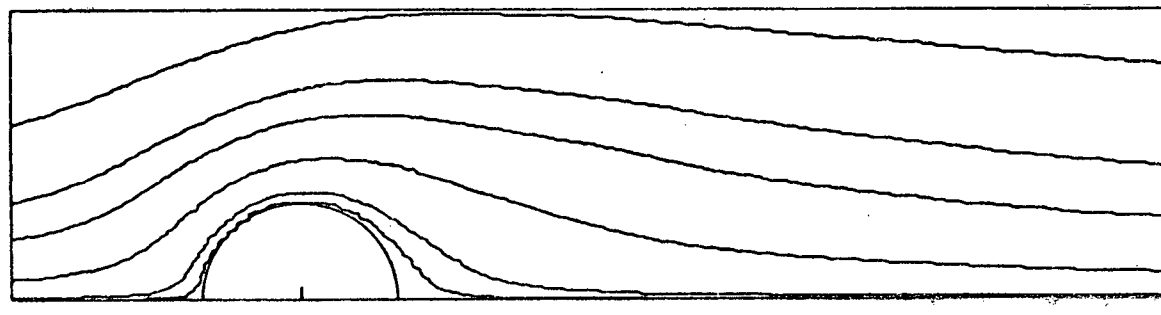

REF. 6

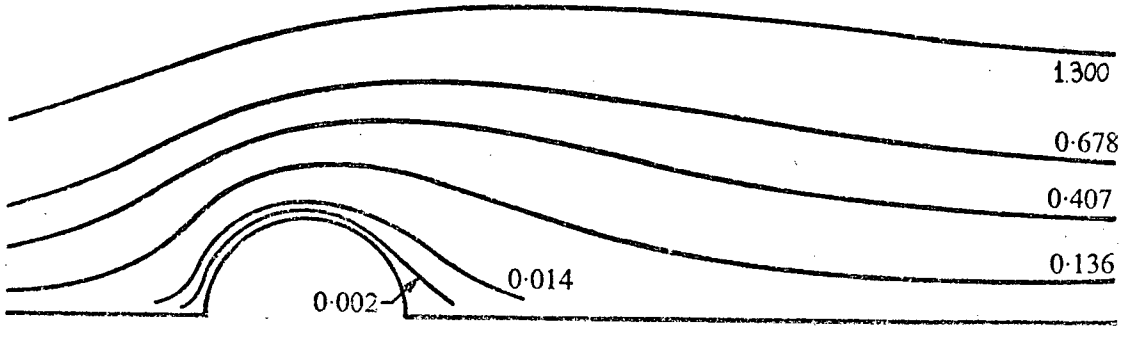

REF. 13

FIGURE 14-2 R = 5

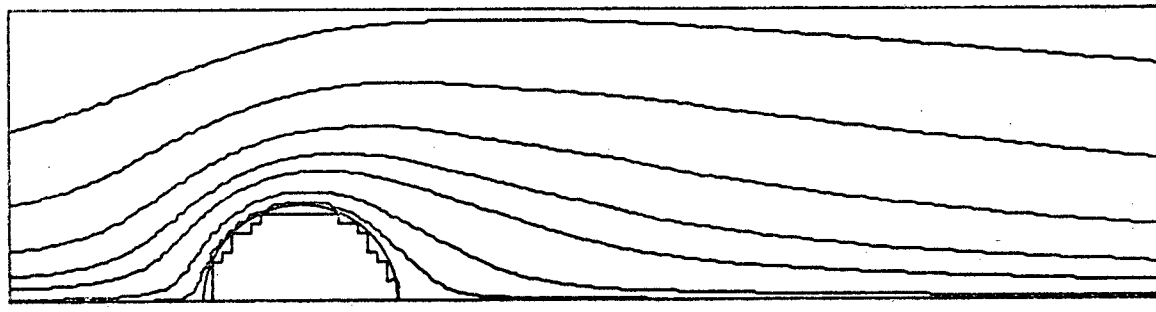

62

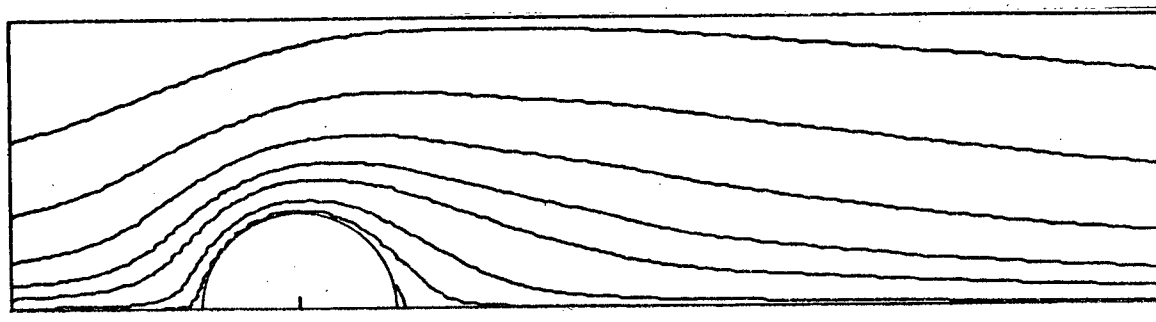

REF. 6

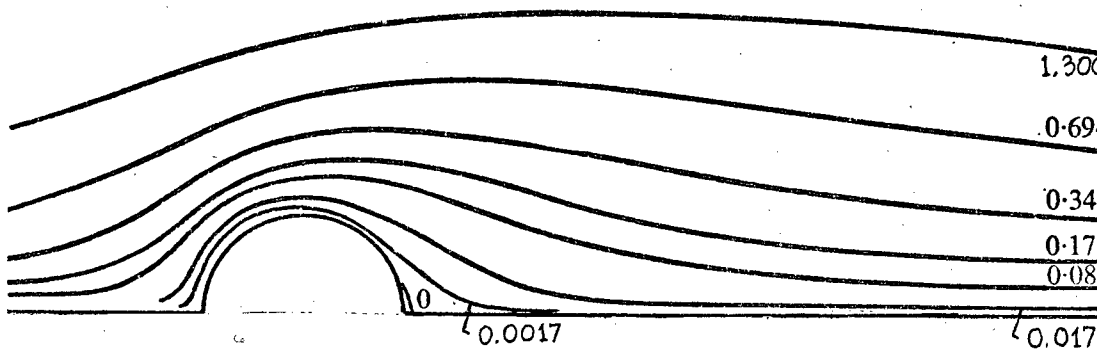

REF. 13

FIGURE 14-3 R=7

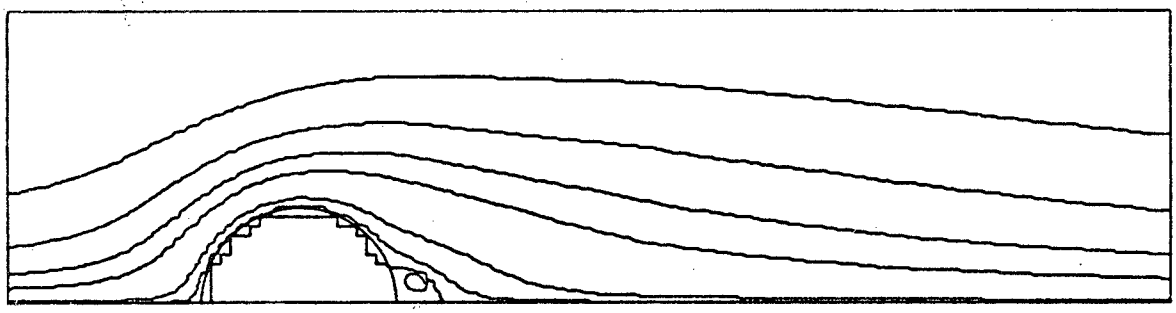

62

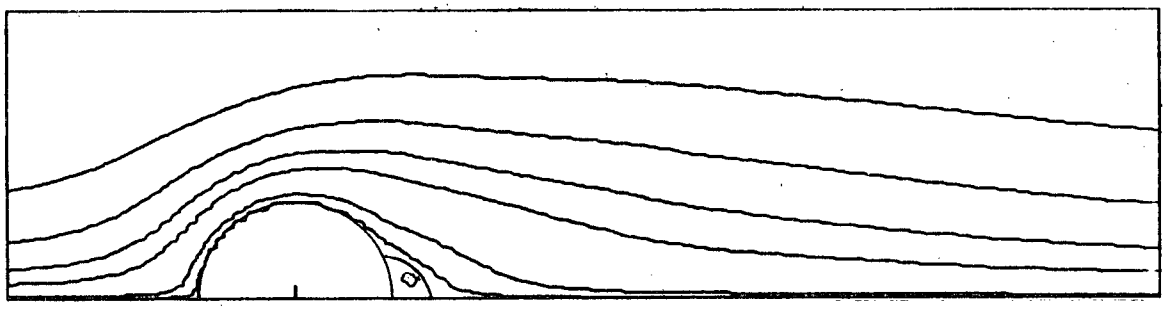

REF. 6

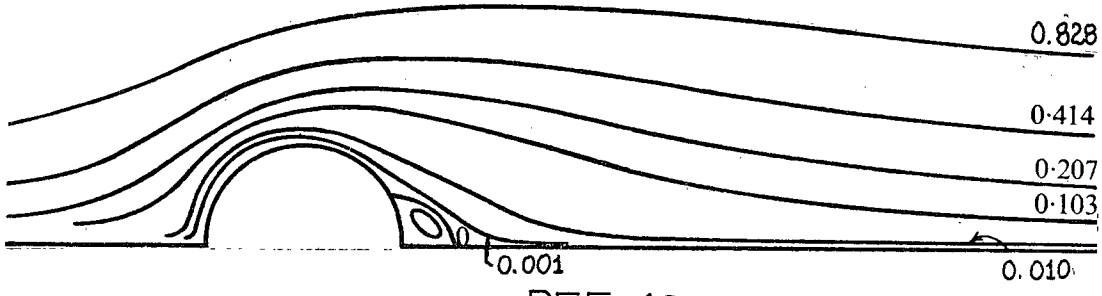

REF. 13

FIGURE 14-4 R = 10

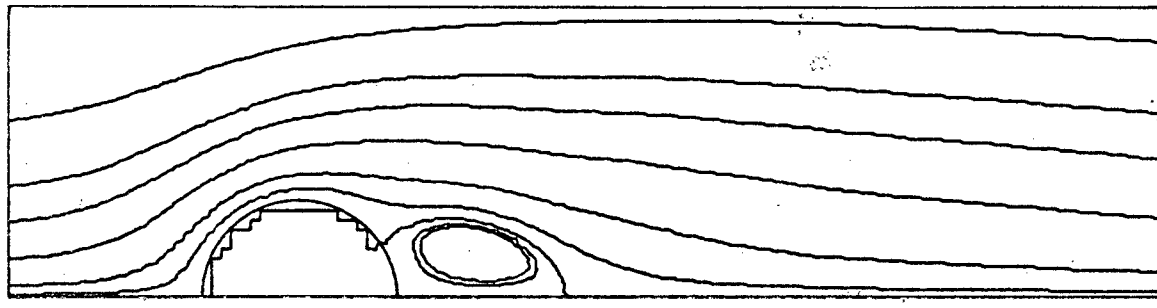

62

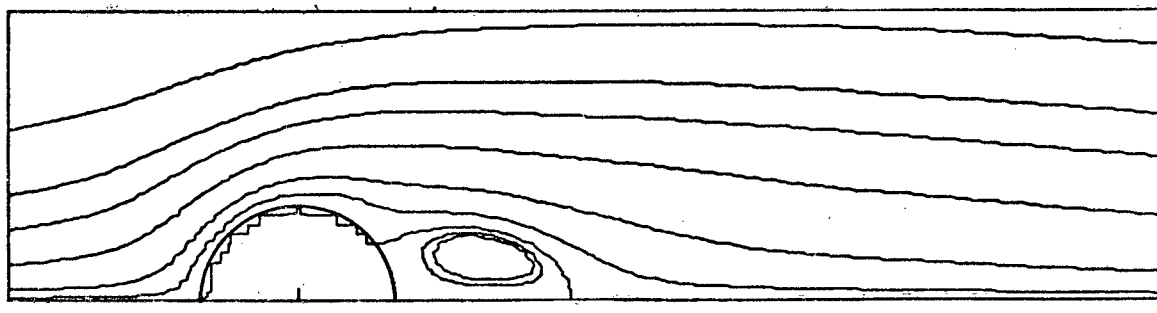

REF. 6

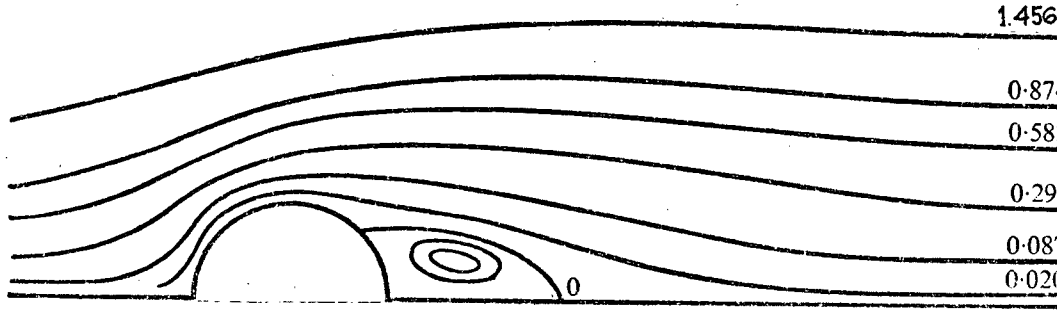

REF. 13

FIGURE 14-5 R = 20

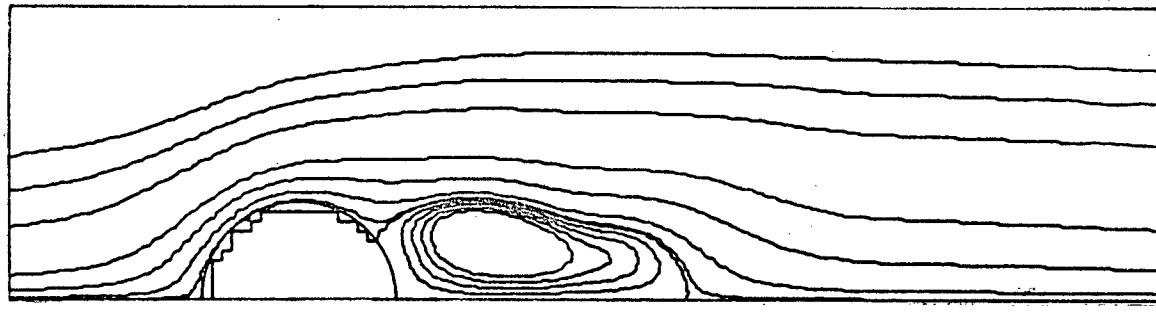

62

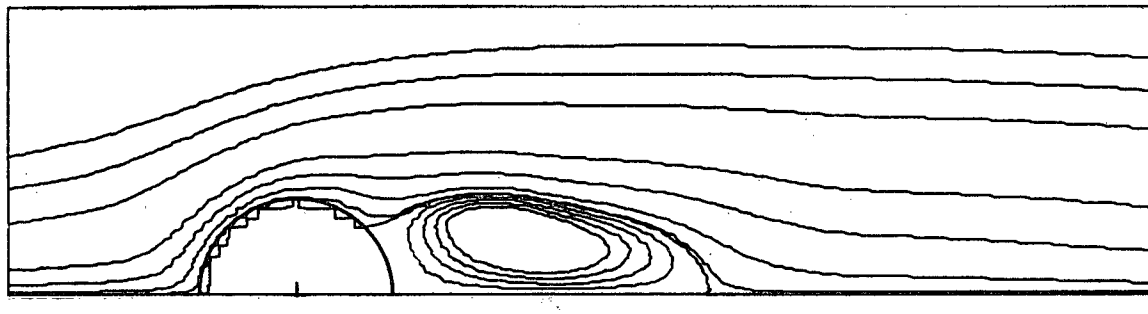

REF. 6

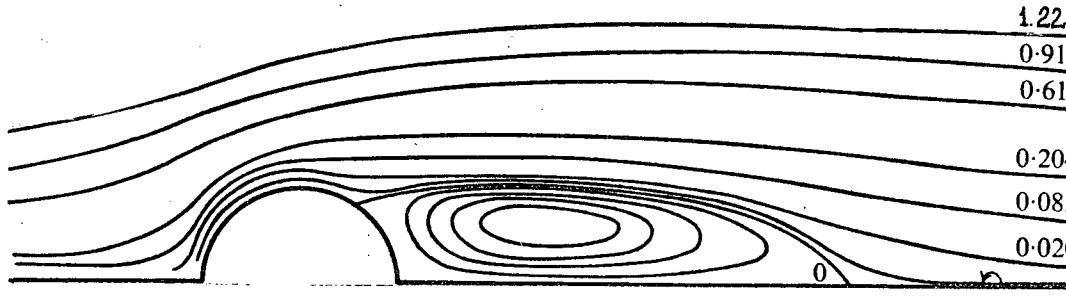

REF. 13

FIGURE 14-6 R = 40

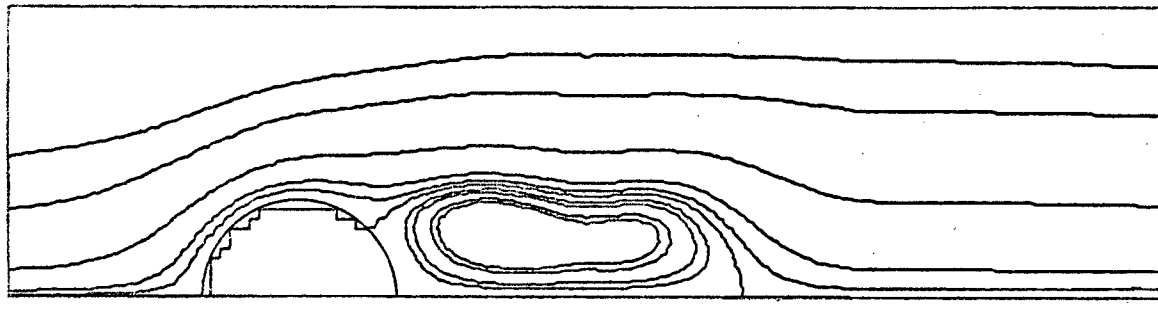

62

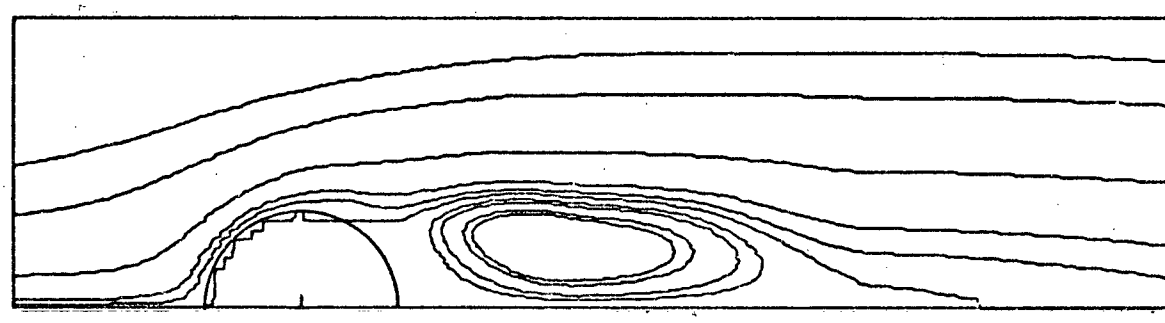

REF. 6

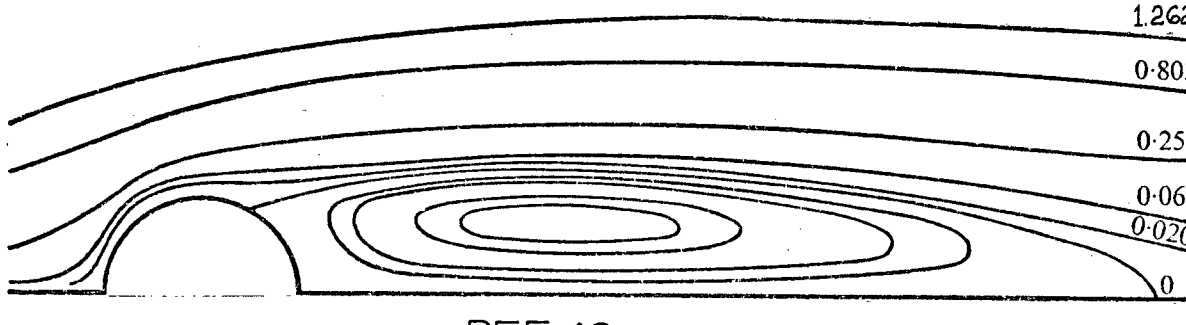

REF. 13

FIGURE 14 - 7 R = 70

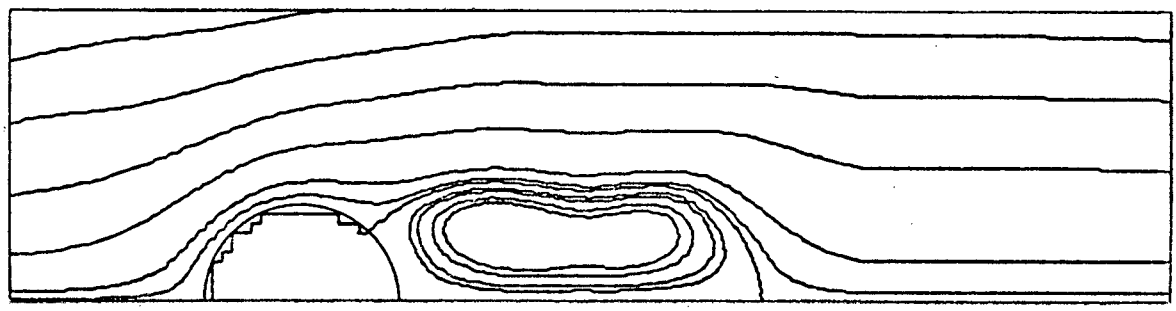

62

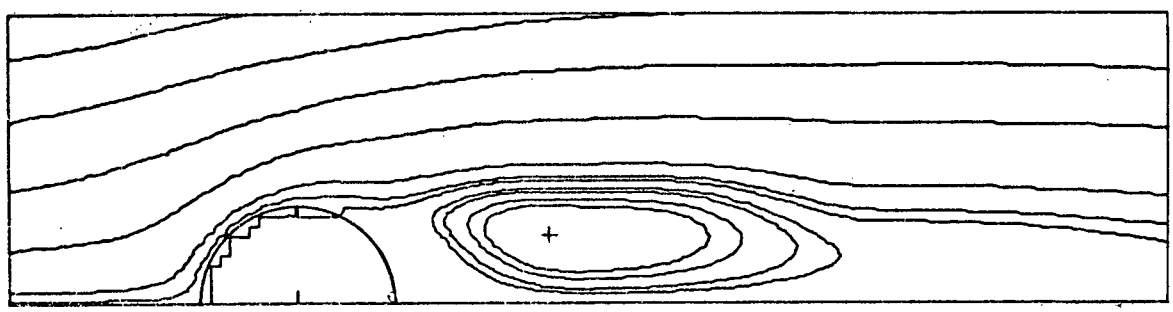

REF. 6

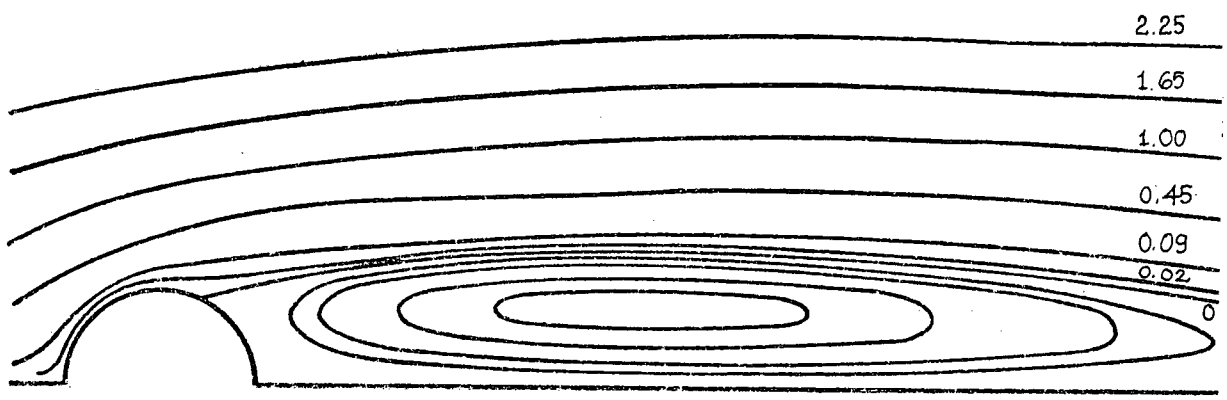

REF. 13

FIGURE 14-8 R = 100

Figure 15 Equi-Vorticity Lines for Steady Flow Around a Circular Cylinder for Various Reynolds Numbers R

Values of the negative dimensionless vorticity ζ are shown for each equi-vorticity line. The number below the top figure denotes the number of modes used in the calculations, while Ref. 6 refers to the direct finite element approach using the same grid.

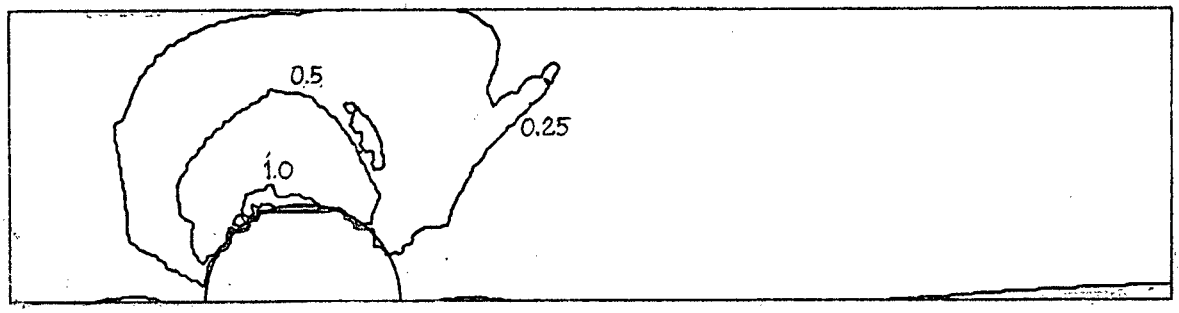

62

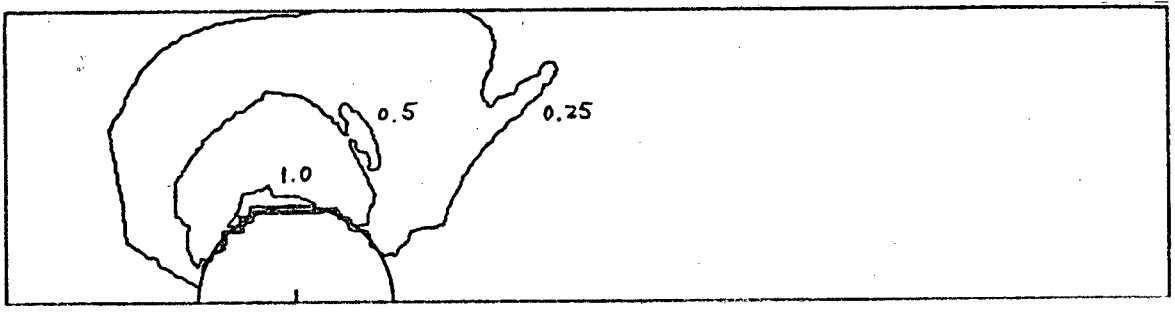

REF. 6

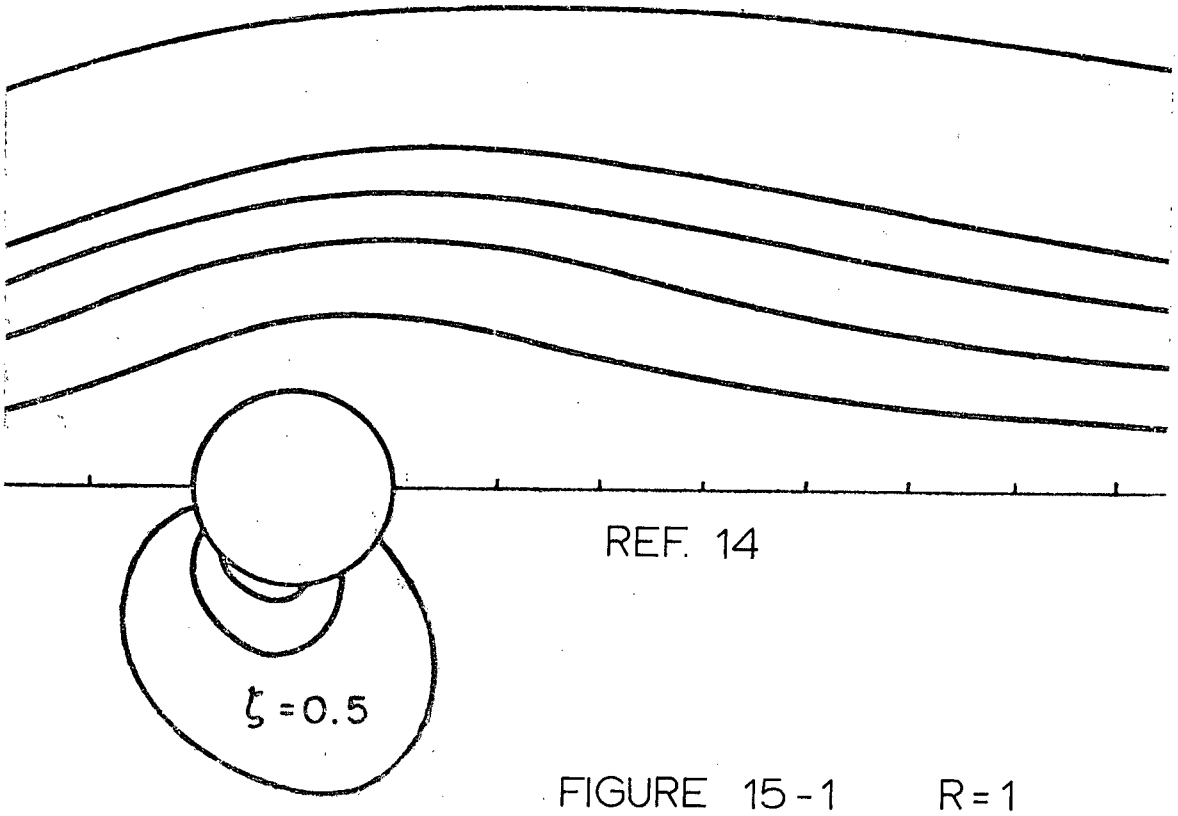

REF. 14

FIGURE 15-1 R=1

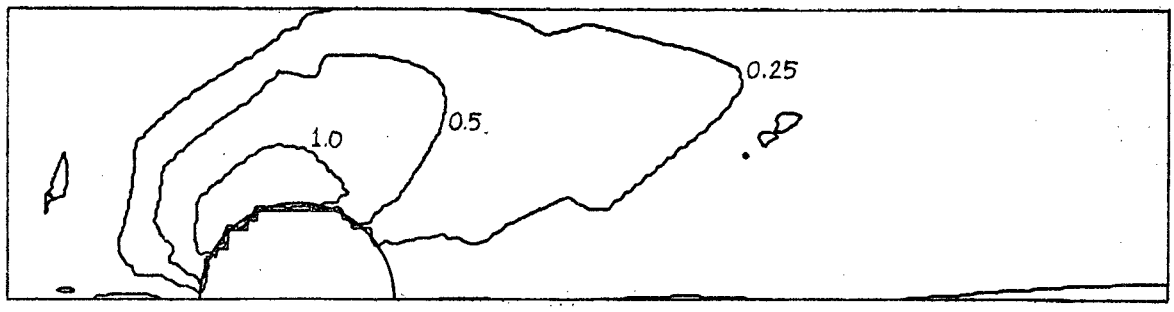

62

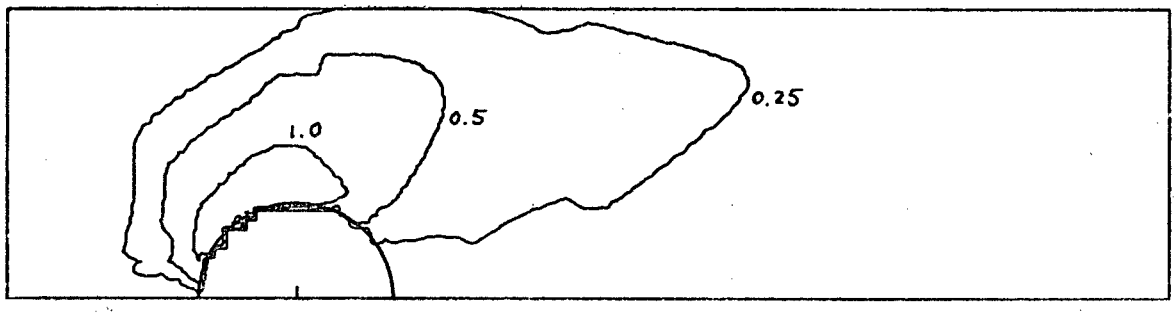

REF. 6

FIGURE 15 - 2 R = 5

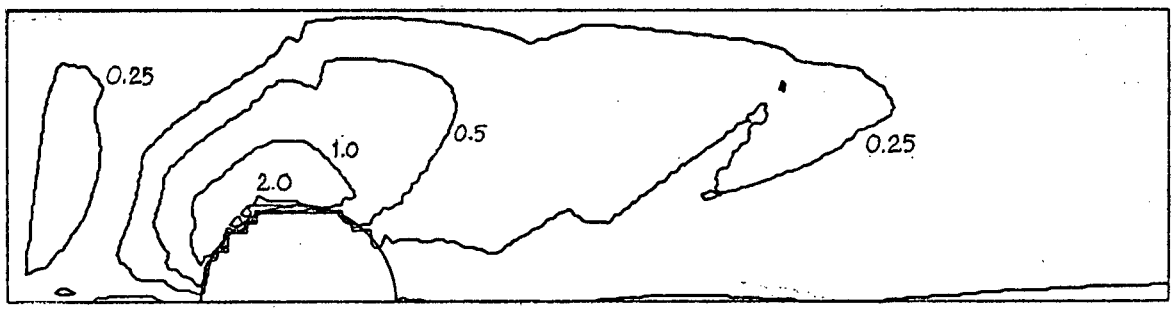

62

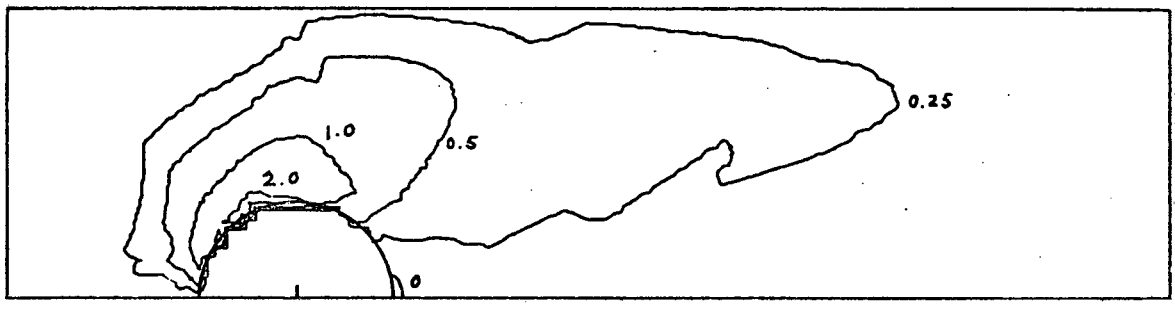

REF. 6

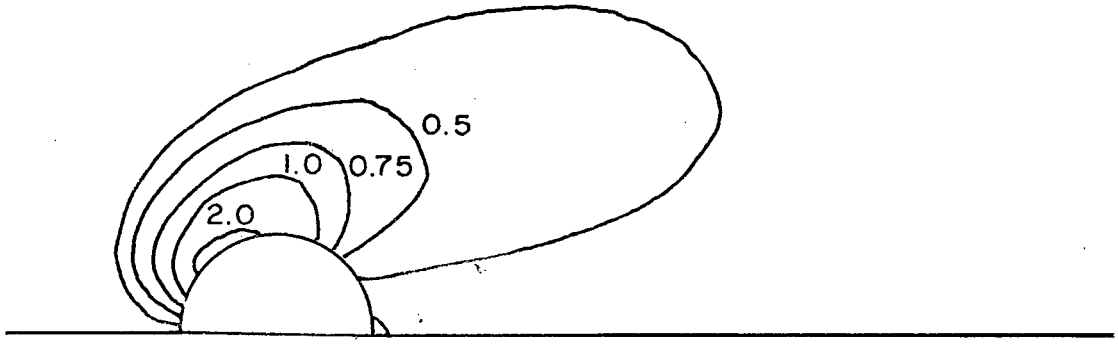

REF. 14

FIGURE 15-3 R=7

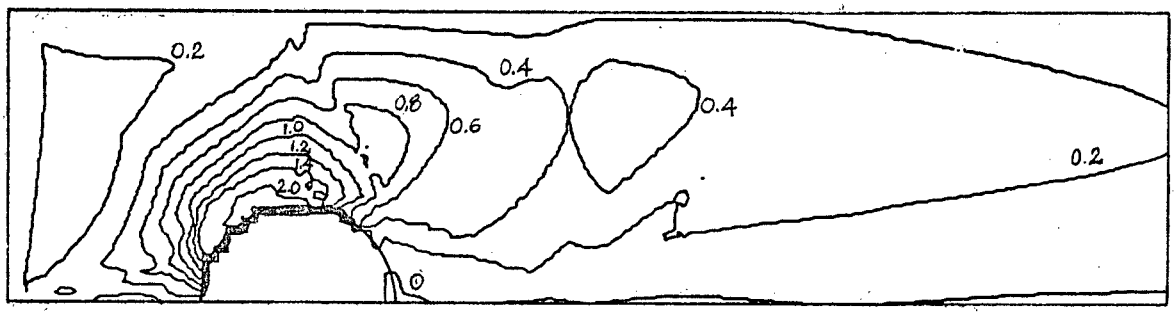

62

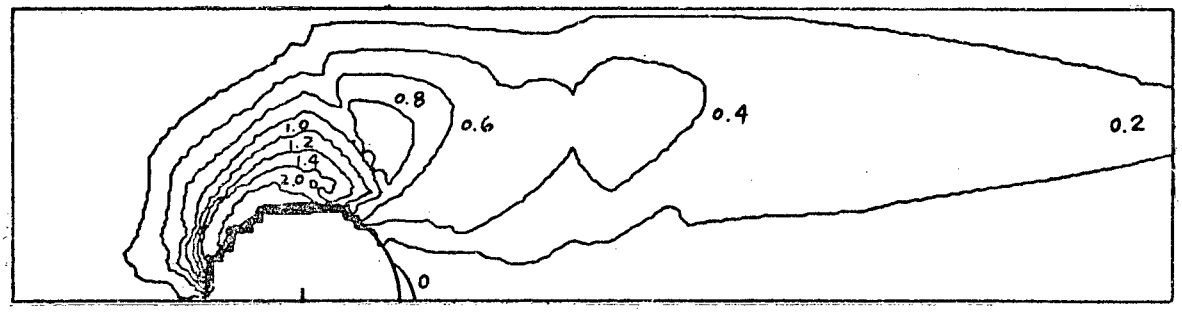

REF. 6

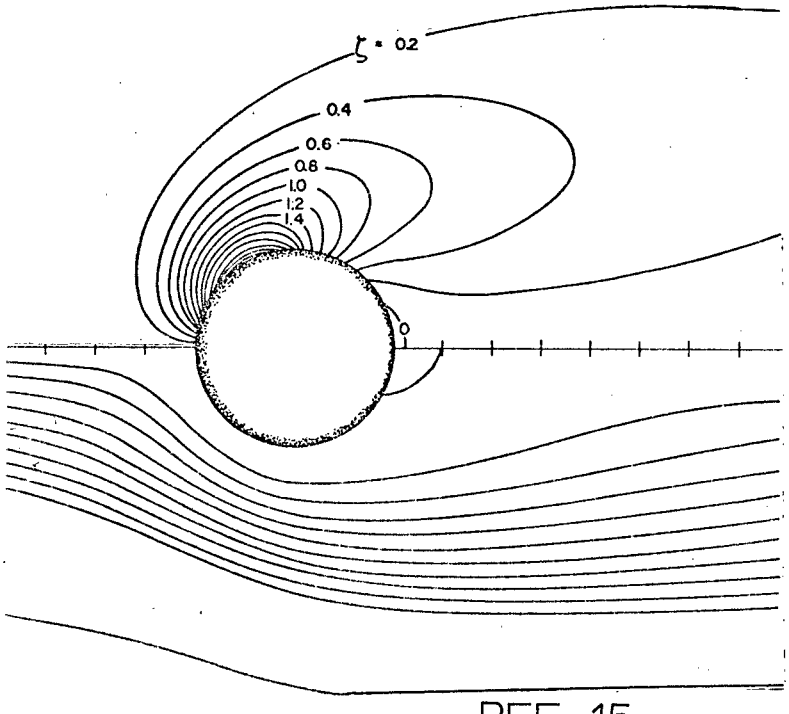

REF. 15

FIGURE 15 - 4 R = 10

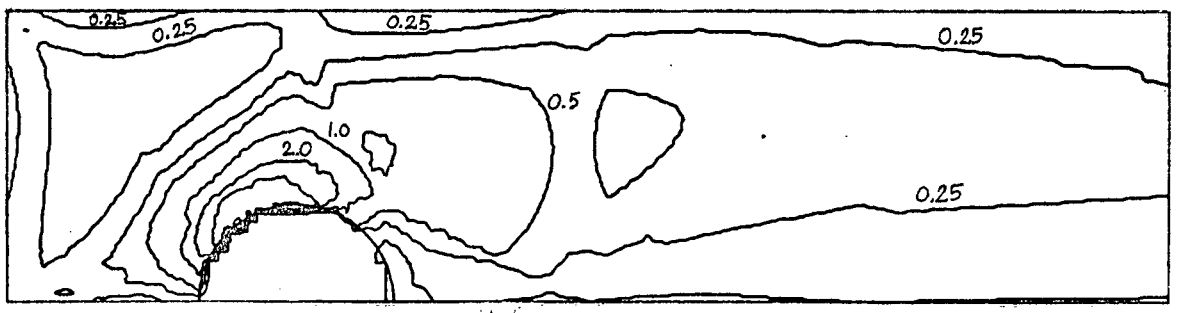

62

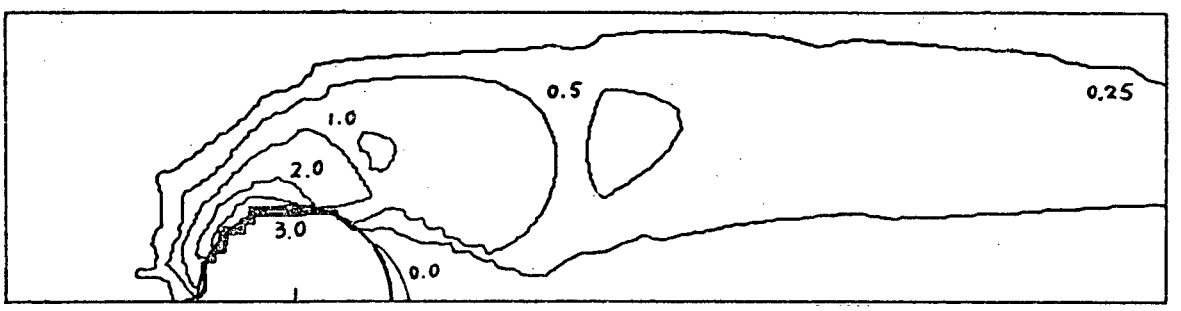

REF. 6

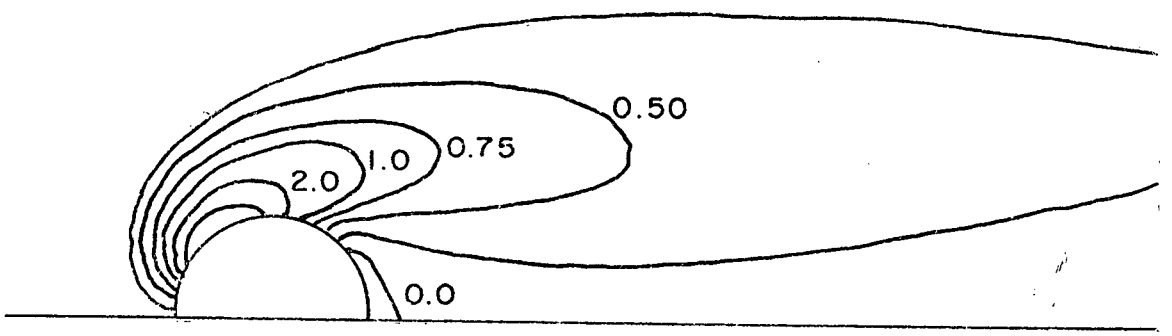

REF. 14

FIGURE 15-5 R = 20

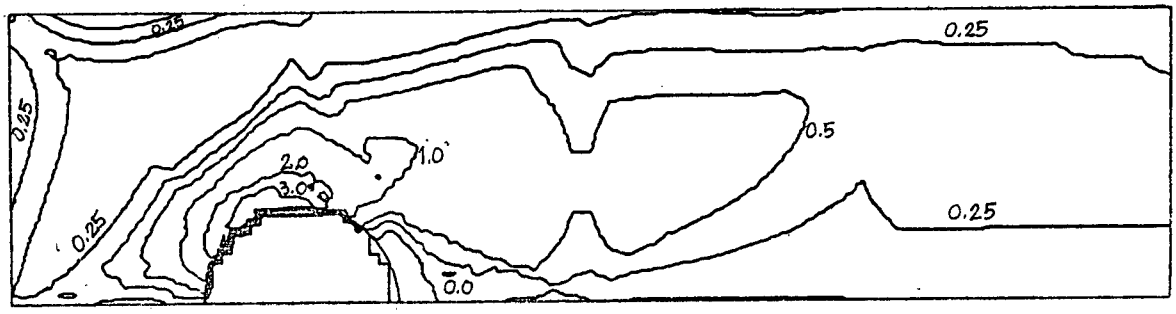

62

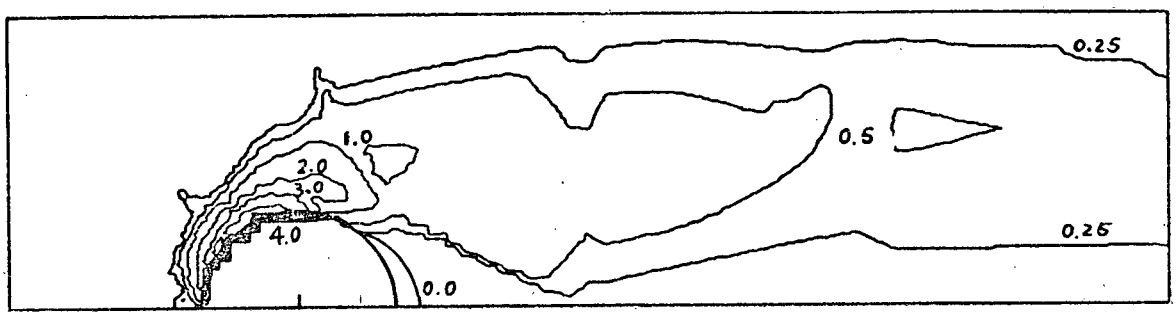

REF. 6

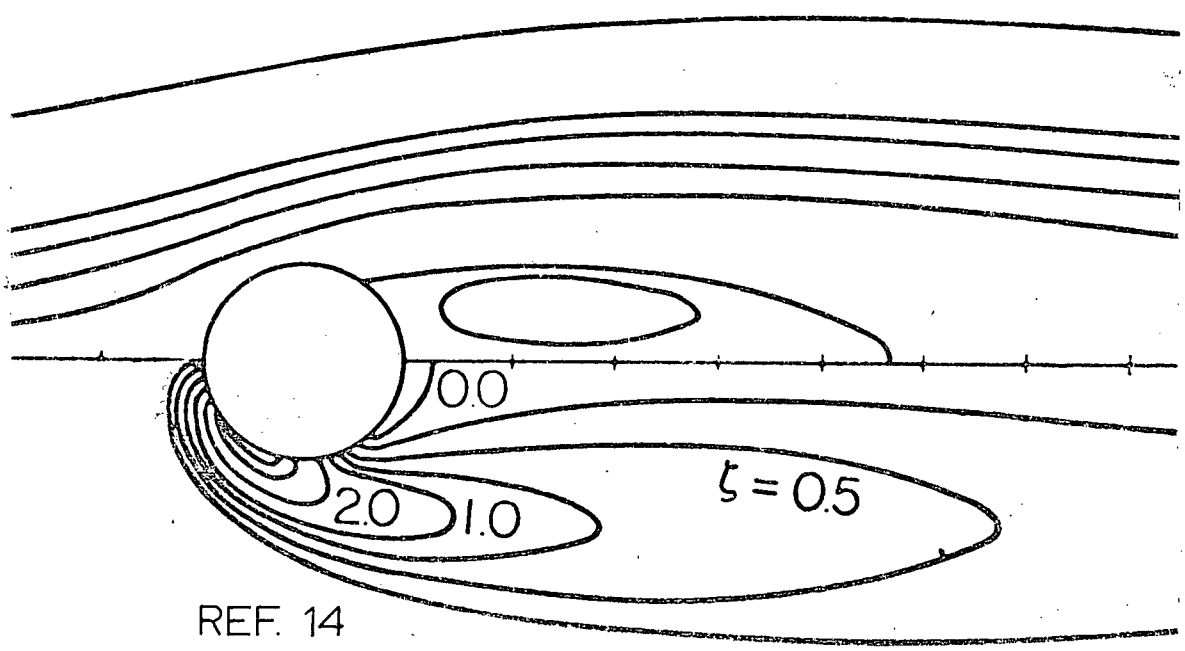

REF. 14

FIGURE 15-6 R = 40

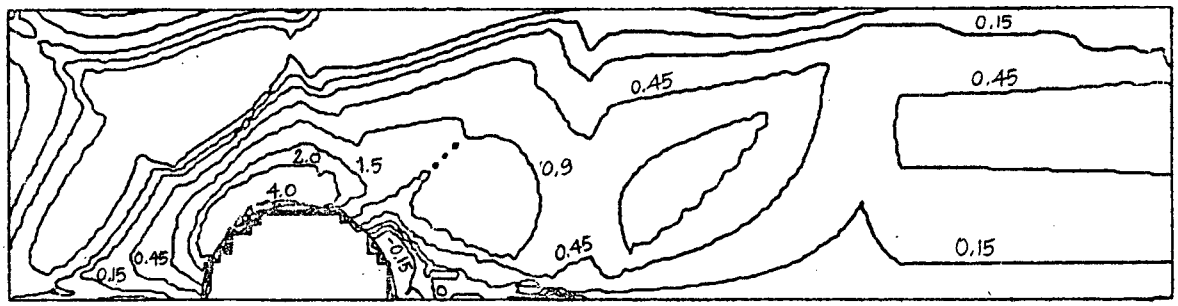

62

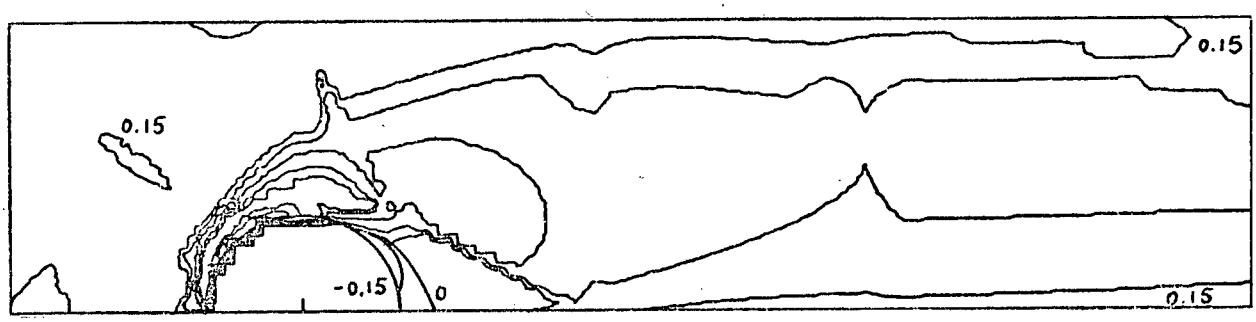

REF. 6

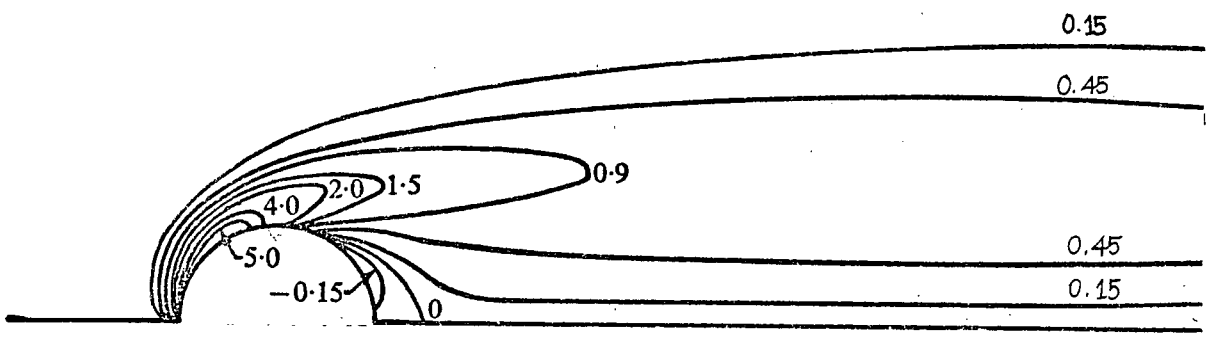

REF. 13

FIGURE 15-7 R = 70

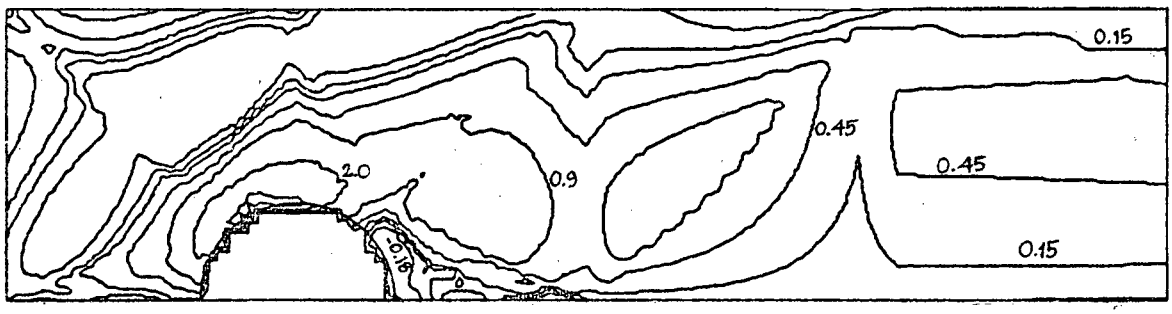

62

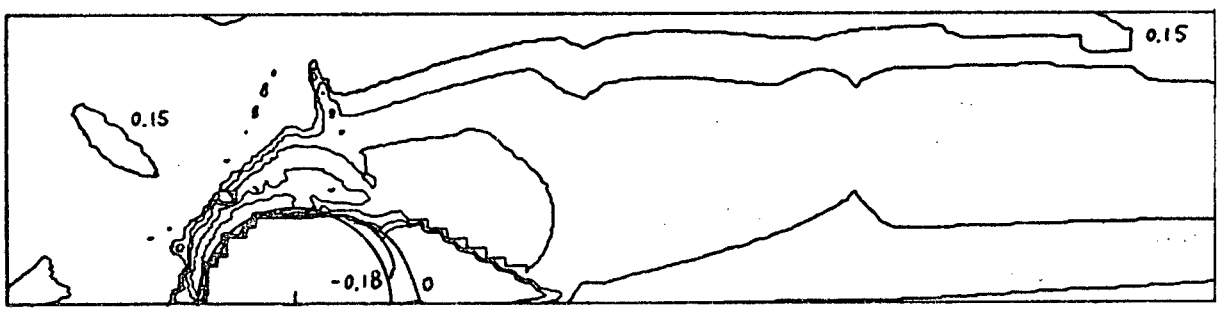

REF. 6

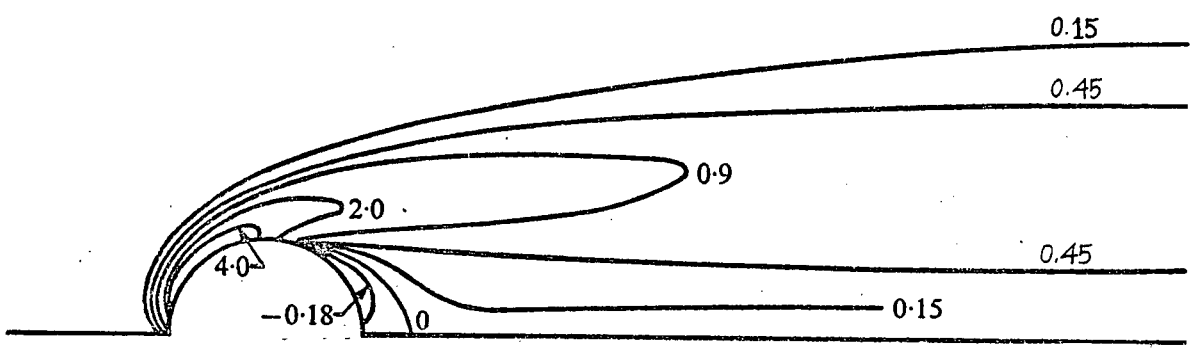

REF. 13

FIGURE 15-8 R = 100

Figure 16 Streamlines for Transient Flow Around a Circular Cylinder at Reynolds Number IT=140 for Various Time Instants

The following streamlines are plotted

ψ = -0.631, -0.4115, -0.129, -0.03, -0.0175, -0.0115

0.0, 0.0115, 0.0175, 0.03, 0.129, 0.4115, and 0.631

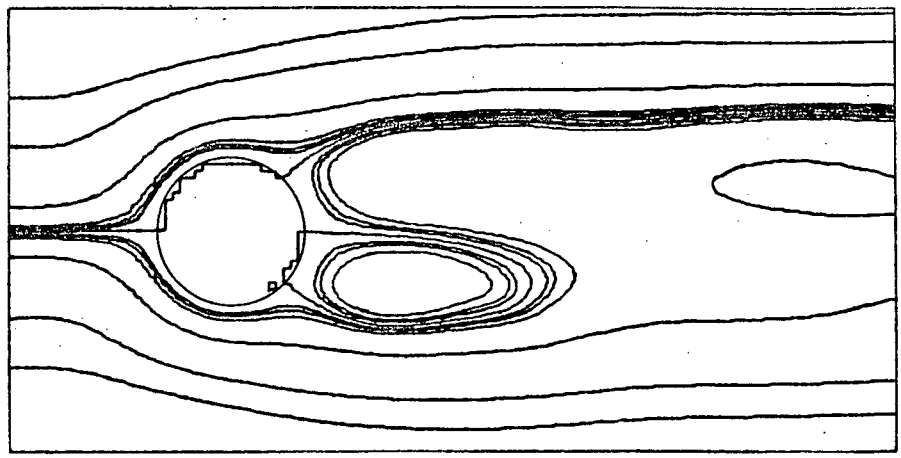

T = 3 SECONDS

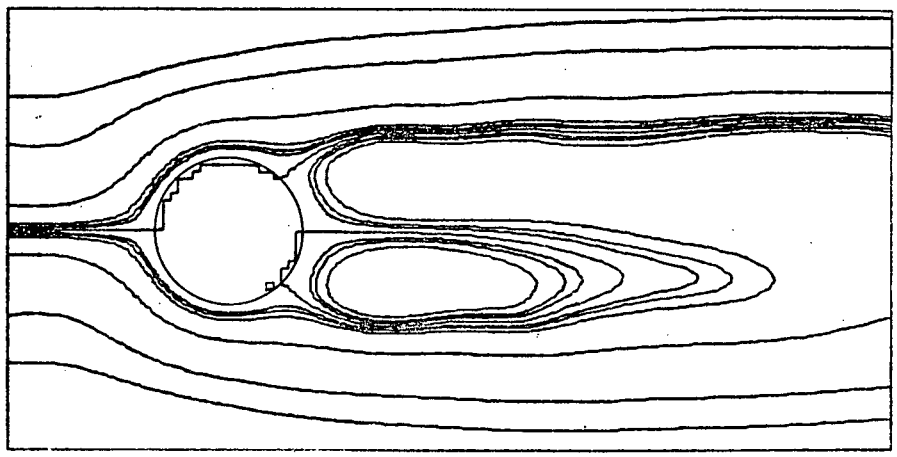

T = 6 SECONDS

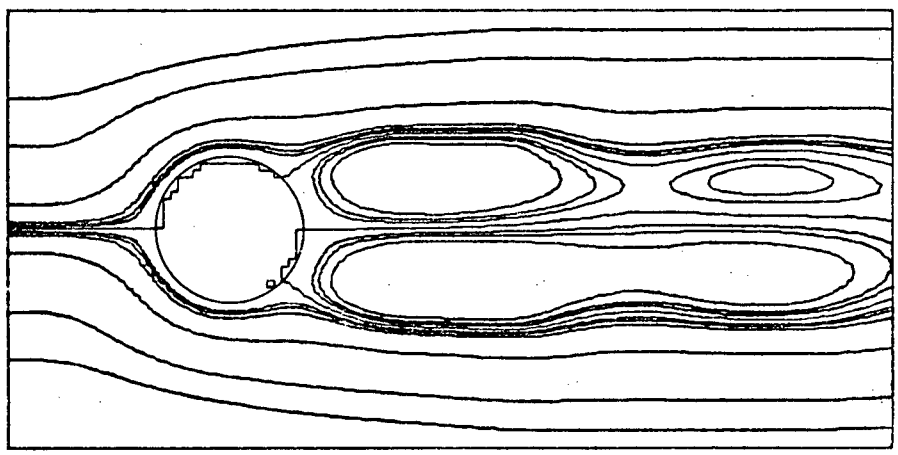

T = 9 SECONDS

FIGURE 16 STREAMLINES FOR TRANSIENT FLOW AROUND A CIRCULAR CYLINDER AT REYNOLDS NO. R = 140 FOR VARIOUS TIME INSTANTS

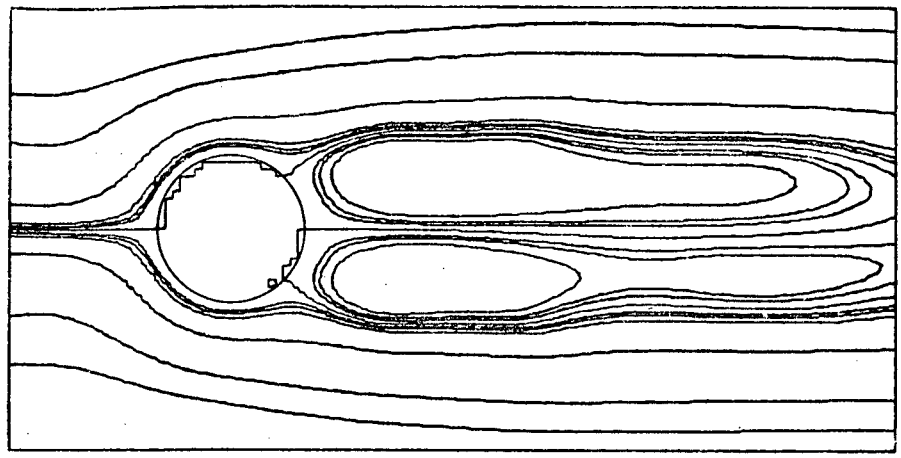

T = 12 SECONDS

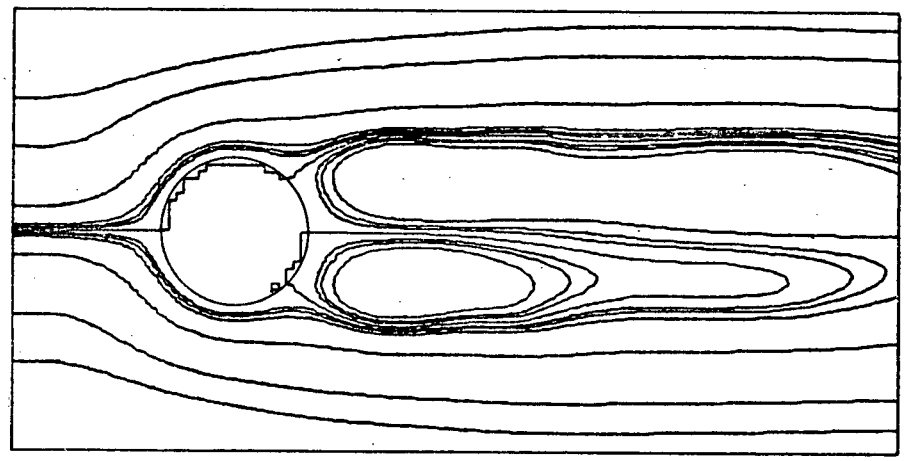

T = 15 SECONDS

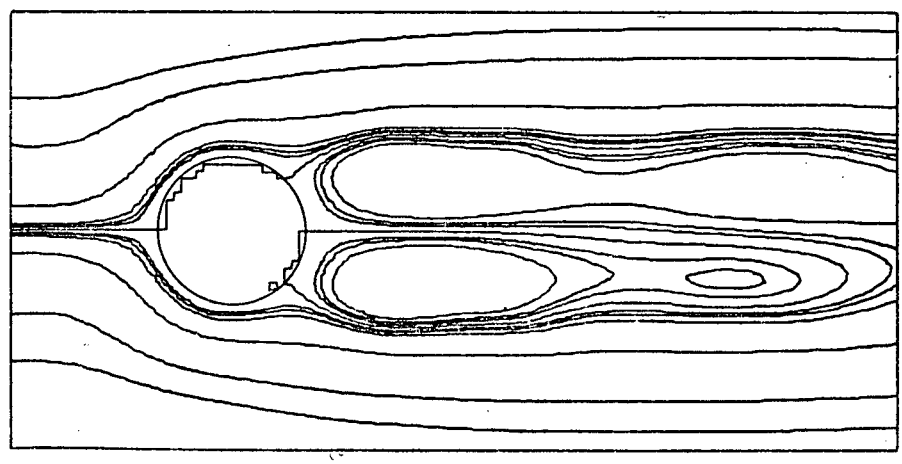

T = 16.5 SECONDS

FIGURE 16 (CONT.) STREAMLINES FOR TRANSIENT FLOW AROUND A CIRCULAR CYLINDER AT REYNOLDS NO. R = 140 FOR VARIOUS TIME INSTANTS